

**SILICON CARBIDE NANOWIRES:
ELASTIC PROPERTIES, DEFECTS, AND SURFACE FORMATIONS**

by

RYAN MICHAEL RICH

Bachelor of Science, 2006
Centre College
Danville, Kentucky

Submitted to the Graduate Faculty of the
College of Science and Engineering
Texas Christian University
in partial fulfillment of the requirements
for the degree of

Doctor of Philosophy

May, 2011

ACKNOWLEDGMENTS

I would like to sincerely thank my advisor, T.W. Zerda for allowing me to join his group. I have been afforded many opportunities by Dr. Zerda over the years working in him, for which I am truly grateful. I cannot thank him enough for his patience and encouragement throughout the course of my study.

I am also grateful for my professors at Centre College, especially Drs. Phillip Lockett, William Crummett, and Edward Montgomery. They are largely responsible for my love of physics and my decision to pursue my Ph.D.

I would like to thank my fellow graduate students, especially Dr. Stephen Nauyoks, Dr. Monika Wieligor, and Cassidy Newton for their friendship. Dr. Jaromir Patyk was a great help in the beginning of my research. I am grateful as well to my fiancée Shannon, for her love and support.

Finally I would like to thank my family, especially my parents Michael and Sharon, for supporting me on this lengthy endeavor and providing the opportunity for my education. My father urged me towards a Ph.D. in physics before I even graduated high school. So I dedicate this work to the memory of Michael Allen Rich, who was not able see it come to fruition.

This work was partially funded by a NSF grant DMR 0502136. The use of the National Synchrotron Light Source at Brookhaven National Laboratory was supported by the US Department of Energy, Office of Science.

TABLE OF CONTENTS

ACKNOWLEDGMENTS.....	ii
LIST OF FIGURES.....	v
LIST OF TABLES.....	x
CHAPTER 1: INTRODUCTION.....	1
CHAPTER 2: THEORETICAL FRAMEWORK.....	3
2.1 Crystal Structure.....	3
2.2 X-ray diffraction.....	7
2.3 Whole Profile Analysis of x-ray Diffraction.....	14
CHAPTER 3: INSTRUMENTAL.....	21
3.1 Diamond Anvil Cell.....	21
3.1.1 Flat-culet DAC.....	24
3.1.2 Beveled-culet DAC.....	27
3.2 X-ray Sources.....	30
3.2.1 Synchrotron Sources.....	30
3.2.2 X-ray Tubes.....	33
3.3 TEM and EDS.....	37
3.4 FTIR.....	38
CHAPTER 4: SYNTHESIS.....	41
4.1 Overview of Synthesis Methods Existing.....	41
4.2 SiC Nanowire Synthesis by Nanotube Confinement.....	42
4.2.1 Sample Vessel.....	42
4.2.2 Tube Furnace.....	43
4.2.3 Manipulation of Temperature.....	44
4.2.4 Calculation of Yield by XRD.....	46
4.2.5 Effects of Sintering Time.....	48
4.2.6 Effects of Vapor Pressure.....	50
4.3 Growth Mechanism.....	50
4.3.1 VLS Mechanism.....	50
4.3.2 VS Mechanism.....	52

4.3.3 Ostwald Ripening.....	56
4.4 SiC Nanowires Used in this Research.....	56
4.5 Acid Treatment.....	57
CHAPTER 5: HIGH PRESSURE EXPERIMENTS.....	59
5.1 Motivation.....	59
5.2 Results.....	60
5.3 Discussion.....	68
CHAPTER 6: DEFECTS.....	76
6.1 Motivation.....	76
6.2 TEM Analysis.....	78
6.3 XRD Analysis.....	83
6.3.1 The Williamson-Hall Plot.....	83
6.3.2 Application of the eCMWP Method.....	85
CHAPTER 7: SURFACE FORMATIONS.....	90
7.1 Motivation.....	90
7.2 Atomic Structure of the Amorphous Layer.....	90
7.2.1 Energy Dispersive Spectroscopy.....	90
7.2.2 Fourier Transform Infrared Spectroscopy.....	92
7.3 Surface Modification.....	97
7.3.1 Thermal Treatment.....	97
7.3.2 Acid Treatment.....	98
CHAPTER 8: Conclusion.....	104
REFERENCES.....	109

ABSTRACT

VITA

LIST OF FIGURES

Figure 2.1	A unit cell characterized by the primitive vectors, a , b , and c , as well as the angles between them, α , β , and γ	page 4
Figure 2.2	Real-space representation of the fcc crystalline structure.....	page 5
Figure 2.3	An atomic plane defined by the Miller indices (hkl).....	page 6
Figure 2.4	Diffraction off of two identical planes.....	page 8
Figure 2.5	X-ray diffractogram of SiC nanowires with atomic planes labeled in the convention of this paper, by their respective Miller indices. The measurement was made using Cu K_{α} radiation with $\lambda = 1.54 \text{ \AA}$	page 14
Figure 3.1	Schematic of the Diamond Anvil Cell.....	page 22
Figure 3.2	Construction of the DAC: a) The anvil is positioned over an opening in a steel seat. b) The anvil is held firmly to its seat by a metal stem. c) The anvil is glued down to the seat. d) When the glue has cured, the stem is removed and the anvils are installed into the DAC before alignment with set screws.....	page 23
Figure 3.3	The imprint diameter, d_i , and the culet diameter, d_c , were measured with a microscope. With the angle of the culet known, the pre-indented gasket thickness was determined.....	page 25
Figure 3.4	Schematic of the diameter measurements.....	page 25
Figure 3.5	Flat culet and beveled diamond anvils.....	page 27
Figure 3.6	Raw data collected from the Mar345 image plate depicting diffraction from SiC nanowires in the flat-culet DAC.....	page 32
Figure 3.7	Raw data from Figure 3.6 integrated by Fit2D (open circles). The data are fitted with Fityk (solid line), and the difference between the data and the fitting is displayed by the bottom line. The (111), (200), and (220) reflections of SiC are seen, along with the (111) and (200) reflections of gold used for pressure calibration...	page 33
Figure 3.8	Schematic representation of a typical x-ray tube.....	page 34

Figure 3.9	Divergence of the $K_{\alpha 1}$ and $K_{\alpha 2}$ lines seen in the diffraction data for SiC nanowires. The insert depicts a magnified view of the region in the dotted rectangle. Here a silver anode was employed with the $K_{\alpha 1}$ wavelength 0.5594205 Å and the $K_{\alpha 2}$ wavelength 0.563811 Å.....	page 36
Figure 3.10	The θ -2 θ diffractometer arrangement.....	Page 37
Figure 3.11	Infrared absorption of Diamond. The black line is the background from the conventional transmission arrangement. The grey line is the background collected from same equipment with the addition of the Diamond ATR attachment.....	page 40
Figure 4.1	Photograph of a typical sample ampoule.....	page 44
Figure 4.2	Temperature distribution of the tube furnace collected at three setpoints: 800°C (solid line), 1000°C (dashed line), and 1200°C (dotted line). As an example, dotted, straight lines are drawn to demonstrate that a desired silicon temperature of 900°C would require an ampoule 12.7 cm long. The MWCNT at the other end of the ampoule would thus be at 1063.4°C.....	page 46
Figure 4.3	Calibration curve used to determine the yield of a reaction. The intensity ratio on the horizontal axis is defined by Equation 4.1, while the mass ratio on the vertical axis is defined by Equation 4.2.....	page 47
Figure 4.4	SiC yield as a function of sintering time.....	page 50
Figure 4.5	Influence of sintering on nanowire diameters. It is seen that longer sintering times result in distributions shifted towards larger diameters.....	page 50
Figure 4.6	TEM image of a sample sintered for 52 hours.....	page 51
Figure 4.7	The effect of silicon vapor pressure on the SiC yield.	page 52
Figure 4.8	STEM image and EDS maps of four elements found within the same SiC nanoflower. In the EDS maps, lighter areas represent areas with higher concentrations of the specified element.....	page 53
Figure 4.9	TEM image of unspecified defects in a MWCNT.....	page 56

Figure 4.10	A model of a graphene sheet that rolls to form a carbon nanotube. It is shown without defects (left) and with Stone-Wales defects (right).....	page 56
Figure 5.1	Pressure induced shift of the (111) reflection from SiC nanowires. To guide the eye, experimental points recorded at different pressures are connected by lines.....	page 62
Figure 5.2	Mathematical fitting of the (111) reflection of SiC. Data collected at NSLS with $\lambda = 0.404067 \text{ \AA}$ on 130 nm grains of SiC at 35 GPa.....	page 63
Figure 5.3	Lattice parameter of nanocrystalline SiC samples under pressure: 20 nm grains (squares), 50 nm grains (circles), 130 nm grains (asterisks), and 30 nm nanowires (triangles).	page 64
Figure 5.4	Relative volume of SiC as a function of pressure for 20 nm grains (squares), 30 nm diameter nanowires (triangles), and 130 nm grains (stars). The data collected from 50 nm grains has been omitted for clarity. The lines represent linear regressions fitted to the data obtained for the grains (dashed line), nanowires (solid line), 50 nm grains (dotted line), and 130 nm grains (dash-dot line).....	page 66
Figure 5.5	Experimental data points for 20 nm grains (squares), 30 nm diameter nanowires (triangles), and 130 nm grains (stars). The data collected from 50 nm grains has been omitted for clarity. The dashed line represents the best fitting of Equation (5-1) to the data obtained for the grains (dashed line), nanowires (solid line), 50 nm grains (dotted line), and 130 nm grains (dash-dot line).....	page 67
Figure 5.6	The fitting of the Birch-Murnaghan equation to data from SiC nanowires 30 nm in diameter. The solid line shows the fitting done on data collected from the flat-culet DAC, i.e. at pressures less than 50 GPa. The dashed line shows the fitting when the additional datum from the beveled-culet DAC was included.....	page 69
Figure 5.7	Two-dimensional schematic model of a spherical nanograin. The atoms in the surface shell of thickness d_{shell} are compressed relative to the core of radius R_c	page 70

Figure 5.8	Two x-rays incident at an identical low angle are represented by solid lines. A slight relative displacement causes the second ray to travel one atomic layer deeper into the crystal. Three x-rays incident at an identical large angle are represented by broken lines. Depending on the displacement of the second and third large-angle rays, the penetration can be very deep into the crystal.....	page 72
Figure 5.9	The α -Q plot for 30 nm SiC nanowires. The a/a_0 values were calculated assuming a_0 of the perfect cubic structure was 4.356 Å. The broken line is shown to guide the eye.....	page 74
Figure 5.10	A model of a SiC nanowire. The core of radius R_c is surrounded by a shell of the same crystallographic structure but different lattice constant of thickness d_{shell} . The outer layer of thickness d is the amorphous layer.....	page 76
Figure 6.1	Direct-space image of twins in a SiC nanowire obtained by TEM. The angle formed at the twin boundary is 141° . Image presented courtesy of M. Wieligor.....	page 79
Figure 6.2	Construction of the electron diffraction pattern produced by twin defects. Here the beam size was 15 nm and the inverse of the diffraction images are shown for clarity. a) and b) are the diffraction patterns collected from two distinct regions of a SiC nanowire. c) depicts the diffraction image collected from the boundary where the electron beam is incident upon both regions. Above each diffraction image is a schematic of the atomic planes from which the diffraction originated.....	page 81
Figure 6.3	Left: a TEM image of stacking faults in a SiC nanowire. Right: A Fast Fourier transform of the image on the left. Notice the streaking that results from stacking faults.....	page 82
Figure 6.4	A SiC nanowire exhibiting a section with numerous planar faults and a defect-free section.....	page 83
Figure 6.5	The Williamson-Hall plots for SiC nanowires of average diameter 30 nm (solid squares) and SiC compacts (open symbols). Circles represent data for compacts obtained at 2 GPa and triangles for compacts sintered at 5.5 GPa. Data on SiC compacts originated from S. Nauyoks dissertation. ^[158]	page 86

Figure 6.6	The X-Ray diffraction pattern for SiC nanowires of average diameter 30 nm. Reflections are assigned to different crystallographic planes. The insert shows details of the (111) peak with the shoulder due to stacking faults.....	page 87
Figure 6.7	Example of the fitting procedure. Measured data (open circles) and fitted diffraction profile (solid line) for the 30 nm diameter SiC nanowires. The difference between the two sets of data is shown at the bottom part of the figure.....	page 87
Figure 7.1	TEM image of a silicon carbide nanowire. The EDS spectrum is shown in the bottom right corner and the data are quantified in the top right corner. The data were collected from the entire region shown by the image. In the insert in the left corner, the solid line represents oxygen concentration measured across the nanowire diameter.....	page 94
Figure 7.2	FTIR spectrum of SiC nanowires before thermal or acid treatment.....	page 95
Figure 7.3	FTIR spectra of one sample of SiC nanowires collected by various techniques. The black line is the spectrum collected via conventional transmission, the dark grey is the spectrum from nanowires dispersed in mineral oil between KBr plates, the light grey line is the spectrum collected via diamond ATR, and the dotted line is a spectrum collected with the photoacoustic technique, not discussed in this paper.....	page 96
Figure 7.4	Determination of the extinction coefficient of glass. The points were collected from glass-KBr pellets and the intensity was measured from the peak around 1100 cm^{-1} . The dotted line is a linear regression fit to the data points.....	page 98
Figure 7.5	Infrared spectrum of SiC nanowires before 700°C thermal treatment (black) and after thermal treatment (grey). Also included is a spectrum collected from pure KBr (dotted line).....	page 100
Figure 7.6	Infrared spectrum of SiC nanowires untreated (black line), treated with HF (dark grey line), and treated with HNO_3 (light grey line).....	page 101
Figure 7.7	Infrared spectrum highlighting CH_2 and CH_3 bands of SiC nanowires untreated (black line), treated with HF (dark grey line), and treated with HNO_3 (light grey line).....	page 102

Figure 7.8	The effect of acid treatment on dislocations in SiC Nanowires. Note that, for comparison, all data are normalized to measurements performed on untreated nanowires. The actual measured values appear above each bar.....	page 103
Figure 7.9	The formation of a dislocation from stresses induced by a surface defect.....	page 104
Figure 7.10	The formation of a dislocation from stresses induced by a surface defect and by a surface layer of a different composition.....	page 105

LIST OF TABLES

Table 3.1	The details of experimental parameters pertaining to the two diamond anvil cell systems.....	page 30
Table 5.1	High-pressure lattice parameter data with errors.....	page 64
Table 5.2	Lattice parameter reduction, where Δa is the total change in the lattice parameter and ΔP is the total change in pressure.....	page 65
Table 5.3	Measured Bulk Moduli of SiC nanoparticles.....	page 68
Table 6.1	The calculated parameters of the microstructure of silicon carbide in different forms: nanowires, SiC compact sintered from nanosize powder at 5.5 GPa and 1800°C, and SiC phase in diamond/silicon carbide composites sintered at 8.0 GPa and 1820oC. $\langle x \rangle_{area}$ is the area-weighted mean crystallite size, β is the planar fault probability, and ρ is the dislocation density.....	page 89

CHAPTER 1: INTRODUCTION

The growing interest in nanostructures is predicated upon the uniqueness of physical and chemical properties in materials that differ only in the size of their respective particulates. It has been shown that some materials become harder and tougher with decreasing grain size.^[1] The cohesion energy has been shown to decrease with size, reducing the melting point and phase transition temperature.^[2-4] Additionally, the unique electrical, optical, and magnetic properties of nanostructures are now better understood.^[3]

Of particular interest to this paper are structures that exhibit extreme confinement in only two dimensions, otherwise known as *nanowires*. Typically, two dimensions are confined to 10 – 100 nm, while the third dimension is on the order of microns. They are large enough to form crystal structures similar to their bulk counterparts, which allows predictions to be made about their properties. The lengths of nanowires in the unconfined direction are long enough to make them applicable when electric or heat conduction is desired.^[5]

Silicon Carbide (SiC) nanowires are of particular interest because of the numerous advantageous properties observed in the bulk form. SiC is used extensively as an abrasive due to its extremely high hardness. Its excellent resistance to heat has led to its employment in pressure sensors for high-temperature gas turbines^[6,7] as well as micromotors with satisfactory operation at high temperatures.^[6,8] In addition to its superb mechanical properties, SiC is a wide bandgap semiconductor well suited for use as a transistor in electronic applications. SiC performs very well in high-power and high-frequency situations.^[9,10] Its high thermal resistance allows SiC to be used in exceedingly

smaller integrated circuit devices.^[9,10] Thus recent years have seen growing effort to develop microelectronic devices from SiC for high-temperature, high-power, and high frequency applications.^[10]

This paper will discuss a unique method of producing SiC nanowires developed in recent years. It will also discuss the control of experimental conditions that affect their production. Finally, the suspected growth mechanisms will be addressed. This paper will go on to discuss the unique elastic properties of SiC nanowires which differ from bulk material. It will discuss quantitative analysis of defects in the crystal structure and conclude with the results of surface modification experiments.

CHAPTER 2: THEORETICAL FRAMEWORK

2.1 Crystal Structure

Essential to our study of nano-structured silicon carbide is understanding how the atoms arrange themselves throughout the material. The SiC studied is a crystalline material, meaning that its constituent atoms arrange in an ordered, repeating pattern. The framework of this repeating pattern is the point lattice – an “array of points in space so arranged that each point has identical surroundings.”^[12,13] If we choose one of these lattice points as the origin, then the location of each additional lattice point, \mathbf{r} , can be described in the following terms:

$$\mathbf{r} = n_1\mathbf{a} + n_2\mathbf{b} + n_3\mathbf{c} \quad (2-1)$$

where n_1 , n_2 , and n_3 are integers. The primitive vectors \mathbf{a} , \mathbf{b} , and \mathbf{c} define the crystallographic axes of the unit cell, a special arrangement of atoms repeated throughout the lattice. The primitive vectors also map out the volume of the unit cell.

$$V = \mathbf{a} \cdot \mathbf{b} \times \mathbf{c} \quad (2-2)$$

All other lattice points are periodic repetitions of the unit cell lattice points with their positions defined by \mathbf{r}' below.

$$\mathbf{r}' = \mathbf{r} + n_1\mathbf{a} + n_2\mathbf{b} + n_3\mathbf{c} \quad (2-3)$$

It is important to note that these lattice points do not necessarily consist of a solitary atom. Instead, there may exist a *basis* of dissimilar atoms whose composition and orientation are repeated throughout the lattice. The unit cell is further characterized by α , β , and γ , the angles between the crystallographic axes, see Figure 2.1.

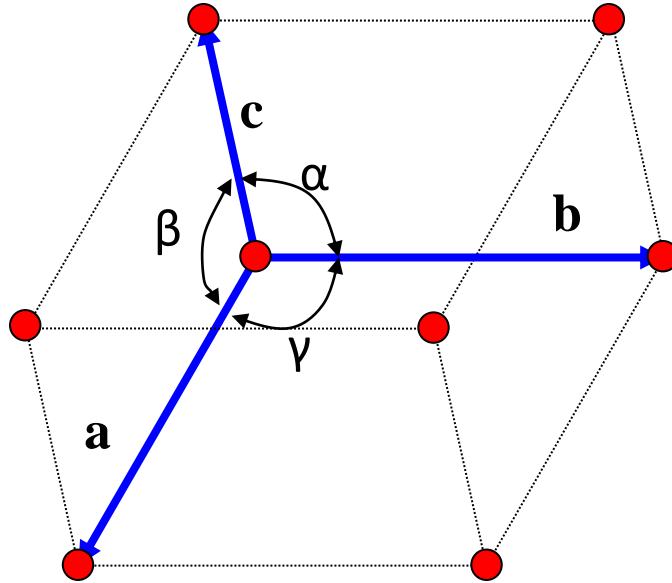


Figure 2.1 A unit cell characterized by the primitive vectors, **a**, **b**, and **c**, as well as the angles between them, α , β , and γ .

Crystals are categorized into seven distinct crystal systems by applying restrictions to their axial lengths and angles. When all crystal axes are equal in length and mutually perpendicular ($a = b = c$; $\alpha = \beta = \gamma = 90^\circ$), it is said that the unit cell belongs to the *cubic system*. The cubic crystal system is of particular interest to this paper, because the silicon carbide under study belongs to this system. More precisely, it belongs to the *face-centered cubic* (fcc) system, which means the material meets all the conditions of a cubic crystal already mentioned, with the additional condition that a lattice point exists at the center of each face of the unit cell, as in Figure 2.2. In accordance with Eq. 2-1, these additional lattice points are defined by the following set of three numbers: $(n_1, n_2, n_3) = (0, \frac{1}{2}, \frac{1}{2}), (\frac{1}{2}, 0, \frac{1}{2}), (\frac{1}{2}, \frac{1}{2}, 0)$. The basis at each lattice point consists of one carbon atom and one silicon atom.

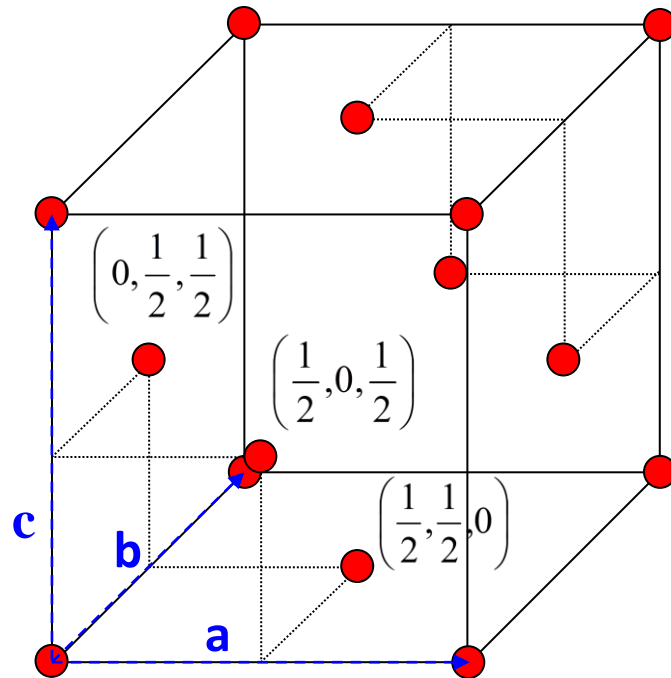


Figure 2.2 Real-space representation of the fcc crystalline structure.

Along with the positions of the individual lattice points, one can also study the locations and orientations of the crystallographic planes formed by any three, non-collinear atoms.^[3] The Miller indices, h , k , and l , convey this information, and they are defined as the reciprocals of the fractional intercepts of the plane in question with the crystallographic axes. The indices h , k , and l are expressed in terms of the lattice vectors \mathbf{a} , \mathbf{b} , and \mathbf{c} respectively. Therefore the plane (hkl) , as planes will be denoted in this paper, intercepts the crystal axes at the points \mathbf{a}/h , \mathbf{b}/k , and \mathbf{c}/l (see Figure 2.3).

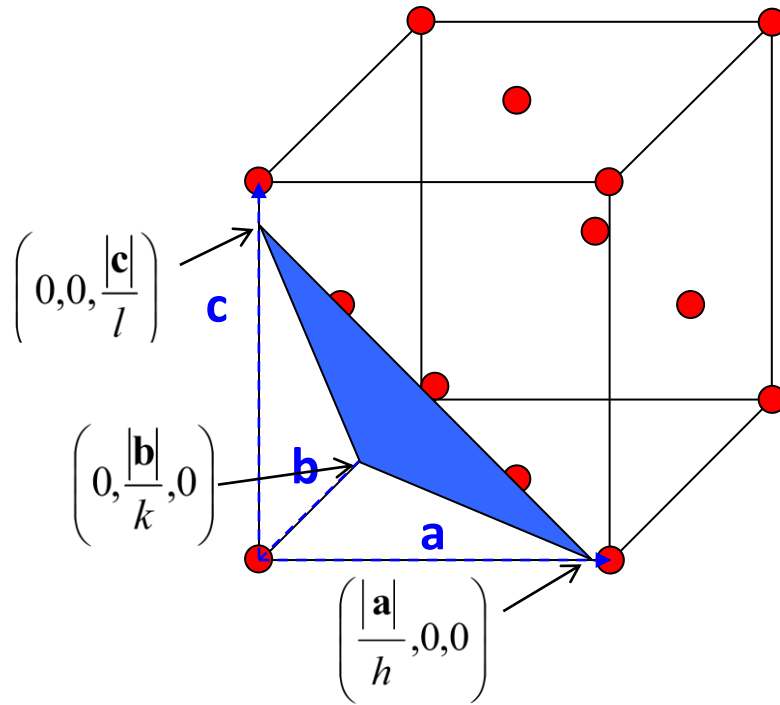


Figure 2.3 An atomic plane defined by the Miller indices (hkl) .

With the use of Miller indices, one can define the *reciprocal space* in which a single point represents an entire family of atomic planes in the direct lattice.^[13] The primitive reciprocal space vectors, \mathbf{a}^* , \mathbf{b}^* , and \mathbf{c}^* are analogous to the vectors of the direct lattice and are defined in the following manner:

$$\begin{aligned}
 \mathbf{a}^* &= \frac{\mathbf{b} \times \mathbf{c}}{\mathbf{a} \cdot [\mathbf{b} \times \mathbf{c}]} \\
 \mathbf{b}^* &= \frac{\mathbf{c} \times \mathbf{a}}{\mathbf{a} \cdot [\mathbf{b} \times \mathbf{c}]} \\
 \mathbf{c}^* &= \frac{\mathbf{a} \times \mathbf{b}}{\mathbf{a} \cdot [\mathbf{b} \times \mathbf{c}]}
 \end{aligned}
 \tag{2-4}$$

with the following properties

$$\begin{aligned}
 \mathbf{a}^* \cdot \mathbf{a} &= \mathbf{b}^* \cdot \mathbf{b} = \mathbf{c}^* \cdot \mathbf{c} = 1 \\
 \mathbf{a}^* \cdot \mathbf{b} &= \mathbf{a}^* \cdot \mathbf{c} = 0 \\
 \mathbf{b}^* \cdot \mathbf{c} &= \mathbf{b}^* \cdot \mathbf{a} = 0 \\
 \mathbf{c}^* \cdot \mathbf{a} &= \mathbf{c}^* \cdot \mathbf{b} = 0
 \end{aligned}
 \tag{2-5}$$

It follows that the reciprocal space lattice vector, \mathbf{G}_{hkl} , between identical atomic planes of the direct lattice is simply

$$\mathbf{G}_{hkl} = \frac{\mathbf{n}_{hkl}}{d_{hkl}}
 \tag{2-6}$$

where \mathbf{n}_{hkl} is the unit normal vector of the (hkl) plane, and d_{hkl} is the distance between two such planes. This vector is also written in a manner analogous to Equation (2-1):

$$\mathbf{G}_{hkl} = h\mathbf{a}^* + k\mathbf{b}^* + l\mathbf{c}^*
 \tag{2-7}$$

Combining equations (2-6) and (2-7) yields an expression for the (direct) lattice constant, a , of a cubic crystal in terms of the interplanar spacing and the Miller indices.

$$a = d\sqrt{h^2 + k^2 + l^2}
 \tag{2-8}$$

2.2 X-Ray Diffraction

The diffraction phenomenon is easily seen with visible light. A beam of light diffracts off of a grating in a manner dependent upon the beam's incident angle, wavelength, and the distance between the scattering centers of the grating.^[15] With complete knowledge of the light beam's properties, one may acquire information about the diffraction grating. In this manner, a crystal of interest is implemented as a diffraction grating in order to study its structure. The electromagnetic radiation must have a wavelength nearly equal to the interatomic distances, which are on the order of

angstroms. Having the required wavelength, x-rays have been chosen for just such applications since von Laue took up the problem in 1912.^[12, 16-18]

X-ray diffraction (XRD) makes use of two very important principles regarding electromagnetic radiation: 1) when two identical rays traverse unequal distances, a phase difference occurs, and 2) when these rays are combined, the phase difference produces a change in the amplitude of the resultant ray. A *diffracted beam* is defined as “a beam composed of a large number of scattered rays mutually reinforcing one another,”^[12] and it occurs when the rays’ phases differ by an integer multiple, n , of the wavelength, λ . It is said in this situation that the rays are completely in phase, and they combine to produce the maximum possible amplitude (constructive interference). Conversely, these rays will be completely out of phase and negate each other if the path length differs by half a wavelength, $\lambda/2$, or an odd multiple of this, $(2n-1)\lambda/2$.

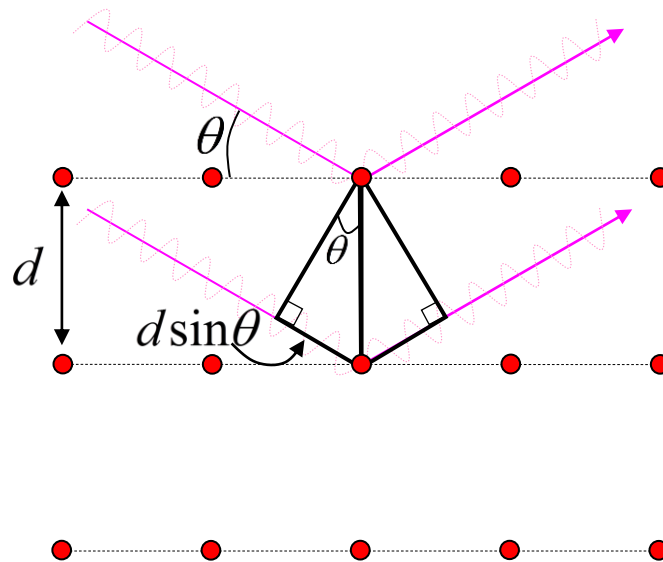


Figure 2.4 Diffraction from two identical planes.

These concepts are applied to x-ray diffraction when studying crystals. The path distance between the two rays in Figure 2.4 is $2d\sin(\theta)$. With this expression, we may place a constraint on the diffraction phenomenon, known as Bragg's Law:

$$n\lambda = 2d_{hkl} \sin \theta \quad (2-9)$$

where θ is the angle of incidence, and the Miller indices hkl are specific to the atomic plane producing the diffracted beam. In angle-dispersive studies, the wavelength is held constant, and the angle θ of a diffracted peak is a reciprocal measure of the crystal's interplanar spacing, thus the importance of reciprocal space is clearly seen. The Bragg law may also be represented in terms of the reciprocal lattice vector

$$\mathbf{G} = \mathbf{k}_f - \mathbf{k}_i \quad (2-10)$$

where \mathbf{k}_f and \mathbf{k}_i are the wave vectors of the diffracted and incident beams respectively.

X-ray scattering results from the interaction between electromagnetic radiation and the electrons of the crystal, so the intensity of the diffracted beam depends on the concentration of electrons in the reflecting plane (hkl). The atomic form factor, f , conveys this information by providing the amplitude of a wave scattered by one atom of a particular element. It follows that the amplitude of the wave scattered by all the atoms of the unit cell is given by the sum

$$F_{hkl} = \sum_1^N f_n e^{i\mathbf{r}_j \cdot \mathbf{G}_{hkl}} \quad (2-11)$$

The summation is carried out over the N atoms of type n in the unit cell. F is referred to as the *structure factor* of the material, the square of which is proportional to the intensity of the scattered wave. The subscript is needed, because, as will be shown, the structure

factor creates selection rules that determine the possible values of h , k , and l which produce reflections with non-zero intensity.

We can calculate the selection rules of the fcc lattice with one type of atom, which is true in the case of silicon, by applying the atomic locations to Equation (2-11). The lattice is formed by translation of four atoms at the relative locations $(n_1, n_2, n_3) = (0,0,0)$, $(0, \frac{1}{2}, \frac{1}{2})$, $(\frac{1}{2}, 0, \frac{1}{2})$, $(\frac{1}{2}, \frac{1}{2}, 0)$, as shown in Figure 2.2. Hence its structure factor is

$$\begin{aligned}
 F_{hkl} &= fe^{i2\pi(0)} + fe^{i2\pi\left(0a+\frac{1}{2}b+\frac{1}{2}c\right)\bullet(ha^*+kb^*+lc^*)} \\
 &\quad + fe^{i2\pi\left(\frac{1}{2}a+0b+\frac{1}{2}c\right)\bullet(ha^*+kb^*+lc^*)} + fe^{i2\pi\left(\frac{1}{2}a+\frac{1}{2}b+0c\right)\bullet(ha^*+kb^*+lc^*)} \\
 &= f + fe^{i\pi(k+l)} + fe^{i\pi h(k+l)} + fe^{i\pi(h+k)}
 \end{aligned} \tag{2-12}$$

Equation (2-12) leads to the following conditions of scattering by fcc crystals:

$$F_{hkl} = \begin{cases} 4f & \text{for } h, k, l \text{ unmixed} \\ 0 & \text{for } h, k, l \text{ mixed} \end{cases} \tag{2-13}$$

Determination of the structure factor for cubic silicon carbide gets slightly more complicated. The atoms are arranged in the *zinc blend structure*, with Si atoms at the aforementioned coordinates and C atoms at the following locations: $(\frac{1}{4}, \frac{1}{4}, \frac{1}{4})$, $(\frac{1}{4}, \frac{3}{4}, \frac{3}{4})$, $(\frac{3}{4}, \frac{1}{4}, \frac{3}{4})$, $(\frac{3}{4}, \frac{3}{4}, \frac{1}{4})$. The structure factor for the (111) reflection is then calculated as follows:

$$\begin{aligned}
 F_{111} &= \sum_m f_{Si} e^{i\mathbf{r}_m \bullet \mathbf{G}_{hkl}} + \sum_n f_C e^{i\mathbf{r}_n \bullet \mathbf{G}_{hkl}} \\
 &= f_{Si} e^{i2\pi(0)} + f_{Si} e^{i2\pi\left(0a+\frac{1}{2}b+\frac{1}{2}c\right)\bullet(1a^*+1b^*+1c^*)} + f_{Si} e^{i2\pi\left(\frac{1}{2}a+0b+\frac{1}{2}c\right)\bullet(1a^*+1b^*+1c^*)} \\
 &\quad + f_{Si} e^{i2\pi\left(\frac{1}{2}a+\frac{1}{2}b+0c\right)\bullet(1a^*+1b^*+1c^*)} + f_C e^{i2\pi\left(\frac{1}{4}a+\frac{1}{4}b+\frac{1}{4}c\right)\bullet(1a^*+1b^*+1c^*)} \\
 &\quad + f_C e^{i2\pi\left(\frac{1}{4}a+\frac{3}{4}b+\frac{3}{4}c\right)\bullet(1a^*+1b^*+1c^*)} + f_C e^{i2\pi\left(\frac{3}{4}a+\frac{1}{4}b+\frac{3}{4}c\right)\bullet(1a^*+1b^*+1c^*)} \\
 &\quad + f_C e^{i2\pi\left(\frac{3}{4}a+\frac{3}{4}b+\frac{1}{4}c\right)\bullet(1a^*+1b^*+1c^*)} + f_C e^{i2\pi\left(\frac{3}{4}a+\frac{3}{4}b+\frac{1}{4}c\right)\bullet(1a^*+1b^*+1c^*)}
 \end{aligned}$$

$$\begin{aligned}
&= f_{Si} + f_{Si}e^{i2\pi(1)} + f_{Si}e^{i2\pi(1)} + f_{Si}e^{i2\pi(1)} + f_c e^{i2\pi\left(\frac{3}{4}\right)} + f_c e^{i2\pi\left(\frac{7}{4}\right)} + f_c e^{i2\pi\left(\frac{7}{4}\right)} + f_c e^{i2\pi\left(\frac{7}{4}\right)} \\
&= f_{Si} \left[1 + e^{i2\pi} + e^{i2\pi} + e^{i2\pi} \right] + f_c \left[e^{i\left(\frac{3}{2}\right)\pi} + e^{i\left(\frac{7}{2}\right)\pi} + e^{i\left(\frac{7}{2}\right)\pi} + e^{i\left(\frac{7}{2}\right)\pi} \right] \\
&= f_{Si} [1 + 1 + 1 + 1] + f_c [-i - i - i - i] \\
&= 4f_{Si} - 4if_c
\end{aligned} \tag{2-14}$$

The atomic form factors, f_{Si} and f_c , correspond to silicon and carbon respectively. It is clearly seen that there is constructive interference in this case, and the (111) plane will produce a diffraction signal with intensity proportional to

$$|F_{111}|^2 = 16(f_{Si}^2 + f_c^2) \tag{2-15}$$

Now consider the (110) reflection:

$$\begin{aligned}
F_{110} &= \sum_m f_{Si} e^{i\mathbf{r}_m \cdot \mathbf{G}_{hkl}} + \sum_n f_c e^{i\mathbf{r}_n \cdot \mathbf{G}_{hkl}} \\
&= f_{Si} e^{i2\pi(0)} + f_{Si} e^{i2\pi\left(0a + \frac{1}{2}b + \frac{1}{2}c\right) \cdot (1a^* + 1b^* + 0c^*)} + f_{Si} e^{i2\pi\left(\frac{1}{2}a + 0b + \frac{1}{2}c\right) \cdot (1a^* + 1b^* + 0c^*)} \\
&\quad + f_{Si} e^{i2\pi\left(\frac{1}{2}a + \frac{1}{2}b + 0c\right) \cdot (1a^* + 1b^* + 0c^*)} + f_c e^{i2\pi\left(\frac{1}{4}a + \frac{1}{4}b + \frac{1}{4}c\right) \cdot (1a^* + 1b^* + 0c^*)} \\
&\quad + f_c e^{i2\pi\left(\frac{1}{4}a + \frac{3}{4}b + \frac{3}{4}c\right) \cdot (1a^* + 1b^* + 0c^*)} + f_c e^{i2\pi\left(\frac{3}{4}a + \frac{1}{4}b + \frac{3}{4}c\right) \cdot (1a^* + 1b^* + 0c^*)} \\
&\quad + f_c e^{i2\pi\left(\frac{3}{4}a + \frac{3}{4}b + \frac{1}{4}c\right) \cdot (1a^* + 1b^* + 0c^*)} \\
&= f_{Si} + f_{Si} e^{i2\pi\left(\frac{1}{2}\right)} + f_{Si} e^{i2\pi\left(\frac{1}{2}\right)} + f_{Si} e^{i2\pi(1)} + f_c e^{i2\pi\left(\frac{1}{2}\right)} + f_c e^{i2\pi(1)} + f_c e^{i2\pi(1)} + f_c e^{i2\pi\left(\frac{3}{2}\right)} \\
&= f_{Si} \left[1 + e^{i\pi} + e^{i\pi} + e^{i2\pi} \right] + f_c \left[e^{i\pi} + e^{i2\pi} + e^{i2\pi} + e^{i3\pi} \right] \\
&= f_{Si} [1 - 1 - 1 + 1] + f_c [-1 + 1 + 1 - 1] \\
&= 0
\end{aligned} \tag{2-16}$$

There is complete destructive interference for planes such as (110), and no diffraction signal is produced. The above calculations can be generalized in the following manner:

$$\begin{aligned}
F_{hkl} &= \sum_m f_{Si} e^{i\mathbf{r}_m \cdot \mathbf{G}_{hkl}} + \sum_n f_c e^{i\mathbf{r}_n \cdot \mathbf{G}_{hkl}} \\
&= f_{Si} e^{i2\pi(0)} + f_{Si} e^{i2\pi\left(0a + \frac{1}{2}b + \frac{1}{2}c\right) \cdot (ha^* + kb^* + lc^*)} + f_{Si} e^{i2\pi\left(\frac{1}{2}a + 0b + \frac{1}{2}c\right) \cdot (ha^* + kb^* + lc^*)} \\
&\quad + f_{Si} e^{i2\pi\left(\frac{1}{2}a + \frac{1}{2}b + 0c\right) \cdot (ha^* + kb^* + lc^*)} + f_c e^{i2\pi\left(\frac{1}{4}a + \frac{1}{4}b + \frac{1}{4}c\right) \cdot (ha^* + kb^* + lc^*)} \\
&\quad + f_c e^{i2\pi\left(\frac{1}{4}a + \frac{3}{4}b + \frac{3}{4}c\right) \cdot (ha^* + kb^* + lc^*)} + f_c e^{i2\pi\left(\frac{3}{4}a + \frac{1}{4}b + \frac{3}{4}c\right) \cdot (ha^* + kb^* + lc^*)} \\
&\quad + f_c e^{i2\pi\left(\frac{3}{4}a + \frac{3}{4}b + \frac{1}{4}c\right) \cdot (ha^* + kb^* + lc^*)} \\
&= f_{Si} + f_{Si} e^{i2\pi\left(\frac{k+l}{2} + \frac{l}{2}\right)} + f_{Si} e^{i2\pi\left(\frac{h+l}{2} + \frac{l}{2}\right)} + f_{Si} e^{i2\pi\left(\frac{h+k}{2} + \frac{l}{2}\right)} + f_c e^{i2\pi\left(\frac{h}{4} + \frac{k}{4} + \frac{l}{4}\right)} \\
&\quad + f_c e^{i2\pi\left(\frac{h}{4} + \frac{3k}{4} + \frac{3l}{4}\right)} + f_c e^{i2\pi\left(\frac{3h}{4} + \frac{k}{4} + \frac{3l}{4}\right)} + f_c e^{i2\pi\left(\frac{3h}{4} + \frac{3k}{4} + \frac{l}{4}\right)} \\
&= f_{Si} \left[1 + e^{i\pi(k+l)} + e^{i\pi(h+l)} + e^{i\pi(h+k)} \right] \\
&\quad + f_c \left[e^{\frac{i\pi}{2}(h+k+l)} + e^{\frac{i\pi}{2}(h+k+l)} e^{i2\pi(k+l)} + e^{\frac{i\pi}{2}(h+k+l)} e^{i2\pi(h+l)} \right. \\
&\quad \left. + e^{\frac{i\pi}{2}(h+k+l)} e^{i2\pi(h+k)} \right] \\
&= f_{Si} \left[1 + e^{i\pi(k+l)} + e^{i\pi(h+l)} + e^{i\pi(h+k)} \right] \\
&\quad + f_c e^{\frac{i\pi}{2}(h+k+l)} \left[1 + e^{i2\pi(k+l)} + e^{i2\pi(h+l)} + e^{i2\pi(h+k)} \right] \\
&= 4 \left[f_{Si} + f_c e^{\frac{i\pi}{2}(h+k+l)} \right] \tag{2-17}
\end{aligned}$$

And therefore the intensity of the diffracted wave is proportional to

$$\begin{aligned}
|F|^2 &= 16 \left[f_{Si} + f_c e^{\frac{i\pi}{2}(h+k+l)} \right] \left[f_{Si} + f_c e^{-\frac{i\pi}{2}(h+k+l)} \right] \\
&= 16 \left[f_{Si}^2 + f_c^2 + f_{Si} f_c \left(e^{\frac{i\pi}{2}(h+k+l)} + e^{-\frac{i\pi}{2}(h+k+l)} \right) \right] \\
&= 16 \left[f_{Si}^2 + f_c^2 + 2f_{Si} f_c \cos \frac{\pi}{2}(h+k+l) \right] \\
&= \begin{cases} 16(f_{Si}^2 + f_c^2) & \text{when } h+k+l \text{ is odd} \\ 16(f_{Si} + f_c)^2 & \text{when } h+k+l \text{ is an even multiple of 2} \\ 16(f_{Si} - f_c)^2 & \text{when } h+k+l \text{ is an odd multiple of 2} \end{cases} \tag{2-18}
\end{aligned}$$

According to these calculations, the intensity of the (220) reflection will be $64f_{SiC}$ times greater than the intensity of the (200) reflection. Of course, there are other factors affecting experimental intensities, but Figure 2.6 confirms that the (220) reflection is indeed more intense than the (200) reflection.

Much information can be extracted from XRD data. The convention is to plot data on a graph of intensity versus 2θ , where θ is the angle of incidence. This will be explained further in Section 3.2. A diffractogram collected from SiC nanowires is shown in Figure 2.5, each peak being labeled with the Miller indices assigned to that particular reflection. The locations of the reflections are dependent upon the wavelength of the source radiation. However, the Bragg law, Equation (2-9), can be utilized to convert 2θ into d-spacing which is independent of wavelength, and the d-spacing can then be used to calculate the lattice constant via Equation (2-8). Alternatively, this may be done in one step by combining Equation (2-9) and Equation (2-8) in the following manner:

$$a = \frac{n\lambda}{2\sin\left(\frac{2\theta}{2}\right)} \sqrt{h^2 + k^2 + l^2} \quad (2-19)$$

The volume of the unit cell is simply the cube of the lattice constant.

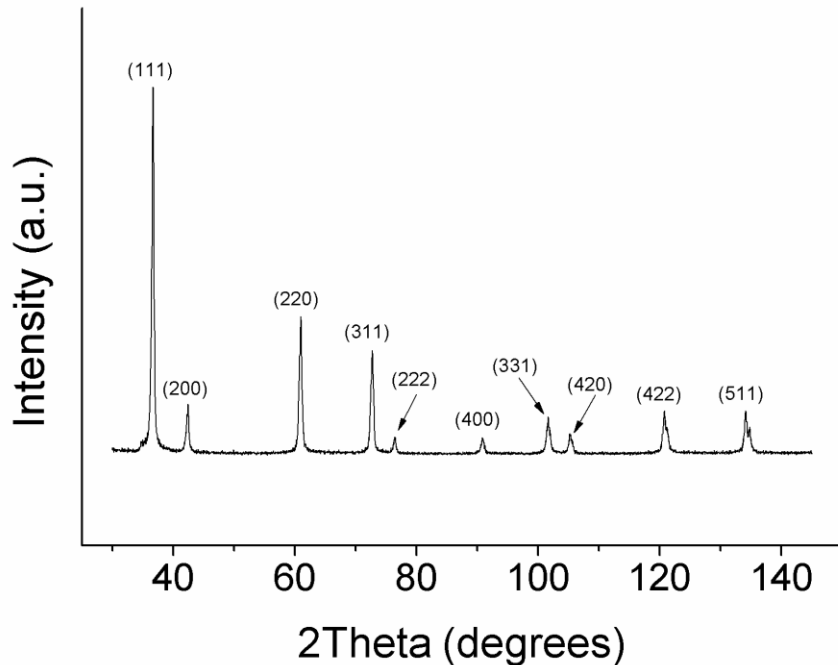


Figure 2.5 X-ray diffractogram of SiC nanowires with atomic planes labeled in the convention of this paper, by their respective Miller indices. The measurement was made using Cu K_{α} radiation with $\lambda = 1.54\text{\AA}$.

2.3 Whole Profile Analysis of X-ray Diffraction Patterns

In recent decades, ever increasing computing capabilities combined with improved laboratory x-ray sources and dedicated synchrotron sources have led scientists to revisit x-ray line broadening for the purposes of microstructural analysis. It is not only reasonably fast to collect the diffraction data, but such data are also collected from a macroscopic volume, thus providing a more statistically accurate picture of the sample.

The use of x-ray diffraction to characterize microstructure began in earnest by Scherrer in the 1920s^[17]. He noticed that when multi-crystalline samples contain domains less than 100 nm in size, the x-ray powder diffraction reflections begin to broaden. The explanation of this lies in situations in which the Bragg condition is not

met. Consider an x-ray beam incident upon a crystal at such an angle that the ray from the second plane of atoms is phase shifted by $\frac{1}{4} \lambda$ in relation to the ray from the first plane of atoms. There will be destructive interference, but it will not completely cancel out the two rays. Thus the signal received is greater than the background level, but weaker than the signal when the Bragg condition is satisfied. However, a third ray incident on the third plane of atoms will be phase shifted by $\frac{1}{4} \lambda$ from the second ray, and $\frac{1}{2} \lambda$ from the first ray, thus the first and third rays will cancel each other out. This is an extreme case, and it is easy to see that the closer the path length of a reflected ray is to $n\lambda$ while still not satisfying the Bragg condition, the deeper within the crystal you have to look for its destructive counterpart. If the crystal is small enough, this canceling ray may not exist at all, and the resulting diffractogram exhibits a broadened peak. Scherrer formulated a way to calculate the average particle size, $\langle x \rangle$, based on peak broadening, and the result is as follows^[17]:

$$\langle x \rangle = \frac{B\lambda}{\beta \cos \theta} \quad (2-20)$$

where λ is the wavelength, β is the full width at half maximum (FWHM) of a particular reflection, θ is the diffraction angle, and B is a constant called the shape factor, which is typically around 1. The validity of this equation holds as long as stress and strain are not present in the sample. Clearly another method was needed to address additional broadening introduced from stress and strain.

Williamson and Hall^[19] introduced a method by which one may determine the dominant source of peak broadening. Peak broadening due solely to decreasing particle size will effect each reflection equally, i.e. there is no dependence of FWHM on the diffraction vector K .

$$K = \frac{2 \sin \theta}{\lambda} \quad (2-21)$$

The anisotropic nature of stresses and defects, however, leads to a direct dependence of FWHM on K . If a plot of FWHM versus K is made, and a non-monotonic increase in FWHM is observed,^[20] this indicates that the source of peak broadening involves stresses due to crystal defects as well as crystallite size. This is referred to as a Williamson-Hall plot.

The modern theory of x-ray bandshapes is expressed as functions of crystallite sizes and their distribution, planar faults density, dislocation induced strain effects, and the dislocation type, screw or edge. The Convolutional Multiple Whole Profile (CMWP) procedure improves upon the traditional method by implementing the automatic deconvolution of overlapping peaks and instrumental effects.^[21, 22] The CMWP method assumes that the experimental profile is a convolution of functions I^d , I^f , I^s , and I^i representing broadenings due to dislocations, planar faults, limited crystalline sizes, and instrumental function, respectively, and also depends on the background, I^b

$$I^{exp}(\theta) = I^b(\theta) + I^s(\theta) * I^d(\theta) * I^f(\theta) * I^i(\theta) * \quad (2-22)$$

The stars in Equation (2-22) represent convolution. In the first step of the analysis the background is removed from the experimental profile. Next, the experimental profiles are stripped of instrumental broadening. In our case we estimated instrumental broadening by recording the diffraction pattern of LaB₆. The LaB₆ standard, free of crystal defects and composed of large crystal grains, produces a pattern that is broadened only by the instrumental function. Dividing the Fourier Transform of the experimental profile by the Fourier Transform of the LaB₆ profile, with the background subtracted from each, we get

$$A_L^{exp} = A_L^s A_L^d A_L^f \quad (2-23)$$

where L represents the Fourier variable. The difficulties in solving Equation (2-23) is in defining the Fourier coefficients A_L^s , A_L^d , and A_L^f , which account for the size, distortions due to dislocations, and distortions due to planar faults, respectively.

The Fourier size coefficient, A^s , can be estimated assuming that the specimen is a mixture of spherical crystallites. The log-normal size function

$$f(x) = \frac{1}{(2\pi)^{1/2} \sigma x} \exp \left[\frac{-(\log(x/w))^2}{2\sigma^2} \right] \quad (2-24)$$

where σ is the variance and w is the median, describes the crystallite size distribution. A^s can be calculated from^[23-25]

$$A^s(t) = \int_{|t|}^{\infty} \left(1 - \frac{|t|}{M} \right) M^2 \left[\int_M^{\infty} f(x) dx \right] dM \quad (2-25)$$

$$A^s(L) \sim \frac{m^3 e^{4.5\sigma^2}}{3} \operatorname{erfc} \left[\frac{\ln\left(\frac{|L|}{m}\right)}{\sqrt{2\sigma}} - 1.5\sqrt{2\sigma} \right] - \frac{m^2 e^{2\sigma^2} |L|}{3} \operatorname{erfc} \left[\frac{\ln\left(\frac{|L|}{m}\right)}{\sqrt{2\sigma}} - \sqrt{2\sigma} \right] \\ + \frac{|L|^3}{6} \operatorname{erfc} \left[\frac{\ln\left(\frac{|L|}{m}\right)}{\sqrt{2\sigma}} \right] \quad (2-26)$$

where erfc is the complementary error function. The area-weighted mean crystallite size is given by

$$\langle x \rangle_{\text{area}} = w e^{2.5\sigma^2} \quad (2-27)$$

The size profile may also be scaled to account for non-spherical crystallites or subgrains.^[26] One can find a similar expression for the volume-weighted mean but we will not use it in this paper and limit the discussion to the $\langle x \rangle_{\text{area}}$.

The Fourier coefficient due to dislocations was found by using the Warren-Averbach^[27] method. The coefficient can be expressed as:

$$A_L^D = \exp\left(-2\pi^2 g^2 L^2 \langle \varepsilon_L^2 \rangle\right) \quad (2-28)$$

where L is the Fourier transform variable, g is the magnitude of the diffraction vector, and $\langle \varepsilon_L^2 \rangle$ is the mean square strain, which depends on how much the atoms are displaced due to strain compared to an ideal lattice arrangement.^[27] Krivoglaz^[28] developed a method to calculate the mean square strain caused by dislocations. Wilkens^[29] improved Krivoglaz's method by assuming that dislocations have an outer cutoff radius, R_c^* . Using this parameter Wilkens derived the following equation for the mean strain:

$$\langle \varepsilon_L^2 \rangle = \left(\frac{b}{2\pi}\right)^2 \pi \rho C f(L/R_c^*) \quad (2-29)$$

where b is the magnitude of the Burgers vector, C is the contrast factor of the dislocations and $f(L/R_c^*)$ is the Wilkens function of strain as defined by:

$$\begin{aligned} f^*(\eta) = & -\log \eta + \left(\frac{7}{4} - \log 2\right) + \frac{512}{90} \frac{1}{\pi} \frac{1}{\eta} + \frac{2}{\pi} \left(1 - \frac{1}{4\eta^2}\right) \int_0^\eta \frac{\arcsin V}{V} dV \\ & - \frac{1}{\pi} \left(\frac{769}{180} \frac{1}{\eta} + \frac{41}{90} \eta + \frac{2}{90} \eta^3\right) (1 - \eta^2)^{1/2} \\ & - \frac{1}{\pi} \left(\frac{11}{12} \frac{1}{\eta^2} + \frac{7}{2} + \frac{1}{3} \eta^2\right) \arcsin \eta + \frac{1}{6} \eta^2, \quad \eta < 1 \end{aligned} \quad (2-30)$$

$$f^*(\eta) = \frac{512}{90} \frac{1}{\pi} \frac{1}{\eta} - \left(\frac{11}{24} + \frac{1}{4} \log 2\eta\right) \frac{1}{\eta^2}, \quad \eta \geq 1 \quad (2-31)$$

where $f(L/R_c^*) = f^*(\eta)$ and $\eta = (1/2) \exp(-1/4) (L/R_c^*)$. The average contrast factor, C , accounts for the anisotropy of the dislocations.^[20] The average contrast factor

in cubic crystals is dependent on C_{h00} , the average contrast factor in the $\{h00\}$ direction. C_{h00} is dependent on the elasticity of the material and on the fourth-order polynomial of the hkl indices, and therefore the average contrast factor is:

$$C = C_{h00} \left(1 - q \frac{h^2k^2 + h^2l^2 + k^2l^2}{(h^2 + k^2 + l^2)^2} \right) \quad (2-32)$$

The effect of faulting and twinning can be represented by a uniform profile function. This function was shown to be the Lorentzian, where the total profile of a faulted or twinned Bragg reflection is the linear combination of Lorentzians broadened and/or shifted according to well-defined hkl dependent rules^[30]. In order to determine the Fourier coefficient due to planar faults, A_L^f , the magnitude of peak broadening and peak location were first evaluated. Diffraction peaks were numerically calculated using the program: DIFFAX (diffraction of faulted crystals). DIFFAX^[31] uses the recursion relationship of the wave function in crystals to simulate planar faults. Balogh and coworkers^[22] calculated the first 15 Bragg reflections of the face-centered cubic crystals with extrinsic and intrinsic stacking faults and twins with probabilities up to 20%. They analyzed over 15,000 subreflections due to planar faults. It was found that they fit either a delta function or a Lorentzian function. The FWHM and the shift of the subreflections were dependent on the hkl indices and the planar fault probability which was approximated by a fifth order polynomial. These results have been summarized in the form of a table of the fifth order polynomials for each hkl set which is subsequently used by the extended CWMP program, eCMWP.^[22] This program is an improvement of the CWMP program because it allows for quantitative characterization of planar faults.

Instead of analyzing individual peaks one at a time, the eCMWP fitting routine analyzes the whole profile simultaneously. For a cubic lattice like that of SiC, it provides the following parameters: 1) the mean size, 2) standard deviation, with which one can find $\langle x \rangle_{area}$ from Equation (2-27), 3) β the fault or twin probability, 4) ρ the dislocation density, and 5) q , a parameter that is dependent on the dislocation type, screw or edge.

CHAPTER 3: INSTRUMENTAL

3.1 Diamond Anvil Cell

The experimental designs of Percy Bridgman dominated high-pressure research at the beginning of the twentieth century.^[33,34] His opposed-anvil press design allowed pressures of up to 10 gigapascals (GPa) to be achieved, but the most significant breakthrough occurred when this approach was applied using diamonds, which have pushed high-pressure studies above 200 GPa.^[34] These pressures are achievable due to diamond's hardness—the hardest known material in nature.^[33] The 1956 invention of the diamond anvil cell (DAC) at the National Bureau of Standards made it possible to conveniently conduct *in situ*, high-pressure diffraction and spectroscopy studies because of diamond's transparency to many forms of electromagnetic radiation.^[33,34] The design of the DAC is simple. A hole is drilled into a pre-hardened metal foil gasket, and the sample is loaded into this hole. Another material is added as a pressure calibrator, before the hole is filled with a hydrostatic medium. The sample, calibrator, pressure medium, and gasket are all squeezed between two well-aligned diamond anvils.^[33] The external pressure is magnified when transmitted to the smaller culet surface of the anvils. Therefore very little external pressure is needed.

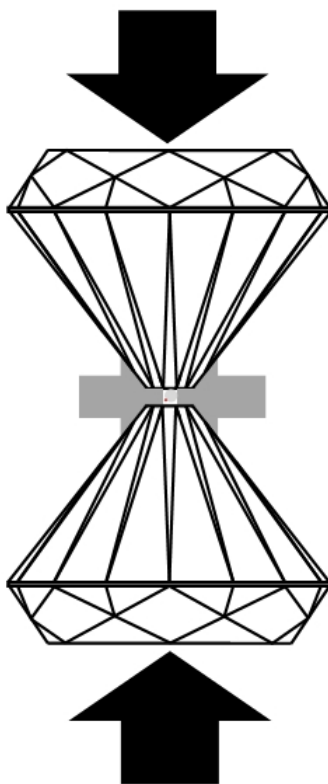


Figure 3.1 Schematic of the Diamond Anvil Cell.

There exists a large number of DAC designs, calibration techniques, pressure media, etc., but this paper will focus only on the two arrangements used in the relevant experiments: the flat culet DAC used for pressures up to 60 GPa and the beveled-culet DAC used for pressures greater than 60 GPa. It was necessary to have two DACs because of the difficulty involved in loading and the reduced sample volume needed for the beveled DAC. Both arrangements started with the same 0.25 carat, type IA diamonds. IA designates a relatively large nitrogen content. It was not necessary to use type IIA diamonds, which contain lower amounts of nitrogen impurities, as this would only affect spectroscopy measurements and not diffraction. The diamonds were selected to have low birefringence—a measure of stress within the crystal. They were custom cut

along the diamonds' strongest axis, (100), by Scimed GmbH, Isselburg, Germany. Each diamond was anchored firmly to a steel disk, glue was applied around the base, and the glue was allowed to cure for several hours. The diamonds were secured into top or bottom half of the steel cell by set screws holding the steel plates on which the diamonds were glued. The diamond backing provided a window through which x-ray radiation could pass. This window was an eccentric, elliptically-shaped hole on the diffraction side of the DAC, allowing the x-ray detector to view a larger range of diffraction along the window's major axis. This window also provided the means with which to meticulously align the top and bottom anvils using a microscope. They were first aligned coarsely by adjusting the set screws holding the bottom anvil. The fine adjustments were made by allowing the two anvils to gently touch and observing the diffraction fringes from the interface of the two diamonds. When the crystallographic axes of the two diamonds were perfectly aligned, these diffraction fringes disappeared.

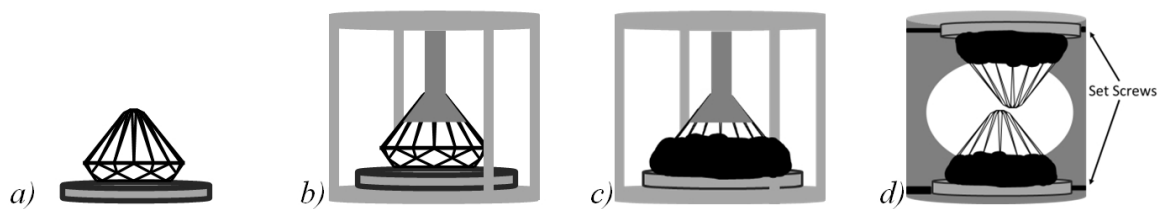


Figure 3.2 Construction of the DAC: a) The anvil is positioned over an opening in a steel seat. b) The anvil is held firmly to its seat by a metal stem. c) The anvil is glued down to the seat. d) When the glue is cured, the stem is removed and the anvils are installed into the DAC before alignment with set screws.

3.1.1 Flat-culet DAC

Much care was taken in the preparation of the DAC gaskets. The starting material for the flat-culet DAC was 250 μm thick Inconel, an alloy of nickel, chromium, and iron. The gaskets were first pre-indented by pressurization in the DAC. The pre-indentation hardened the gasket and reduced the amount of material that would be displaced upon re-pressurization with the loaded sample.^[33] If the gasket was too thick, the pressure would create too much metal flow, and the sample hole would close. If, however, the gasket was too thin, the pressure medium would expand past the edge of the diamond culet, thereby releasing the seal. The thickness of the gasket was determined *in situ* by measuring the ratio of the culet diameter to the outer diameter of the imprint with the aid of a microscope (see Figures 3.3 and 3.4). The proper ratio was determined by extensive trial and error. In this manner, the gasket was squeezed to approximately 30 μm . Drilling the 200 μm hole in the center of the gasket is very difficult with conventional micro-drills, so an electronic discharge machine (EDM) was employed instead. The EDM discharged current to the gasket through alcohol. The discharge melted the gasket, the molten metal mixed with the cooler alcohol, and the re-solidified metal particulates were carried away from the hole.^[35]

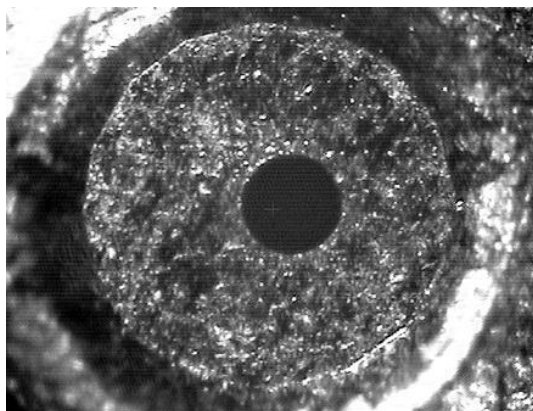


Figure 3.3 The imprint diameter, d_i , and the culet diameter, d_c , were measured with a microscope. With the angle of the culet known, the pre-indented gasket thickness was determined.

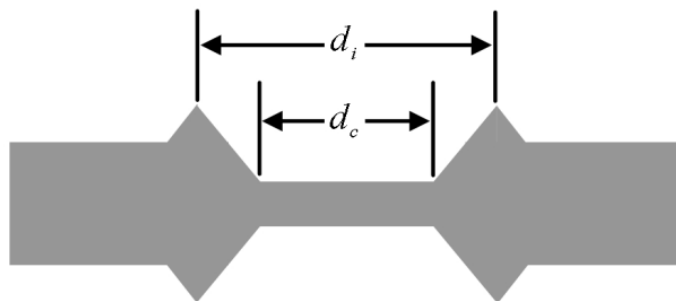


Figure 3.4 Schematic of the diameter measurements.

With the gasket indented and the hole formed, the sample could then be loaded into the DAC. The size of the diamond culets dictated the use of very small sample volumes, resulting in low signal strength in addition to the already present problem of peak broadening from nanosized crystallites.^[12,17] Therefore, the gasket hole was filled with the largest sample volume possible, increasing signal strength at the risk of losing hydrostatic conditions.

A small gold flake was added with the sample for pressure calibration. The most common method of pressure calibration is to add a ruby chip and utilize the pressure dependence of ruby's R1 fluorescence line.^[36] However, the weak diffraction of SiC made it necessary to load as much of the sample into the gasket hole as possible, which enveloped the ruby chip and made observance of the fluorescence line impossible. Therefore the well-documented shift of gold's XRD reflections, described by Jamieson et al.^[37] and later refined by Anderson^[38] et al., was employed. The following equation of state was used to determine pressure, P , from quantities easily obtained through XRD.

$$P = \frac{3K_0 \left(1 - \frac{a}{a_{0R}}\right)}{\left(\frac{a}{a_{0R}}\right)^5} \exp \left[\frac{3}{2} (K_0' - 3) \left(1 - \frac{a}{a_{0R}}\right) \right] \quad (3-7)$$

where K_0 is the bulk modulus of gold (166.7 GPa), K_0' is its unit-less pressure derivative (6.3 for Au), a_{0R} is the lattice constant of gold at atmospheric pressure and temperature (4.0784 Å), and a is the lattice parameter of gold as measured by XRD in our experiment. It is estimated that this method is accurate to within 5%.^[39]

The study of material properties at very high pressures requires a hydrostatic environment free of shear stress. Solid media are convenient to load, but the presence of stress above 10 GPa leads to a non-uniform pressure distribution.^[33, 43] Gaseous media provide quasi-hydrostatic conditions up to pressures of 80 GPa or more,^[44] but loading gaseous material into the DAC is quite difficult. Therefore liquid media are most commonly used in DAC experiments. A blend of methanol and ethanol (4:1) is known to remain at least quasi-hydrostatic up to 10.4 GPa,^[33, 39] and this can be extended to higher pressures with the addition of water in a 16:3:1 (methanol : ethanol : water) blend.^[33, 45]

This blend was chosen for use in our SiC studies up to 55 GPa, and since we were studying nanoparticles rather than large, single crystals, we made the assumption that the loss of hydrostatic conditions would not be observable. This assumption was verified by comparing our results to experiments already performed on similar materials.

3.1.2 Beveled-culet DAC

The anvils used for higher pressure experiments differed in that an 8° bevel was cut into the culet, effectively reducing the culet face to $100\ \mu\text{m}$. The reduction in area magnified the obtainable pressure. The gasket material used in the beveled-culet DAC was rhenium, which is much harder and able to withstand greater pressures.^[46] Instead of measuring the thickness during pre-indentation, the pressure applied to the gasket was measured more precisely by placing a ruby chip on the culet face, pressing the anvils into the gasket, and measuring the fluorescence shift of the ruby signal. This method of pressure calibration will be described in greater detail later in this section. EDM was again used to drill the hole, but the diameter was much smaller, $50\ \mu\text{m}$, due to the smaller culet face.

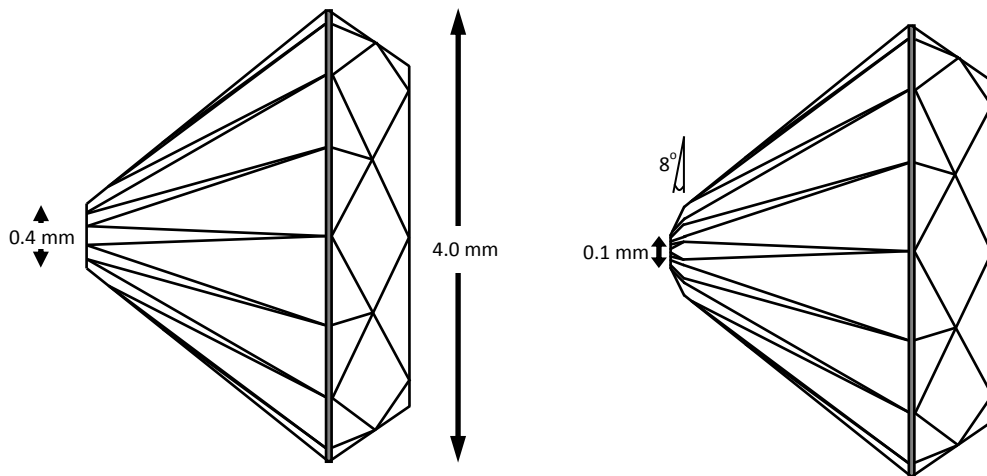


Figure 3.5 Flat culet and beveled diamond anvils.

Maintaining hydrostatic conditions becomes a difficult task at pressures above 60 GPa, and thus extra precaution was taken in the beveled-culet DAC. The sample, in powder form, was pressed between two microscope slides to form a thin wafer. A piece of this wafer less than 50 μm in size was chosen. It was turned upon its side, and its diameter was measured visibly through an optical microscope. The sample had to be thinner than the pre-indented gasket in order to ensure that the pressure medium would completely surround it and maintain the hydrostatic application of pressure. With this confirmed, the sample was loaded into the gasket hole.

Using gold for a calibrant was deemed unsuitable for this DAC. The strong diffraction from gold can easily overwhelm the weak silicon carbide diffraction, as was often seen in trial runs with the flat-culet DAC when too much gold was used. The reduced sample volume in the beveled-culet DAC led to an even weaker silicon carbide signal, and thus the permissible amount of gold would be reduced to a level impractical for loading. Therefore the more common ruby calibration method was used. In addition to the benefits already mentioned, the ruby method allows one to calibrate the pressure before conducting x-ray measurements. In contrast, the gold method requires XRD data to be collected and processed in order to check the pressure, which may prove the data to not be useful. A ruby chip was loaded next to the sample with great care so as to maintain an unobstructed optical path from the excitation laser.

It was first shown by Foreman et al. in 1972 that the ruby fluorescence lines shift linearly with hydrostatic pressures up to about 2.2 GPa.^[47,48] Further work by Barnett et al. in 1973 led to the popularity of ruby calibration in DAC studies.^[49] When excited with a laser at atmospheric pressure, the fluorescence of the R_1 and R_2 doublet, 6927 \AA

and 6942 Å respectively, is intense enough that only a 5-10 um chip of ruby is needed. Piermarini et al. used an equation of state to link the ruby scale to sodium chloride, thus demonstrating that the pressure-induced shift of ruby fluorescence lines was linear up to 19 GPa^[50], and this was later extended to 30 GPa^[46]. The accepted value for the R-line shift in this range is 3.65 Å/GPa.^[46] To test the linearity of the R-line shift beyond 30 GPa, Mao et al. conducted high pressure x-ray studies of copper, molybdenum, gold, and palladium^[51]. The shifting lattice parameters in conjunction with isothermal equations of state were compared to the ruby-calibrated pressures, and it was found that a small correction to the linear scale was needed.^[51] However, the assumption of linearity amounted to only a 3% error at 100 GPa, and so the linear approximation was used in this study.

The beveled culet DAC was intended for studies at much higher pressure than the flat culet DAC. Therefore to avoid inhomogeneous pressure distribution within the cell, the alcohol pressure medium was replaced with liquid argon. Argon gas was run through a liquid nitrogen bath in order to condense it to liquid form. The DAC, already loaded with the sample, was opened by a small amount and lowered into the liquid argon, thus allowing the argon to flow into the sample chamber. The DAC was then closed, trapping the argon inside with the sample and ruby.

Table 3.1 The details of experimental parameters pertaining to the two diamond anvil cell systems.

Experimental Parameter	Flat-culet DAC	Beveled-culet DAC
Culet face diameter	400 μm	100 μm
Gasket hole	200 μm	50 μm
Gasket material	Inconel	Rhenium
Pressure medium	Alcohol mixture	Argon
Pressure calibration	Gold diffraction	Ruby fluorescence spectrum
Maximum pressure obtained	55 GPa	75 GPa

3.2 X-ray Sources

3.2.1 Synchrotron Sources

The weak diffraction signal combined with the extremely small sample volume within a diamond anvil cell necessitates an enormously large x-ray flux to make any useful diffraction studies possible. The only source offering such an x-ray throughput is a synchrotron. Synchrotron radiation is derived from charged particles undergoing acceleration, the cultivation of which has its birth in high energy particle physics. Charged particles were accelerated to near the speed of light before being used in collision experiments, and it was recognized that the main source of power loss was due to emission of radiation, which existed in a smooth, continuous spectrum with high flux from the far infrared to x-rays. Given the potential for use in materials research, scientists began to gather this radiation during high energy experiments. As electrons were accelerated about a ring of bending magnets, the radiation was extracted tangentially.

Since these experiments were conducted parasitically to the high energy experiments, the synchrotron radiation was not as useful as that available today—the radiation strongly varied as the energy of the electrons was being ramped up for the collision experiments. Dedicated synchrotron laboratories were soon built employing storage rings to overcome this limitation. After being accelerated to sufficient speeds by various means, i.e. linear accelerators and booster rings, the electrons were dumped into the storage ring where bending magnets maintained their constant speed, and, subsequently, the synchrotron radiation was produced with a very stable spectrum.^[53]

Beyond the first generation sources, x-ray generation has been dominated by insertion devices known as wigglers and undulators. A wiggler, or a “second generation source”, is inserted into the storage ring and consists of a periodic array of magnets with alternating magnetic field orientations. The final product is the incoherent superposition of radiation produced at each pole of each magnet. The flux from a wiggler is increased by a factor of $2N$ from that of a bending magnet, where N is the number of oscillation periods. An undulator is similar to a wiggler, except that the radiation at each magnet pole is combined coherently, producing discrete spectral lines of even higher flux. Undulators have been dubbed the “third generation” sources.^[54]

The high pressure studies in this work were conducted at the National Synchrotron Light Source at Brookhaven National Laboratory in Upton, New York. Beamline X17B3 was used, which employed a superconducting wiggler. Sagittally bent silicon crystals were used to monochromate the beam^[55] at 30 keV, or a wavelength of 0.404067 Å. This beamline utilized a pinhole camera^[12] setup in which radiation was sent through the powder sample, and the diffracted beams were detected as concentric

rings on a Mar345 digital image plate. Due to physical limitations of the DACs, the diffraction range available for measurement was confined to $1^\circ \leq 2\theta \leq 20^\circ$. The small wavelength of the incident radiation, 0.404067 \AA , made this range comparable to the diffraction range $4^\circ \leq 2\theta \leq 80^\circ$ collected with Cu K_α x-rays, and this range was adequate for study of the most intense SiC reflections. The beam was focused to a size of $25 \mu\text{m} \times 25 \mu\text{m}$ with a K-B mirror.^[56] This was crucial in order to direct the radiation through the diamond anvil cell and the hole in its gasket, which measured $50 \mu\text{m}$ in diameter at its smallest. The raw data, an example of which is depicted in Figure 3.6, were integrated with the software Fit2D.^[57] The computer program Fityk^[58] was used to fit a sum of Voigt functions to the data, with each component of the sum corresponding to an x-ray diffraction peak. An example is shown in Figure 3.7, with the difference between the data and the fitting shown at the bottom.

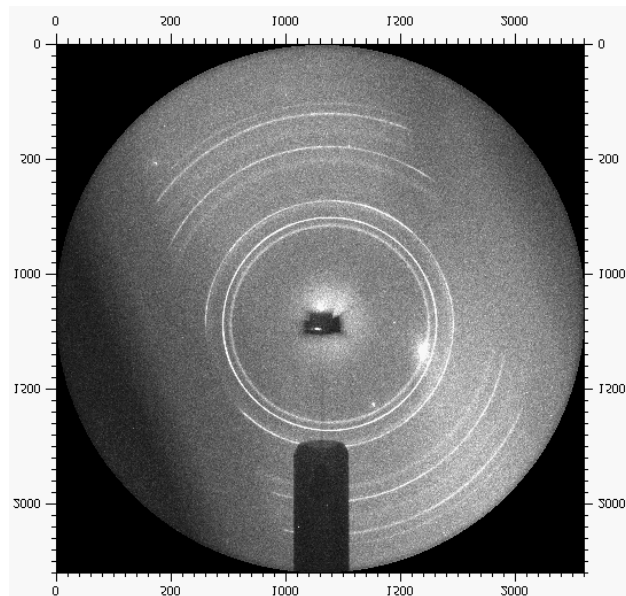


Figure 3.6 Raw data collected from the Mar345 image plate depicting diffraction from SiC nanowires in the flat-culet DAC.

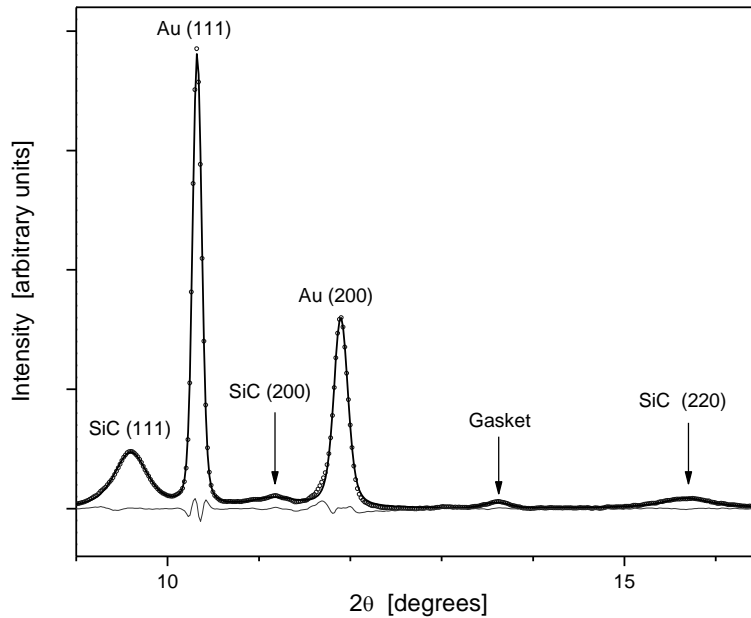


Figure 3.7 Raw data from Figure 3.6 integrated by Fit2D (open circles). The data are fitted with Fityk (solid line), and the difference between the data and the fitting is displayed by the bottom line. The (111), (200), and (220) reflections of SiC are seen, along with the (111) and (200) reflections of gold used for pressure calibration.

3.2.2 X-ray Tubes

It is not always practical to conduct x-ray experiments with synchrotrons sources. The construction and operation costs of such a facility limit their abundance, thus increasing the demands on a single synchrotron, and travel to a limited number of synchrotron facilities also proves to be a barrier. Therefore x-ray studies are much more commonly conducted with x-ray tube sources, which produce a much lower flux, and are poorly monochromated. However, the low cost and availability of the x-ray tube made it an adequate choice for all of the ambient-pressure studies reported in this work.

The very first x-rays discovered by Roentgen in 1895 came from gas x-ray tubes, in which x-rays were produced from the ionization of small quantities of gas, and these tubes were soon replaced by the filament tubes invented by Coolidge in 1913. This arrangement produces radiation by rapidly accelerating electrons and slamming them into a metal target. Therefore the three main components are 1) the filament from which electrons are emitted (usually tungsten), 2) an accelerating voltage (30kV in our case), and a metal target, which also serves as the anode (copper in our case). All of the components are sealed in an evacuated glass tube to minimize collisions with air molecules, and the metal anode is water-cooled to prevent melting due to all the heat produced during the collisions, see Figure 3.8.

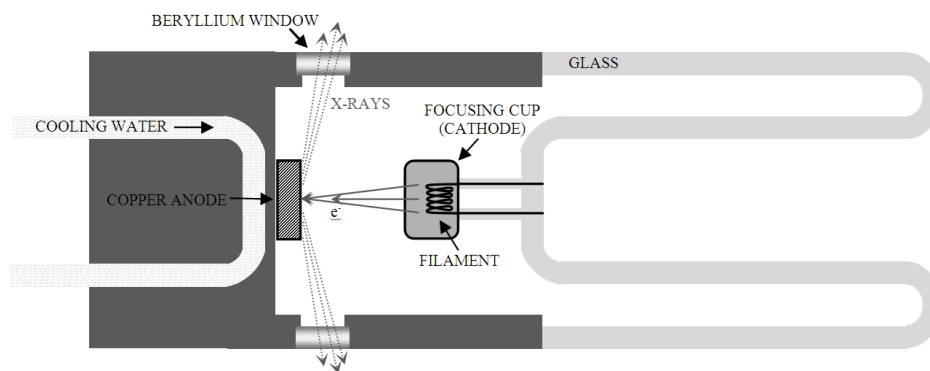


Figure 3.8 Schematic representation of a typical x-ray tube.

X-rays are produced in these tubes by two mechanisms, and the first to be addressed is the continuous, or bremsstrahlung, radiation. The collision of the electrons and the metal target produces such a deceleration of the charged electrons that radiation is emitted. Some electrons are stopped upon impact with the first atom of the target, while other electrons decelerate more slowly over several collisions. The varied condition by

which each electron decelerates produces a smooth spectrum which varies over many angstroms. Bremsstrahlung radiation is a poor source for x-ray studies, because the intensity is too low.

Luckily there is a second mechanism present in x-ray tubes which produces a much more intense, discrete spectrum of x-ray emission. When the accelerating voltage is raised beyond some critical level, the incident electrons may dislodge electrons from the low energy levels of the metal anode. The vacant energy levels left are then filled by electrons from higher energy levels, and the transition produces x-ray radiation. The *characteristic spectrum*, consists of narrow x-ray lines, grouped into several sets, K , L , M , etc., based upon the energy level from which the transition originates. It is named so, because the critical accelerating voltage as well as the energy of the emitted x-rays are characteristic of the anode's composition. Usually only the K lines are used, as the other lower energy lines are too easily absorbed. The subscripts α and β , are applied to denote lines produced by an electron transitioning to the K shell from the L shell and M shell, respectively. The K_α line is the strongest and is thus the obvious choice. So all other lines and the bremsstrahlung radiation must be filtered out by a monochromator. However, the K_α line is more appropriately referred to as the K_α *doublet*, as the fine structure of the L state produces two very closely spaced x-ray lines labeled $K_{\alpha 1}$ and $K_{\alpha 2}$. Their wavelengths are so close, 0.015 Å separation for copper, that they are usually unresolved, producing diffraction doublets that diverge with larger scattering angles, see Figure 3.9. Such doublet formation is an inherent disadvantage with x-ray tube sources that cannot be avoided in an easy or cost effective manner, so any analysis must take this into account.^[59]

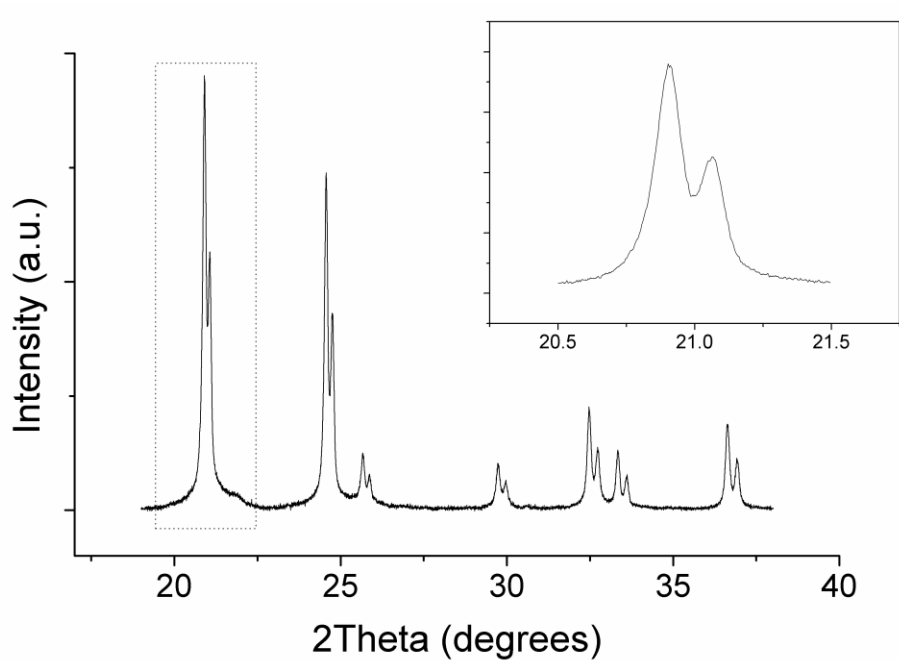


Figure 3.9 Divergence of the $K_{\alpha 1}$ and $K_{\alpha 2}$ lines seen in the diffraction data for SiC nanowires. The insert depicts a magnified view of the region in the dotted rectangle. Here a silver anode was employed with the $K_{\alpha 1}$ wavelength 0.5594205 \AA and the $K_{\alpha 2}$ wavelength 0.563811 \AA .

There are various means by which one may detect the diffracted data, but the most common setup for x-ray tubes is the use of a diffractometer in a θ - 2θ arrangement. In contrast to an image plate which will collect data in the form seen in Figure 3.6, a diffractometer will move along the angular range of diffraction and an angle equal to the angle of incidence. Because it is very difficult to bend x-rays, in practice, the sample is rotated which means the diffractometer must rotate at twice the angular rate in order to maintain the equivalence of the incident and reflected angles. So if the sample is titled at

angle θ , the diffractometer will be moved to angle 2θ as in Figure 3.10. The convention is to leave the data in the form in which it was collected, intensity versus 2θ .

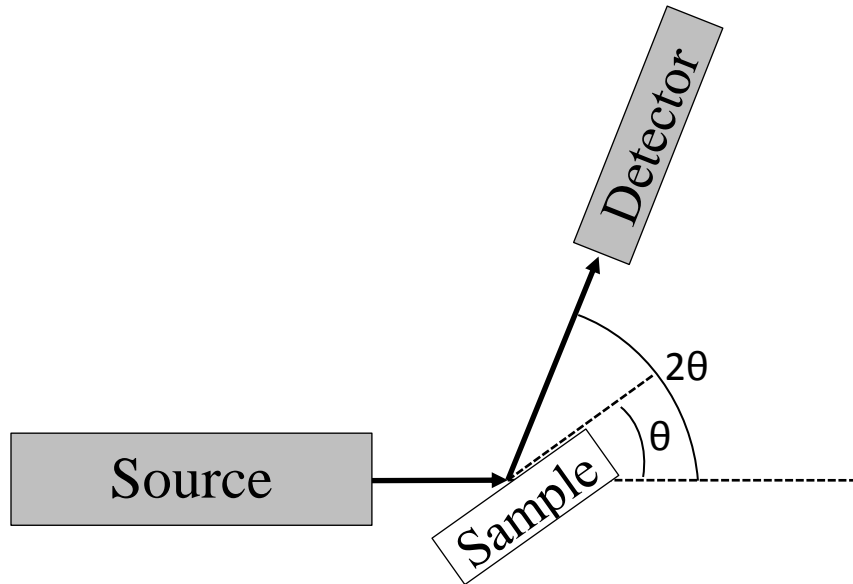


Figure 3.10 The θ - 2θ diffractometer arrangement.

The diffraction setup used for the microstructure analysis in Chapter V was manufactured by Phillips. It consists of an x-ray tube with a copper anode, producing x-rays with $K_{\alpha 1}$ wavelength 1.540562 Å. It operates at 30 kV accelerating voltage, with 30 μ A filament current. The data were recorded with a diffractometer in θ - 2θ arrangement described in Section 2.2.

3.3 TEM and EDS

Transmission Electron Microscopy (TEM) was necessary to observe the nanometer-sized samples. Since fast moving electrons may be treated as waves with very short wavelengths, according to de Broglie's formulation, they may be used in

microscopy to achieve very high resolution. The microscope was a JEOL2100 with a LaB₆ source. The accelerating voltage used was 200 kV, which was sufficiently high to penetrate the samples. Images were recorded on a digital Gatan camera. The microscope was capable of imaging in scanning mode (scanning transmission electron microscopy, or STEM), which facilitated energy dispersive x-ray spectroscopy (EDS). This technique provided information regarding composition based on x-rays emitted after electronic transitions resulting from the impact of electrons. The same mechanism is used to produce x-rays for diffraction, as was seen in section 3.2.2. Since the x-ray wavelength is dependent upon the atom being impacted, elemental composition can be determined.

The samples were first dispersed in toluene with an ultrasonic probe. A small drop of the suspension was applied to a copper grid. The grids were 300 mesh, which corresponds to openings around 50 μm in size--way too large to support nanowires as small as 10 nm in diameter. Therefore the grids were purchased with a thin carbon substrate on which the sample would be supported. Unfortunately the carbon in this substrate made it difficult for carbon levels in the sample to be quantified. So, when needed, lacey carbon substrates were used. These substrates had small holes in them across which a nanowire could lie for measurement.

3.4 FTIR

Fourier Transform Infrared Spectroscopy (FTIR) was employed to detect the vibrational characteristics of SiC nanowires. This data is complementary to EDS, which only determines the elements present. The equipment used was a Nexus 670 model manufactured by Thermo Nicolet. There are many sampling techniques used today, but

the Potassium Bromide (KBr) pellet is by far the most common. In this method, a powder sample is dispersed as evenly as possible in very finely ground and very pure KBr. The mixture is then pressed into a pellet so that the sample may be placed in the infrared beam for transmission measurements. The main benefit over other techniques is that KBr does not absorb in the typical range for infrared spectroscopy studies, 40 cm^{-1} to 4000 cm^{-1} ^[52]. However, KBr is highly hygroscopic and complete removal of water from the spectrum of KBr pellets is nearly impossible. Other techniques include sandwiching the sample with mineral oil between two KBr plates and dispersion in a volatile solvent before depositing on a substrate to dry. These latter techniques are less desirable, because they introduce new absorption bands into the infrared spectrum. However, they eliminate shifts due to the local field effect when the sample is embedded into the KBr matrix. This effect will be discussed further in Section 7.3.

Recent advances in attenuated total reflection (ATR) have made it a popular infrared sampling technique. Here the infrared beam is passed through a single crystal on top of which the sample is placed. The angle of the beam is such that total internal reflection occurs on that top surface, and an evanescent wave penetrates the sample to a depth dependent upon the composition of the single crystal, usually less than one micron. ATR provides the advantage that very dark materials such as carbon-filled polymers may be studied, whereas conventional transmission techniques would require very difficult, laborious, and expensive procedures to cut the material thin enough that total absorption does not occur. On that same note, most materials may be studied in the bulk form with ATR. These advantages are not pertinent to our study of SiC nanowires, but the advantages ATR provides us are the elimination of water from spectra and the local field

affects which both accompany the use of KBr pellets. ATR also eliminates foreign species in the spectrum from mineral oil or volatile solvents. Maybe most noticeable is the ease with which ATR measurements are conducted, as the powder sample is simply pressed on top of a relatively large crystal. However, the hardness of SiC means that our selection of crystals is very limited. Germanium is not usable because SiC will easily scratch germanium, or even become embedded in the crystal. Therefore diamond is the only suitable choice, as it is the only material harder than SiC. The choice of diamond comes at a price, because diamond absorbs a large portion of infrared light in the 1700 - 2700 cm^{-1} range, see Figure 3.11.

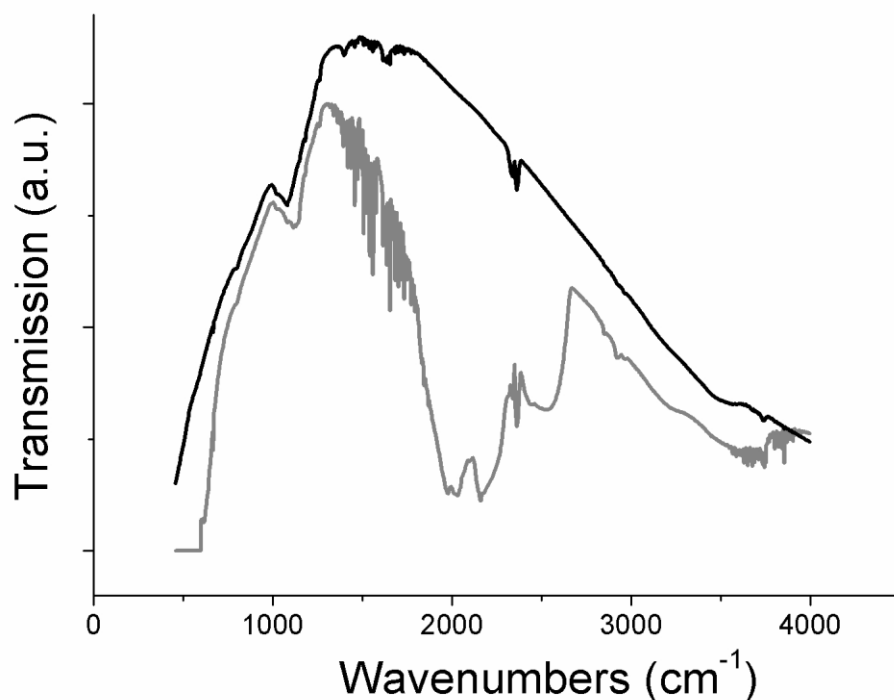


Figure 3.11 Infrared absorption of Diamond. The black line is the background from the conventional transmission arrangement. The grey line is the background collected from same equipment with the addition of the Diamond ATR attachment

The range in which diamond is not infrared transparent is of vital importance to our study, so the KBr pellet technique was used for all spectra reported in this paper. The samples were prepared by first heating them to 200°C to reduce adsorbed water. Each sample was then ball milled with 0.5 g of KBr for 30 seconds, and the product was loaded into a 13 mm pellet press with the capability to be evacuated. Then 7 metric tons of pressure was applied from a hydraulic press, and a rotary pump evacuated the pellet press for 20 minutes to reduce moisture in the sample. Pressure was slowly released, and the sample, now in the form of a pellet, was removed for measurement.

CHAPTER 4: SYNTHESIS

4.1 Overview of Synthesis Methods Existing

Currently there exist many methods for the synthesis of nanowires. Template-assisted synthesis confines the material to grow in nanosized pores of hard materials such as anodic alumina, nanochannel glass, ion track-etched polymers and mica films.^[62] Materials with low melting points may simply be injected in the liquid form into the templates, but the template must be able to withstand the temperatures and pressures involved.^[63-65] Alternatively, nanowires may be grown in templates by electrochemical deposition, which has been used extensively to create thin films. In this method, a thin metal film is deposited on one side of the template to serve as a cathode for electroplating.^[66, 67, 69-78] In the physical deposition method, a material is heated and the subsequent vapor is passed through the template, where it cools into nanowires^[79]. Compound materials may be created by a chemical deposition method, and one successful method involves filling the pores of a template with a liquid that then reacts with a gas atmosphere.^[80, 81] Other methods of SiC nanowire production include the sol-gel process, the vapor-liquid-solid process (VLS), and reactions between silicon vapor and carbon black or graphite. The major goal in all these techniques is the control of the desired parameters, such as diameter, length, and concentrations of various defects.

The aforementioned techniques produce straight, uniform wires of narrow diameter, but these techniques have numerous limitations. Most importantly, the need for precursors in the liquid/gaseous states eliminates the possibility of working with materials having high melting/boiling points such as silicon carbide. Secondly, the yield

of template-assisted methods or many VLS methods is very low and the cost is very high, making them undesirable for future industrial applications.

4.2 SiC Nanowire Synthesis by Nanotube Confinement

In recent years, a new method of producing SiC nanowires in relatively large quantities and reduced expense has been developed utilizing the reaction between multiwalled carbon nanotubes (MWCNT) and micron-sized silicon powder. The reaction takes place at high temperature and is done under vacuum to prevent the loss of MWCNTs to oxidation.^[82] This method has been used to produce the SiC nanowires analyzed in this work, and the experimental apparatus has been modified to allow more control and reproducibility through the adjustment of the partial pressure of silicon. All SiC nanowire samples started with MWCNT precursors that ranged in outer diameter from 15 nm to 100 nm and were manufactured by NanoAmor, Inc.

4.2.1 Sample Vessel

The reactions were carried out in a quartz tube having both reactants separated. Quartz was chosen, because it is relatively easy to make airtight seals, and it has a very high melting point. The MWCNTs were contained within an inner quartz vial for easy removal, and the outer tube was crimped to hold the vial in place. The location of this crimp was determined by the desired separation distance of the reactants, and thus the desired partial vapor pressure of silicon, to be described in the next section. A rotary pump evacuated the tube to approximately 130 mPa (~1 millitorr) before the tube was

sealed with a hydrogen/oxygen torch. This complete assembly shall be referred to from this point forward as the sample “ampoule.”

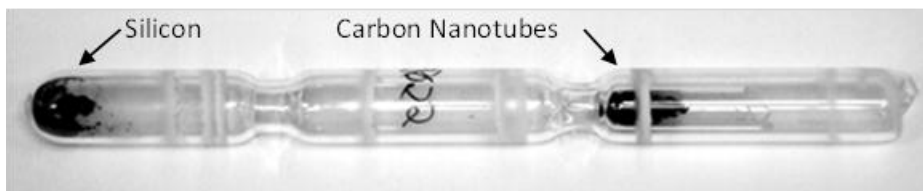


Figure 4.1 Photograph of a typical sample ampoule.

4.2.2 Tube Furnace

The partial pressure of silicon was manipulated by utilization of a two-temperature experimental design. A substance’s vapor pressure is determined by its temperature, and so the temperature to which the sample ampoule is exposed will determine the vapor pressure inside the ampoule. However, it was determined that high temperatures (around 1200°C) were necessary for the silicon vapor to react with MWCNTs. Therefore the ampoule was designed to be long enough in order to maintain the MWCNTs at a much higher pressure than the silicon, and the silicon’s vapor pressure was thusly manipulated by controlling the pressure at the cold end containing silicon. The lowest known carbon vapor pressure was measured at 1700°C, and it is nine orders of magnitude lower than that of silicon at this temperature.^[83] Consequently, our neglect of carbon’s partial pressure is justified.

A tube furnace was employed for two reasons, the first of which being the prevention of ampoule collapse. Quartz begins to soften around 1200°C, and thus atmospheric pressure outside the evacuated ampoule can often cause the ampoule to

collapse in on itself. Therefore the ampoule was heated inside a tube furnace consisting of two very pure alumina tubes. The alumina tubes were evacuated to less than 133 mPa (1 millitorr) after the sample ampoule was deposited inside. Alleviating the pressure differential between the inside and the outside of the ampoules prevented their collapse.

The vacuum inside the alumina tubes was also needed to prevent oxidation of the quartz ampoules. Often when the ampoules were heated in air to temperatures around 1200°C, the oxidation of the ampoules would lead to cracking. It was common for this cracking to be so severe that the vacuum inside the ampoule would be compromised before the desired sintering time was reached. Removal of the oxygen surrounding the ampoules alleviated this problem. After sintering, the portions of the ampoules containing silicon powder were sealed off to prevent contamination of the silicon carbide product.

The Burrell tube furnace used for the experiments needed modification in order to maintain stable temperatures. An Omega CNI3244-C24 controller was connected to both the furnace's thermocouple and an Omega SSR240DC50 solid state relay. The relay was connected in series with the heating elements, and it cut the flow of electricity when the thermocouple surpassed the specified setpoint. The controller was equipped with proportional integral derivative capabilities which refined the on/off power cycling in order to minimize ramp up time while also stabilizing the temperature at the desired set point.

4.2.3 Manipulation of Temperature

The temperature of silicon was manipulated by exploiting the temperature variance along the length of the tube furnace. For this reason, an accurate measurement of the temperature distribution was essential. The furnace was heated to 1200°C, as determined by the S-type thermocouple (platinum/10% rhodium blend versus platinum interface) mounted at the center of the furnace. After stabilization, the temperature distribution was measured in 0.5 cm increments with a K-type (chromel versus alumel interface) thermocouple. This information was collected at several furnace setpoints, as can be seen in Figure 4.2. The temperature near the center of the furnace changed less than 3°C per cm. The MWCNT were always placed here, while the silicon was placed at a distance corresponding to the chosen, lower temperature.

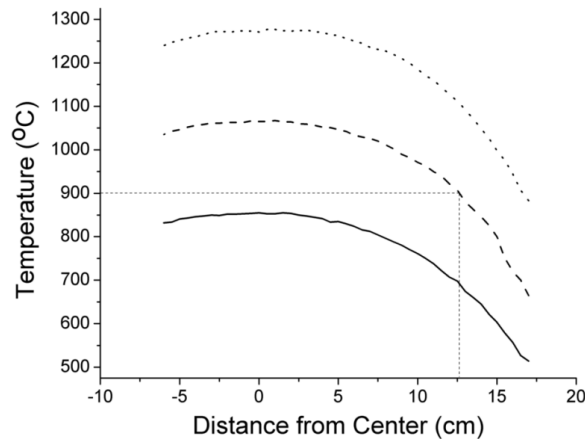


Figure 4.2 Temperature distribution of the tube furnace collected at three setpoints: 800°C (solid line), 1000°C (dashed line), and 1200°C (dotted line). As an example, dotted, straight lines are drawn to demonstrate that a desired silicon temperature of 900°C would require an ampoule 12.7 cm long. The MWCNT at the other end of the ampoule would thus be at 1063.4°C.

4.2.4 Calculation of Yield by XRD

We expected that varying the silicon vapor pressure and sintering time would have an effect on the rate at which the reaction progressed, so a method of quantifying the SiC formed during sintering was necessary. Following the procedure developed by Pantea^[84], we determined the correlation between XRD peak intensities and the molar content of SiC in a particular specimen. Silicon carbide powder was mixed with MWCNTs in varying mass concentrations. X-ray diffractograms were collected from each mixture with a Phillips PW2773 diffractometer producing copper K_{α} radiation, $\lambda=1.54\text{\AA}$.

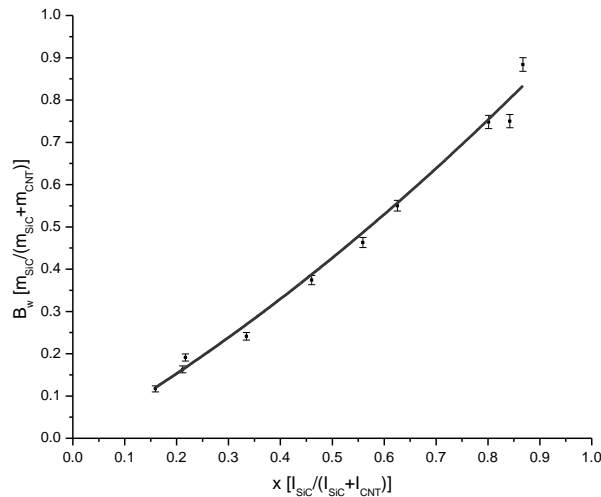


Figure 4.3 Calibration curve used to determine the yield of a reaction. The intensity ratio on the horizontal axis is defined by Equation 4.1, while the mass ratio on the vertical axis is defined by Equation 4.2.

The XRD data were fitted to a sum of Voigt functions, each representing one reflection. The intensity ratios of the various mixtures were denoted as x :

$$x = \frac{I_{SiC}}{I_{SiC} + I_{CNT}} \quad (4-1)$$

where I_{SiC} is the intensity of the (111) peak of SiC, and I_{CNT} is the intensity of the reflection due to MWCNT at $2\theta = 26.28^\circ$ ($\lambda=1.54\text{\AA}$). These intensities refer to the area under the peak of their respective Voigt function. The mass content of SiC was defined in a manner similar to Equation (4-1):

$$B_{mass} = \frac{m_{SiC}}{m_{SiC} + m_{CNT}} \quad (4-2)$$

where m_{SiC} is the mass of silicon carbide and m_{CNT} is the mass of MWCNT. The plot of x versus B_{mass} results in a second order parabolic function of the form

$$B_{mass} = C_1x^2 + C_2x + C_3 \quad (4-3)$$

where C_1 , C_2 , and C_3 are constants. C_3 was eliminated, because B_{mass} must be zero when x is zero. Also, when x is unity, B_{mass} is equivalent. This reduced Equation (4-3) to the following form:

$$B_{mass} = C_1x^2 + (1 - C_1)x \quad (4-4)$$

B_{mass} was plotted against x (see Figure 4.3) and Equation (4-4) was fitted to the data, yielding the constant C_1 : 0.2930+/- 0.024. Substituting C_1 into Equation (4-4) produced Equation (4-5) by which the mass content of SiC was determined via XRD.

$$B_{mass} = 0.29308x^2 + 0.70692x \quad (4-5)$$

Finally, the mass content was converted to molar content by Equation (4-6) in order to better judge the completeness of the reaction.

$$B_{mol} = \frac{B_{mass}}{\frac{m_c + m_{SiC}}{m_{SiC}}(1 - B_{mass}) + B_{mass}} \quad (4-6)$$

Sintering time and vapor pressure were isolated, and the effects of these respective variables on the reaction rate and nanowire diameters were analyzed.

4.2.5 Effects of Sintering Time

Silicon carbide nanowire samples were prepared with varying sintering times. In this series of experiments, the temperature of silicon was held constant at 1000°C, which corresponds to a vapor pressure of approximately 1 mPa. As can be seen in Figure 4.4, the reaction clearly progressed linearly with respect to time. The nanowire diameters were measured by TEM, and lognormal distributions were fitted to each data set (see Figure 4.5). Although each sample contained nanowires of varied diameters, the lognormal distributions widened and shifted toward larger diameters with increasing sintering time. The peaks of the distributions ranged from 49 nm with 3 hours sintering to 76 nm with 52 hours sintering. It was noted that a sample sintered for 52 hours produced a few very large wires with diameters of several hundred nanometers, (see Figure 4.6). These diameters were much larger than the diameters of their precursor MWCNTs (60 nm to 100 nm).

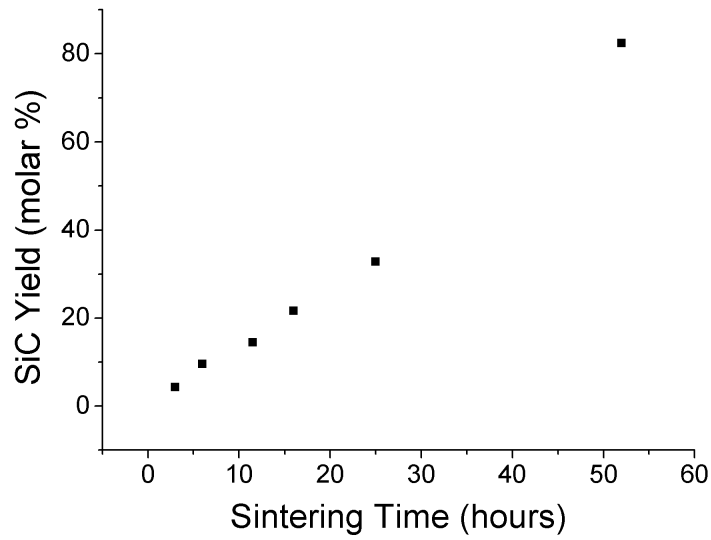


Figure 4.4 SiC yield as a function of sintering time.

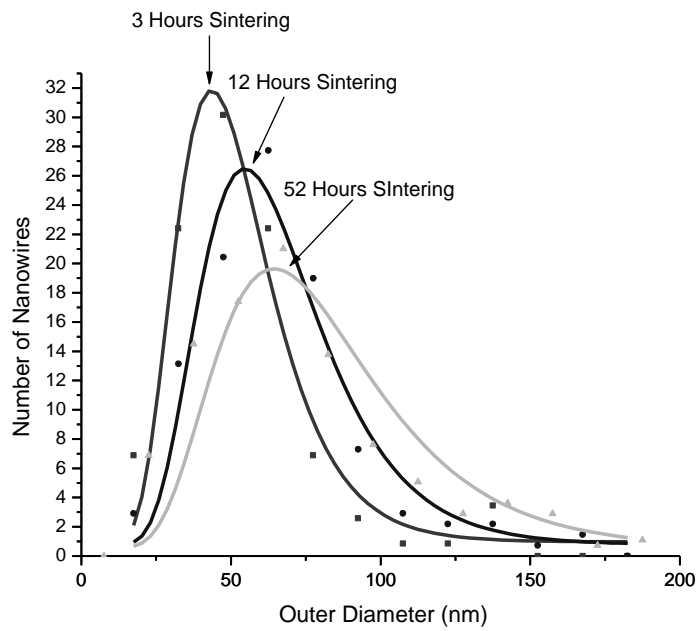


Figure 4.5 Influence of sintering on nanowire diameters. It is seen that longer sintering times result in distributions shifted towards larger diameters.

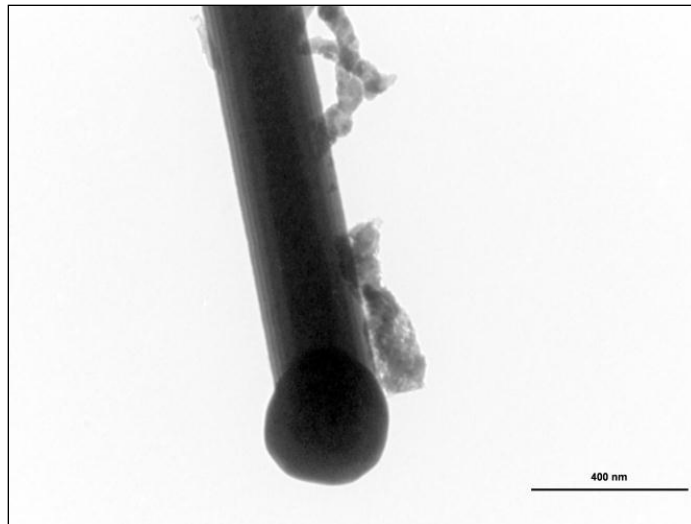


Figure 4.6 TEM image of a sample sintered for 52 hours.

4.2.6 Effects of Vapor Pressure

The SiC nanowire reaction was also investigated in terms of the vapor pressure. In these experiments, the sintering time was held constant at 16 hours, and the sintering temperature (temperature of the MWCNTs) was maintained at 1200°C. The length of the ampoule was varied so that the silicon temperature would vary by 25°C-50°C with each successive experiment: 1000°C, 1050°C, 1100°C, 1125°C, 1150°C, 1175°C, and 1200°C. The data reported by Nesmeyanov^[83] was used to determine the partial pressure of silicon corresponding to these temperatures, and the results are plotted in Figure 4.7. A sharp increase in the yield appeared between 15 mPa and 25 mPa of Si vapor pressure. Therefore 25 mPa was the chosen partial pressure of Si for future experiments. However, the error involved in these calculations is quite large, and thus a definitive trend cannot be established.

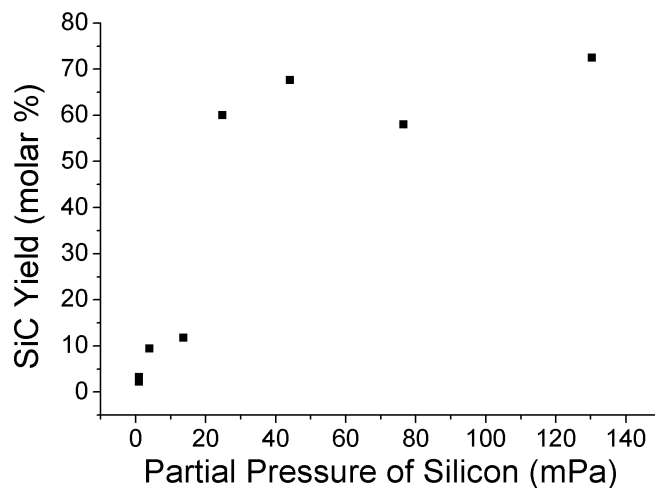


Figure 4.7 The effect of silicon vapor pressure on the SiC yield.

4.3 Growth Mechanism

4.3.1 VLS Mechanism

The mechanism of SiC nanowires formation in the synthesis method described above remains controversial, but when metals were present in carbon nanotube precursors, the growth mechanism was identified as the vapor-liquid-solid (VLS) process.^[85] Currently, the VLS method is the most popular amongst researchers for nanowire synthesis. Details of the usual experimental method are as follows: metal droplets are deposited by various means onto a substrate. A source material is then introduced in the vapor phase, which is absorbed by the metal droplet. When the metal droplet has become supersaturated, it begins to deposit the material onto the substrate, which acts as the seed of nucleation. This method was first employed to form silicon nanowires on a silicon substrate through gold droplets. The size of the wires may be controlled by the size of the metal droplets.^[86] This process has even been observed *in*

situ via Transmission Electron Microscopy.^[87] It is further known that the wires may form kinks whenever the substrate temperature or the vapor pressure is changed.^[88]

In the MWCNT method described in this paper, the metal catalyst originates as a trace element left over from the MWCNT production process. This metal was identified as iron, which has 0.12% abundance in the MWCNT precursor.^[89] The VLS process is identified by “flowers” from which one or many SiC nanowires may originate. When EDS is performed, iron is found in relatively large quantities within the flowers, as seen in Figure 4.8. It must be noted that a large relative concentration of oxygen is found in the flower, indicating that an oxygen containing molecule, such as SiO may be responsible for transporting the silicon to the MWCNT.

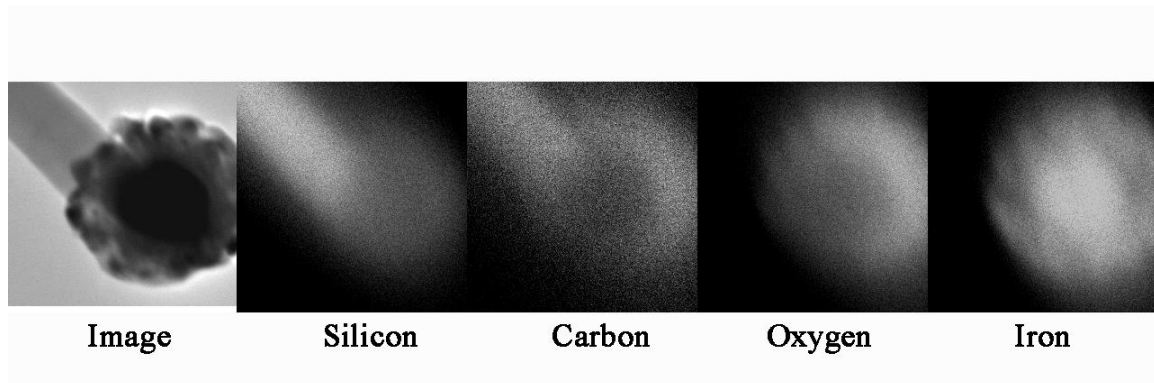


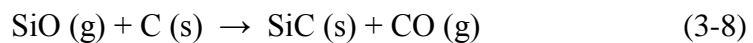
Figure 4.8 STEM image and EDS maps of four elements found within the same SiC nanoflower. In the EDS maps, lighter areas represent areas with higher concentrations of the specified element.

4.3.2 VS mechanism

The low abundance of catalyst material makes it very improbable that the VLS method alone is responsible for the large abundance of SiC wires. It has been

demonstrated that SiC wires may be grown from highly oriented pyrolytic graphite and carbon blacks, both of which are free of metal catalysts.^[90] Hence one must assume that the vapor-solid (VS) mechanism was the most predominate source of SiC wires. In this mechanism, a silicon atom from the vapor phase (silicon vapor or silicon dioxide) deposits on the carbon nanotube substrate, where it migrates on the surface until it evaporates back into the vapor. If the surface of the MWCNT has no structural imperfections, the silicon atom is not likely to chemically bond with the carbon atoms. If, however, the migrating atom encounters some structural imperfection in the MWCNT substrate, the atom finds itself in a corner where carbon atoms from two surfaces may form chemical bonds via their unfilled orbitals. This bonded silicon atom forms a nucleus to which other migrating silicon bonds may form.

In reality, this process is likely to be more complicated with several intermediary steps. Quartz is known to adsorb air molecules including oxygen, which it then releases at high temperatures. So it is conceivable that the oxygen released from the quartz ampoule reacted with the silicon vapor to form silicon monoxide vapor that reacted with the CNTs in the following manner:



Such a reaction is often reported by other researchers.^[91-93] However, we found that heating the ampoule to 325°C and evacuating with a diffusion pump to 10⁻⁴ pascal (~10⁻⁶ torr) before sealing, the yield of the reaction was increased dramatically. Such a process would remove a great deal of oxygen adsorbed into the walls of the container. Therefore it must be concluded that the reaction involves pure silicon vapor, or silicon monoxide liberated from the quartz (SiO₂) itself.

Experimental results clearly indicate that CNTs possess many defects; for example, Mawhinney et al.^[94] reported that several percent of carbon atoms on the carbon nanotube walls can be located at the defective sites, thus providing ample opportunity for silicon bonding. Such defects are depicted in Figure 4.9. The most common defects are the so-called Stone-Wales (SW) defects,^[95-97] which are pairs of adjacent 5 and 7 member rings, see Figure 4.10. The SW defects are formed unavoidably during nanotube synthesis process, since the additional pairing of a heptagon with a pentagon is energetically favorable. High concentration of these defects may lead to tube bending and changed diameter. We have observed this behavior in TEM images of carbon nanotubes recorded prior to the reaction with silicon. It is generally accepted that SW defect sites trigger chemical reactions between carbon nanotubes and other materials.^[98, 99] At high temperatures, the population of these defects is probably increased. Here it must be noted that the manufacturing of SiC nanowires takes place at temperatures between 1100°C and 1350°C. In addition, SW defects can glide, twist, and distort, and thereby some C-C bonds may break. It is then energetically favorable for these dangling bonds to react with Si atoms. Of course, other defects such as vacancies, impurities, and kinks may also be present and constitute nuclei for the reaction, and the combined effect of various defects could further lower the activation energy.

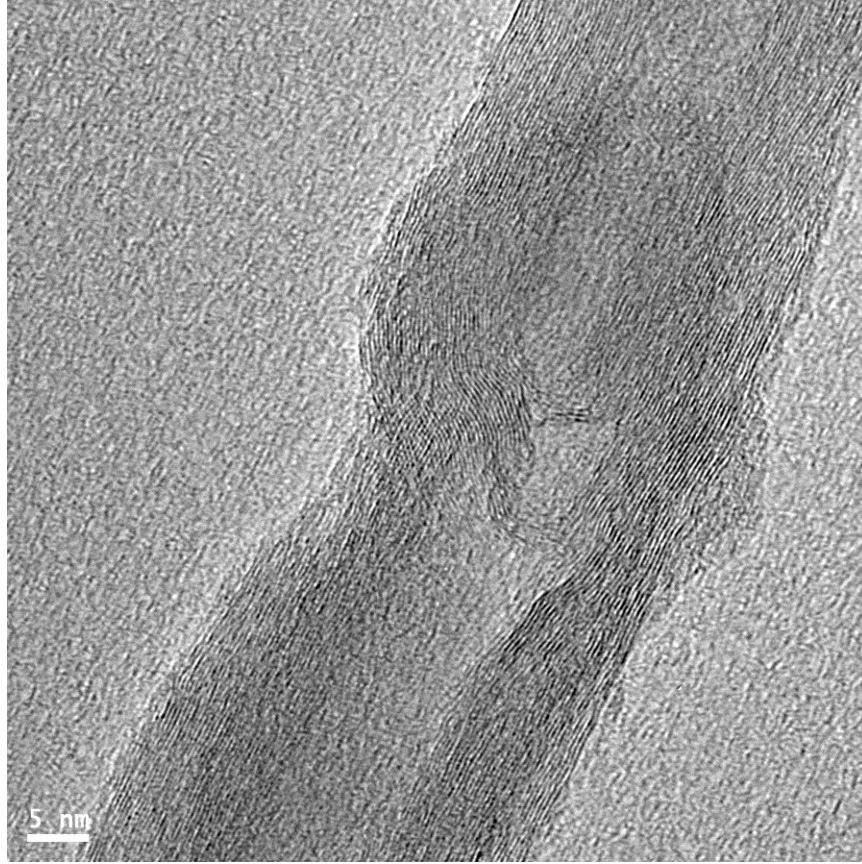


Figure 4.9 TEM image of unspecified defects in a MWCNT.

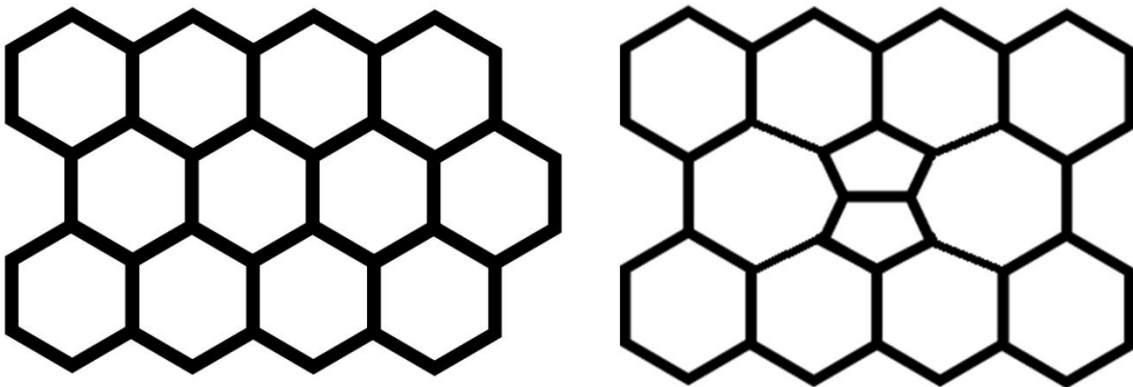


Figure 4.10 A model of a graphene sheet that rolls to form a carbon nanotube. It is shown without defects (left) and with Stone-Wales defects (right).

We assume that the reaction with silicon starts at SW defects or other defects on outer walls of multiwall carbon nanotubes. Then SiC grows not only along the tube outer walls but also radially, and the high density of defects results in numerous nucleation sites. As the grains grow they coalesce. Of course, continuing the reaction for an extended period of time at a high temperature facilitates growth of the crystallites. Once the SiC layer coats the exterior of the carbon nanotube, to continue the reaction, carbon atoms must diffuse through the newly formed SiC layer to the outer surface to react with silicon, or silicon atoms must migrate toward the carbon rich area. As silicon diffuses into the interior of the coaxial structure it transforms carbon nanotubes into SiC and eventually the interior becomes solid SiC. The outer diameter of the nanowires also grows indicating that carbon atoms continue to diffuse through the SiC layers. The outermost layers of SiC nanowires are composed of amorphous silicon carbide, SiO_x, and various carbon functional groups, which is evidence for the reaction described by Equation (3-8).

A layer of SiC formed on carbon substrate, initially thin, grows with reaction time. Diffusion coefficients of both carbon and silicon atoms in crystalline SiC are very small,^[100-103] and, to explain the rapid growth of SiC, we assume that it proceeds mainly by diffusion of those atoms along grain boundaries, stacking faults, and dislocations. Pantea et al.^[105] observed this effect in diamond composites in which the diffusion of carbon and silicon atoms was enhanced by the presence of structural defects and extensive grain boundaries.

4.3.3 Ostwald Ripening

When specimens were allowed to reside at elevated temperatures for a long time, longer than 4 hours, a different process known as Ostwald ripening started, and large diameter nanowires continued to grow at the expense of smaller wires. Smaller nanowires produce larger vapor pressure due to their larger surface area per unit mass. It logically follows that large nanowires produce lesser vapor pressures, and, in order to maintain equilibrium, smaller particles evaporate into surrounding medium with a rate inversely proportional to the radius. The specimens discussed in this article had average size of about 30 nm and were produced in times for which the Ostwald ripening was not significant.

4.4 SiC Nanowires Used in This Research

The silicon carbide nanowires used in the high pressure studies were sintered for one hour. The precursors were 1) MWCNTs with 10-30 nm diameters and 5-10 micrometer lengths manufactured by NanoAmor, Inc. of Houston, TX and 2) silicon powder with particles smaller than 44 μm (~325 mesh) manufactured by the Sigma-Aldrich Corporation of Saint Louis, MO. The silicon was held at 1200°C, while the MWCNTs were held at 1250°C. For comparison, high pressure studies were also conducted upon commercially available SiC grains, which allowed morphology and size to be studied simultaneously. The grains measured 20 nm, 50 nm, and 130 nm in diameter and were manufactured by NanoAmor, Inc.

After completing the high pressure studies, it was determined that the diameters of the nanowires were more controllable if the silicon partial vapor pressure was kept

low. This meant that longer sintering times were required, but the low silicon pressure prevented the reaction from proceeding too quickly. Also, elevated MWCNT temperatures produced even more desirable results in this configuration. Thus the SiC nanowires produced for the microstructure and surface studies were produced in the following conditions: the silicon was held at 1125°C, the MWCNTs were held at 1325°C, and they were sintered for 16 hours. As with the high pressure study, the silicon and MWCNTs were manufactured by NanoAmor and Sigma-Aldrich, respectively.

CHAPTER 5: HIGH PRESSURE EXPERIMENTS

5.1 Motivation

As silicon carbide is a material with numerous advantages in harsh conditions, SiC nanoparticles will most definitely be sought out for applications in the most extreme of such cases: high pressure, high temperature, and high abrasion. Thus it is imperative to know how these materials behave in a wide range of experimental conditions. For this work, the isothermal application of pressure was employed to investigate SiC's most well-known and often-applied property: very high hardness, quantified in terms of its bulk modulus. Experimental results are scant and report the bulk modulus of bulk SiC from 203 GPa^[106] to 260 GPa.^[107] The bulk moduli obtained from nanocrystalline SiC are reported to be within this same range.^[108] However, the experimental techniques employed are relatively new and are still evolving. As shown by Liu et al, the choice of pressure medium and, subsequently, the degree to which hydrostatic conditions are maintained may greatly affect the results of DAC measurements.^[109] Therefore it is impossible to judge the effect or non-effect of confinement given mixed methodologies of the available data. A consistent, controlled investigation is needed to show that the bulk moduli of nano-sized SiC particles are indeed elevated in comparison with the bulk material. Such a conclusion is suspected due to the behavior of silicon nanowires, which exhibited a 25% increase in bulk modulus compared to that of the bulk material.^[115]

SiC exists in over 100 different polytypes due to differences in the stacking of the silicon-carbon bilayers, and these different atomic arrangements determine the physical properties of the substance. Therefore, understanding how to control the polytype will

allow SiC to be tailored to the specific needs of an application or harsh operating conditions. For example, 3C-SiC (also referred to as the β phase) is known to withstand high temperatures and radiation, while interest in 6H-SiC (the α phase) is if focused on its use as a blue-light emitting diode. Currently, the pressure-induced transition between the β and α is poorly understood. Simulations have produced very inconsistent predictions of the phase transition point, varying between 66 GPa to 600 GPa,^[110-112] while the experimental results are quite sparse, due to the extreme difficulty in studies conducted at such high pressures. Shock compression data has shown the transition to the α phase to be complete at 100 GPa, but has not determined the actual transition point. Yoshida et al, used the diamond anvil cell to determine that the transition occurs at 100 GPa,^[113] though the authors used an alcohol medium which has been shown to crystallize at much lower pressures.^[109] Thus the pressure applied was very likely not hydrostatic.

While not much is known about the β - α transition of SiC, even less is known about the manner in which spatial confinement affects this transition. High pressure investigations of other materials have, in many cases, resulted in lowered phase transition points. For example, it was demonstrated that the Si I-II transition point in 60-80 nm diameter silicon nanowires was reduced 2 GPa in comparison with bulk material.^[115] Thus the same is expected to be true of SiC nanowires.

5.2 Results

The XRD peaks of SiC were seen to shift to higher angles with increasing pressure, an example of which is shown in Figure 5.1. The experimental XRD profiles consisted of three reflections due to SiC, four due to gold, and two from the gasket and so

a sum of nine Voigt functions were fitted to experimental contours in order to determine the peak locations. Figure 5.2 illustrates one of these reflections—the (111) reflection of SiC. The fitting quality proved to be excellent, allowing precise determination of the peak location within 0.00151° from the point of highest intensity. The quality of the fits for the SiC (220) reflection was equally good, but many times the SiC (200) statistics were too poor to allow its use in comparison with other experimental runs. Therefore attention was focused on the SiC (111) and (220) reflections.

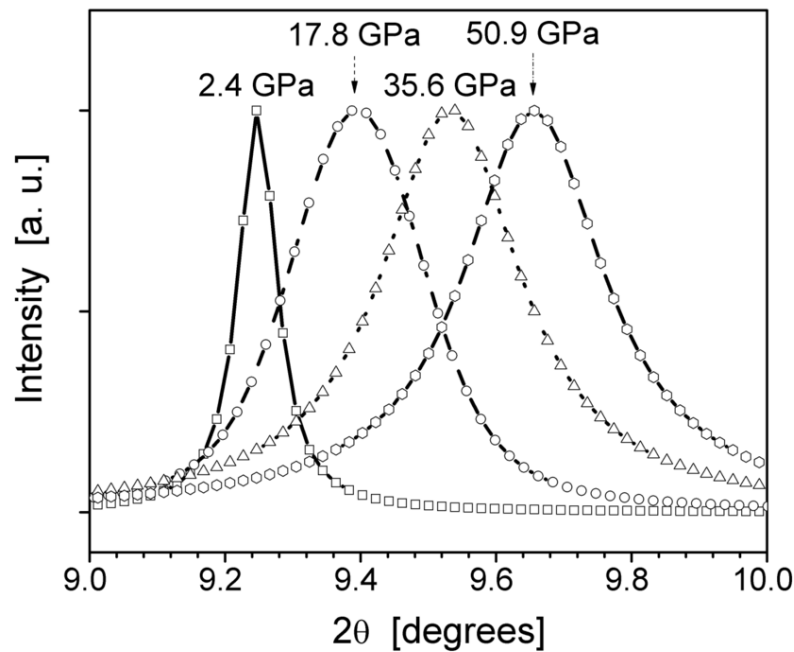


Figure 5.1 Pressure induced shift of the (111) reflection from SiC nanowires. To guide the eye, experimental points recorded at different pressures are connected by lines.

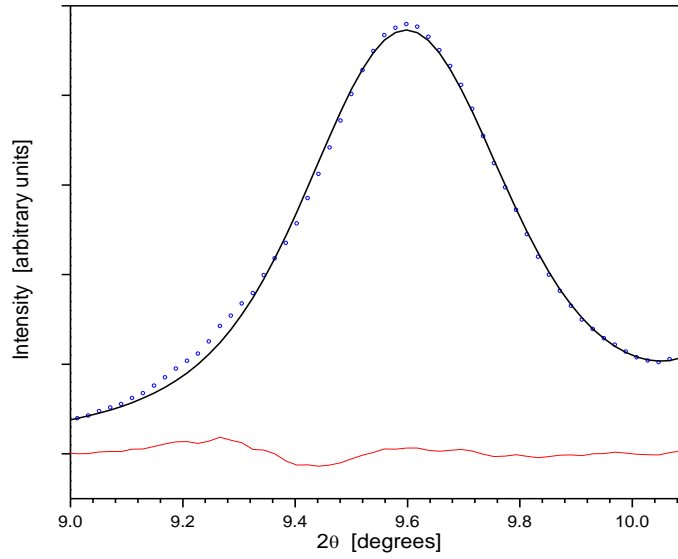


Figure 5.2 Mathematical fitting of the (111) reflection of SiC. Data collected at NSLS with $\lambda = 0.404067 \text{ \AA}$ on 130 nm grains of SiC at 35 GPa.

Calculations were then performed on the information collected by the fitting. Equation (2-19) was used to calculate the lattice constant from the location of the peak centers, and the results of these calculations are shown in Table 5.1 and Figure 5.3. The error in the calculation, δa , was produced by the usual method:

$$\delta a = \frac{a}{2} \cot\left(\frac{(2\theta)}{2}\right) \delta(2\theta) + \frac{\sqrt{h^2 + k^2 + l^2}}{2 \sin\left(\frac{(2\theta)}{2}\right)} \delta(\lambda)$$

where $\delta(2\theta)$ is the error in the peak location determined by the Fityk program, and $\delta(\lambda)$ is uncertainty in the x-ray wavelength. The error involved in the wavelength is on the order of 10^{-3} to 10^{-4} %, and so the second term was neglected. The pressures listed were calculated by application of Equation (3-7) to the (111) reflection of gold. It is seen in all

samples that the lattice parameter decreases as pressure increases (see Figure 5.3). This result is expected, because the high pressure should indeed push atoms closer together.

Table 5.1 High-pressure lattice parameter data with errors.

20 nm Grains		50 nm Grains		130 nm Grains		Nanowires	
P (GPa)	a (Å)	P (GPa)	a (Å)	P (GPa)	a (Å)	P (GPa)	a (Å)
2.6	4.34 ± 0.01	2.4	4.341 ± 0.002	1.9	4.337 ± 0.001	1.9	4.364 ± 0.004
20.4	4.24 ± 0.01	5.0	4.326 ± 0.009	15.3	4.27 ± 0.01	2.4	4.341 ± 0.001
39.0	4.21 ± 0.01	10.9	4.29 ± 0.02	22.9	4.221 ± 0.007	17.8	4.273 ± 0.005
55.8	4.16 ± 0.01	14.3	4.277 ± 0.004	29.9	4.205 ± 0.004	35.6	4.211 ± 0.004
		19.2	4.26 ± 0.01	35.3	4.183 ± 0.006	46.0	4.17 ± 0.02
		26.3	4.24 ± 0.09	40.6	4.159 ± 0.003	50.9	4.157 ± 0.005
		35.5	4.204 ± 0.007	48.2	4.130 ± 0.002		

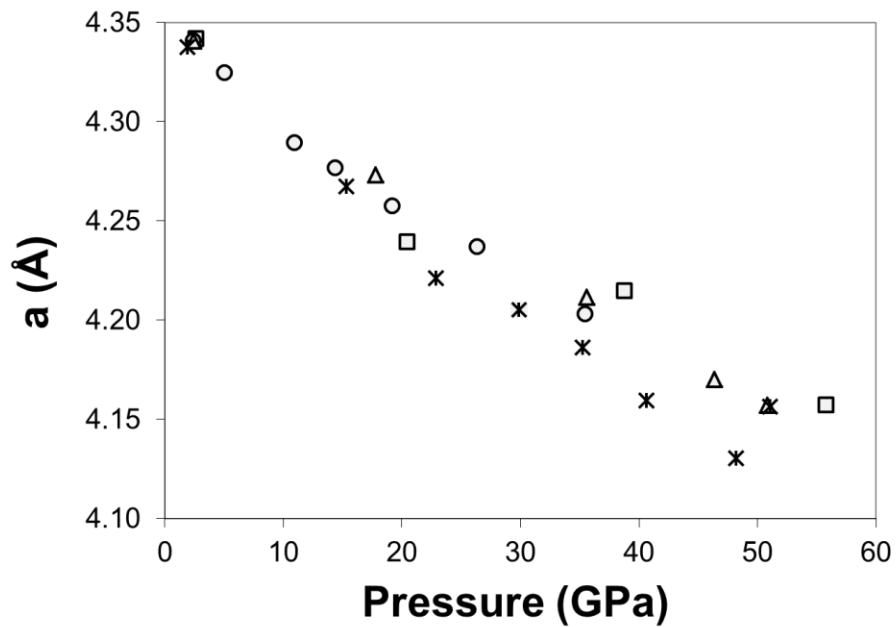


Figure 5.3 Lattice parameter of nanocrystalline SiC samples under pressure: 20 nm grains (squares), 50 nm grains (circles), 130 nm grains (asterisks), and 30 nm nanowires (triangles).

As an initial approach to compression analysis, the total reduction in lattice parameter was observed, and it is seen that smaller grains are compressed less than larger grains, with nanowires behaving very similar to the 50 nm grains (see Table 5.2). Data from the (220) reflection differ by an average of only $6.6 \times 10^{-3} \text{ \AA}$, or 0.20%, from the (111) reflection in 50 nm grains, 130 nm grains, and nanowires.

Table 5.2 Lattice parameter reduction, where Δa is the total change in the lattice parameter and ΔP is the total change in pressure.

Sample	$\Delta a / \Delta P$ ($\text{\AA}/\text{GPa}$)
130 nm Grains	0.00448
50 nm Grains	0.00416
Nanowires (30 nm)	0.00423
20 nm Grains	0.0064

Following the convention of previously published data, the compression data were calculated in terms of normalized volumes.^[108, 109, 114] Linear regressions were performed, and the results are displayed in Fig. 5.4. The compressions of the 50 nm and 130 nm commercial samples agree with available literature pertaining to bulk SiC.^[106] For example, Yoshida et al. report the volume of bulk SiC to be approximately 94% at 20 GPa compared to 93.9% calculated via the linear fit obtained in this work (50 nm and 130 nm crystals).^[115] On the other hand, this work shows that the volume of the 20 nm sample was 20% greater at 20 GPa than that of the larger nanocrystals and bulk material. One may conclude that this is due to a size effect in particles on the order of 20 nm. The compression rate of SiC nanowires is 13% less than that of the 50 nm and 130 nm

particles. This may be an intermediate size effect between bulk SiC and 20 nm grains, or it may be due to the unique, one-dimensional morphology.

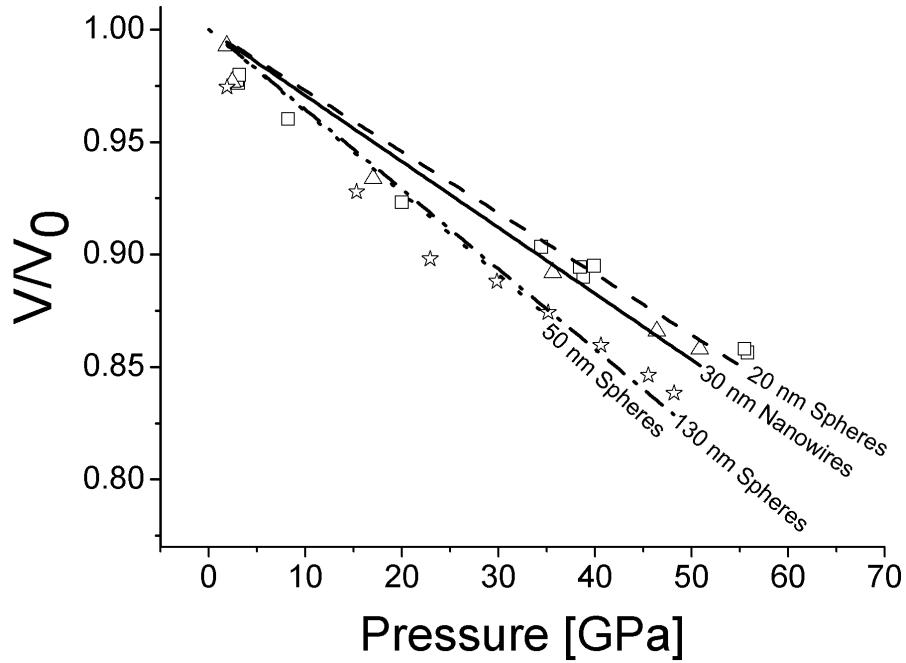


Figure 5.4 Relative volume of SiC as a function of pressure for 20 nm grains (squares), 30 nm diameter nanowires (triangles), and 130 nm grains (stars). The data collected from 50 nm grains have been omitted for clarity. The lines represent linear regressions fitted to the data obtained for the grains (dashed line), nanowires (solid line), 50 nm grains (dotted line), and 130 nm grains (dash-dot line).

A more sophisticated analysis of compression involves determining the equation of state for the material. In this case, as well as most isothermal pressure studies, the Birch-Murnaghan equation of state was used.^[108, 109, 114, 116, 117]

$$P = \frac{3}{2} K \left[\left(\frac{V}{V_0} \right)^{-\frac{7}{3}} - \left(\frac{V}{V_0} \right)^{-\frac{5}{3}} \right] \left\{ 1 + \frac{3}{4} (K' - 4) \left[\left(\frac{V}{V_0} \right)^{-\frac{2}{3}} - 1 \right] \right\} \quad (5-1)$$

V/V_0 is the reduced volume, P is the applied pressure, and K and K' are the fitting parameters: the bulk modulus and its derivative, respectively. The bulk modulus, K , expresses the amount of pressure required to compress a material by a specified unit of volume. Initially, we considered K' an independent variable but the improvements in the fitting routine, judged by the χ^2 , values were insignificant. Following previous calculations, we assumed that $K' = 4$.^[116]

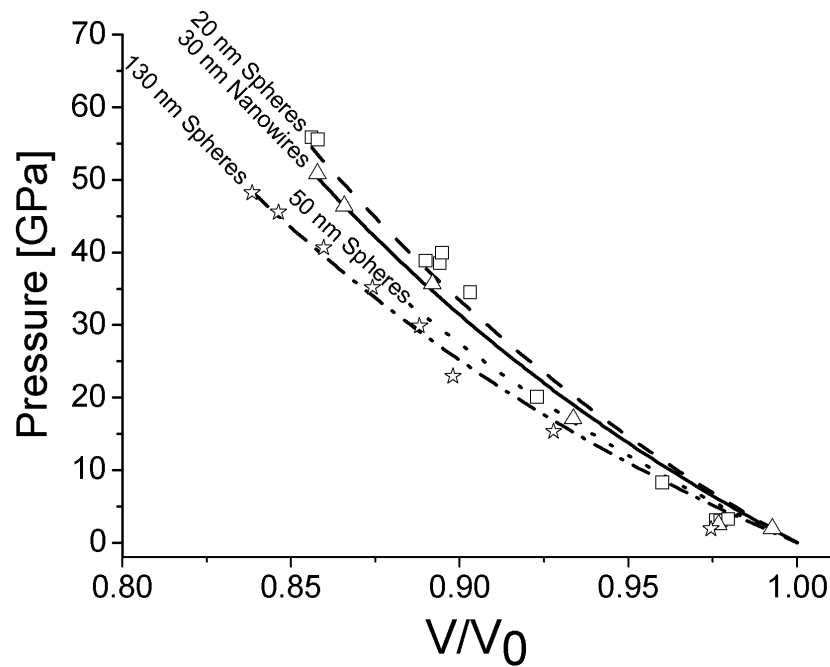


Figure 5.5 Experimental data points for 20 nm grains (squares), 30 nm diameter nanowires (triangles), and 130 nm grains (stars). The data collected from 50 nm grains has been omitted for clarity. The dashed line represents the best fitting of Equation (5-1) to the data obtained for the grains (dashed line), nanowires (solid line), 50 nm grains (dotted line), and 130 nm grains (dash-dot line).

The results of the fitting in Figure 5.5 are shown in Table 5.3. Once again, the data for 50 nm and 130 nm samples coincide with the bulk data in literature. The 20 nm

sample has an elevated bulk modulus, while the bulk modulus of nanowires falls in between that of 20 nm and 50/130 nm grains. Such is expected since the nanowires averaged 30 nm in diameter.

Table 5.3 Measured Bulk Moduli of SiC nanoparticles.

Morphology	K (GPa)
Bulk SiC ^[106]	203 ± 3%
130 nm grains	193 ± 3%
50 nm grains	198 ± 6%
Nanowires (30 nm)	241 ± 7%
20 nm grains	260 ± 15%

Due to the difficulty of experiments with a beveled-culet, this DAC was only used at pressures above 55 GPa. Only one experimental run was successful before a liquid helium leak developed in the wiggler, and experiments on all three connected beamlines were canceled. However, this one run was very important, because it showed that silicon carbide nanowires remain in the cubic state at pressures up to 76 GPa. Also, the unit cell volume at 76 GPa was plotted alongside the data from previous measurements collected under very different experimental conditions: a different pressure medium and a different pressure calibration were used, refer to Section 3.1 for details. When the Birch-Murnaghan equation of state was fitted, the additional 76 GPa data point changed the bulk modulus by less than 2%. The bulk moduli reported for SiC vary wildly in the literature, most probably due to the many combinations of conditions used in DAC

experiments. Now with this work, two experiments have verified each other to an amazingly precise level.

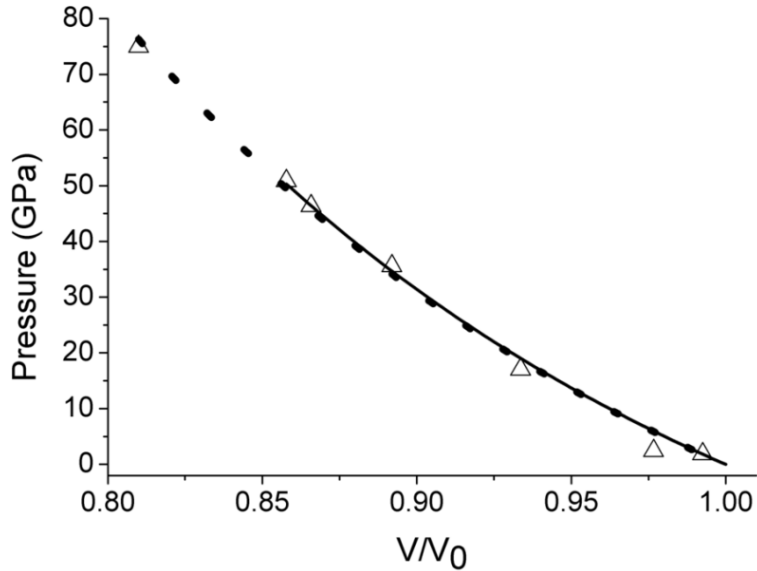


Figure 5.6 The fitting of the Birch-Murnaghan equation to data from SiC nanowires 30 nm in diameter. The solid line shows the fitting done on data collected from the flat-culet DAC, i.e. at pressures less than 50 GPa. The dashed line shows the fitting when the additional datum from the beveled-culet DAC was included.

5.3 Discussion

The elevated bulk modulus is explained by two separate phenomena: the size effect, and the enhancement of hardness due to defects. The size effect will be discussed in this chapter as the well-accepted core-shell model of nanoparticles is applied to SiC nanowires. More will be learned about the contribution to hardening from defects in Chapter VI. Finally, a possible route to tune the hardness is discussed in Chapter VII, as SiC nanowires are modified to control defects.

Surface atoms have different surroundings than atoms in the crystal interior. Contrary to the atoms in the bulk, surface atoms have asymmetrical interactions which, of course, affect their structure. In large crystals the fraction of atoms near the surface is low in comparison with the total number of atoms constituting the crystal. In nanosize crystals this situation is different, and a considerable portion of atoms lie near the surface. For example, in a 5 nm crystal, about 50% of the atoms form a surface layer about 1 nm thick. This effect explains the novel mechanical and chemical properties of nanomaterials. In order to make predictions about such properties, models must be developed treating the surface layer, or “shell” as a separate phase from the interior, the so called “core.”

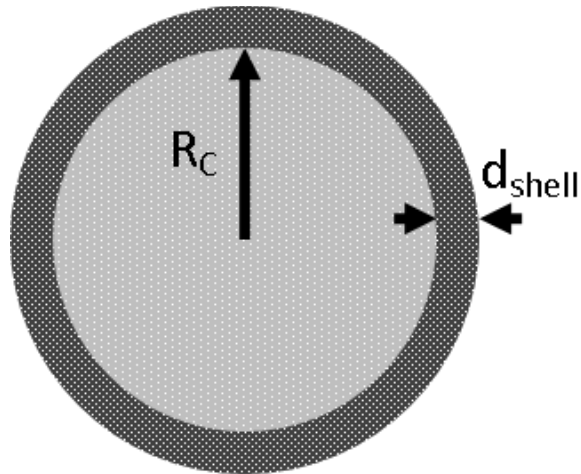


Figure 5.7 Two-dimensional schematic model of a spherical nanograin. The atoms in the surface shell of thickness d_{shell} are compressed relative to the core of radius R_c .

The core-shell model of nanosize particles and wires has been introduced by Palosz and coworkers and has gained general acceptance.^[118-122] Figure 5.7 depicts a core-shell model of a spherical crystal. The core of radius R_c and the shell of thickness d_{shell} have the same crystallographic structure, and the lattice parameter of the core is

indistinguishable from the infinite crystal lattice parameter, a_0 . However, the lattice parameter in the shell differs slightly. In comparison with the core, the shell structure may be expanded or compressed, and its thickness may vary from 0.3 to 0.6 nm for different crystals. Reality is probably more complex, and the lattice parameter changes continuously along the grain radius.

One of the main successes of that model is the explanation of modifications to x-ray diffraction patterns with decreasing particle sizes. Conventional powder diffraction techniques have been developed for materials with perfect 3-D periodic order in an infinite lattice. In such a case, each Bragg reflection will produce an identical lattice parameter. But a long range order in nanocrystals is limited by the size of the grain. Therefore, application of the methods derived for an infinite lattice is inadequate, because the size of the crystallites may be smaller than the coherence length of the incident x-ray beam. In this case, the *alp* method is employed.

Before describing the *alp* method, we must first introduce the effect of the diffraction angle on the depth of penetration into the crystal. This is illustrated in Figure 5.8, where one x-ray is incident upon an atom in the first atomic plane at point a. A second x-ray is incident upon the crystal at an identical angle, but its slight displacement results in penetration to the second atomic plane at point b. If displacement were doubled, it would be incident upon the first atomic plane again. Now consider the three x-rays incident upon the crystal by a much larger angle. The first ray is incident upon the first atomic plane at point c, while a slight displacement causes the second ray at the same angle to interact with an atom at point d, nine atomic planes into the crystal. A different displacement will make a third ray incident at point e, only one atomic plane

deep again. Therefore, lattice parameters calculated from large- Q reflections will reflect interatomic distances measured at statistically larger depths. It must be noted that the strength of the correlation between penetration depth and diffraction angle is dependent on many factors, the most important of which are the symmetry of the atom and the cross-section of interaction between the x-rays and the atoms, the latter of which depends largely on the atomic number.

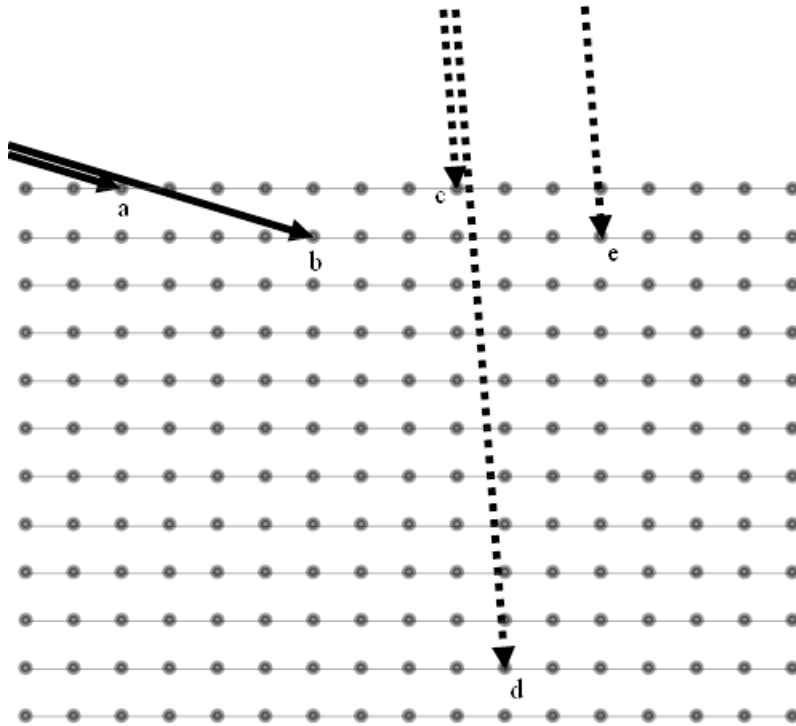


Figure 5.8 Two x-rays incident at an identical low angle are represented by solid lines. A slight relative displacement causes the second ray to travel one atomic layer deeper into the crystal. Three x-rays incident at an identical large angle are represented by broken lines. Depending on the displacement of the second and third large-angle rays, the penetration can be very deep into the crystal.

In a perfect, infinitely large crystal, the region in which atoms are under the influence of asymmetric forces at the surface of is very small in relation to the coherence length of the x-rays. Therefore the diffraction is unaffected and the lattice parameter is universally determined by Equation (2-8). In the case of powder diffraction performed on nanocrystals, however, one ray will encounter many separate crystals whose planes all contribute to the diffractogram. If each crystal contains an outer region of different lattice spacing, as the core-shell model proposes, the contribution of this region will become larger as crystallite sizes become smaller, and Equation (2-8) will no longer apply. Instead, each reflection, uniquely defined by diffraction vector Q , may provide a distinct lattice parameter, referred to as the *apparent lattice parameter*, or *alp*. The diffraction vector is defined as

$$Q = \frac{4 \pi \sin(\theta)}{\lambda} \quad (5-2)$$

For comparison with other diffraction data reported in this work, Q is proportional to scattering angle θ , and data plotted in terms of Q do not depend on the wavelength of x-rays used.

Because of the differences in penetration depth, the shell atoms have the largest effect on the low- Q reflections. The high- Q x-rays, on the other hand, exhibit diffraction from much deeper planes and result in lattice parameters that approach the lattice parameter of the infinite, perfect crystal. It may be noted that the contribution from the compressed region, though dependent in intensity on Q , is always present and thus makes observation of a perfect lattice parameter impossible in any real crystal.

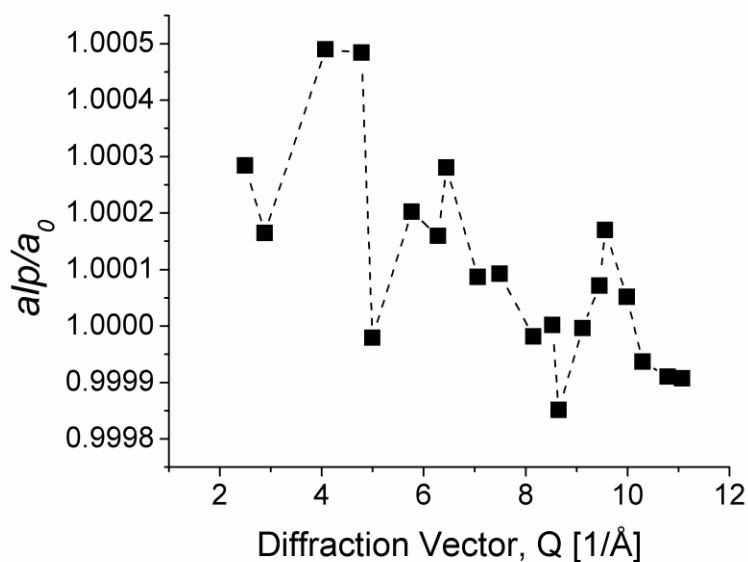


Figure 5.9 The alp - Q plot for 30 nm SiC nanowires. The a/a_0 values were calculated assuming a_0 of the perfect cubic structure was 4.356 Å. The broken line is shown to guide the eye.

In Figure 5.9, we plot lattice parameters calculated from different reflections for SiC nanowires with an average diameter of 30 nm. A standard x-ray diffractometer equipped with a Cu lamp does not allow for observation of small changes in the structure of nanoscale crystals. Typically the Q range for this source is about 6 Å⁻¹, but the Q range required for a meaningful alp - Q plot is at least 12 Å⁻¹. Data in Figure 5.9 were obtained on a custom-made x-ray diffractometer equipped with a silver lamp producing x-rays of 0.55942 Å wavelength. As can be seen, the analysis of these data is not straightforward and requires simultaneous analysis of pair distribution functions from neutron diffraction experiments, computer modeling of diffraction patterns, and, ideally, a Q range up to 25 Å⁻¹.

Such analysis was performed by Palosz et al.^[123-124] for spherical SiC powders, 11 nm and 40 nm in diameter. Reasonably good agreement between experimental and theoretical data was obtained when the structure of silicon carbide nanograins was approximated by the core-shell model with a shell about 0.5 nm thick. In that shell, interatomic distances are about 3% smaller than those in the core.

When the *alp* method is applied to materials with simple atomic arrangements such as aluminum and sodium chloride, the shell is clearly observed by the monotonic change in *alp* with *Q* that quickly levels off to a constant value. However, analysis of the *alp-Q* plot of silicon carbide nanowires in Figure 5.9 indicates that the simple model composed of a single shell and a uniform core is just a first approximation. To better explain the microstructure of silicon carbide, a more sophisticated model is needed. Indeed, Palosz et al.^[124] have pointed out that a more realistic model consisting of a modulated multi-shell structure is needed to explain details of the *alp-Q* plot for spherical SiC. In addition, SiC nanowires possess a shallow layer of amorphous material on their surfaces, which will be discussed in detail in Section 7.2. To account for the amorphous layer, we introduce a model, based on the core-shell model and consisting of the overall radius *R*, crystalline core of radius R_c , and the shell of thickness d_{shell} , which likely contains subshells of changing *alp*, see Figure 5.10. The shell, which consists of crystalline SiC, must not be confused with the amorphous layer of thickness, *d*.

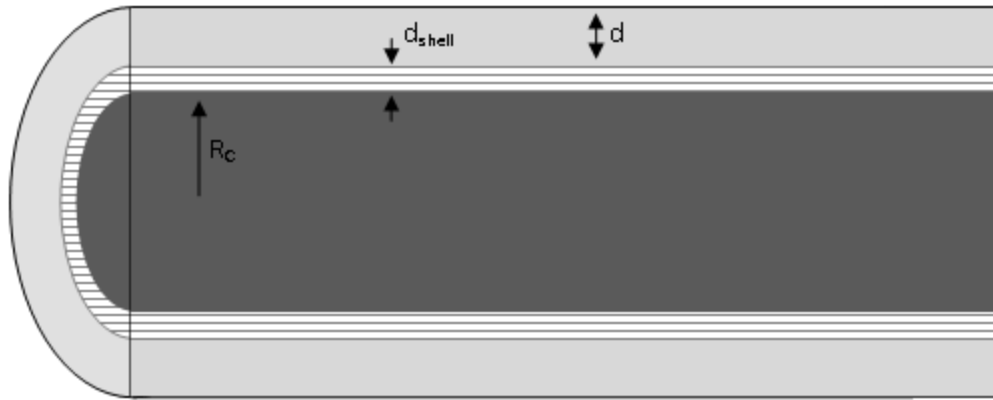


Figure 5.10 A model of a SiC nanowire. The core of radius R_c is surrounded by a shell of the same crystallographic structure but different lattice constant of thickness, d_{shell} . The outer layer of thickness d is the amorphous layer.

The elevated bulk modulus of 20 nm grains and 30 nm wires is explained by the core-shell model.^[118-122] In the core, the majority of the Si and C atoms are arranged in a manner consistent with bulk SiC and they exhibit all the properties associated with the bulk material, such as bulk modulus and lattice parameter. The shell atoms, on the other hand, possess interatomic distances smaller than those of the core. Since the shell is pre-compressed, they resist further compression and shield the core atoms from the hydrostatic pressure.

CHAPTER 6: DEFECTS

6.1 Motivation

Defects may be separated into zero- up to three-dimensional groups. The intrinsic point defects due to missing atoms, the displacement of atoms out of the crystal lattice, and impurity atoms may be included into the zero-dimensional defects, and will not be discussed in further detail here. The one-dimensional defects are dislocations, which will be discussed more in Chapter 7, and the two-dimensional defects include stacking faults, grain boundaries, twins, and domain walls. This section will concentrate on two types of planar faults: twins and stacking faults. Since SiC exists in the form of many different polytypes, these planar imperfections may be incorrectly identified as the inclusion of an alpha phase inside the pure 3C structure.

The importance of defects may be illustrated by summarizing recent connections made between defects and electronic or mechanical properties. Bulk SiC is a brittle material, and easily breaks under small strains, even less than 0.2%. Defects have been shown to strongly affect mechanical properties, especially fracture toughness, by limiting the range and motions of dislocations. According to Zhang et al.,^[125] defects contribute to the remarkable ability of a SiC nanowire to stretch to 200% of its original length. This indicates that SiC nanowires have mechanical properties dramatically different from those of the bulk material, and that defects play a role in this. Stacking faults appear to play an important role during elastic deformations while dislocations are important during plastic deformations.^[126-128] Recently, several groups have theoretically predicted the existence of multi-quantum well systems consisting of cubic SiC wells with hexagonal SiC barriers which may take the form of planar faults.^[129-133] SiC wires with

periodic twins have recently been obtained,^[133] and such periodic structures were shown to exhibit a bandgap modulation, rather than an average value of the potential energy.^[134] Especially relevant to this research is the study by Lin et al. which has recently shown that heavily-twinned SiC nanowires exhibit a bulk modulus 20-40% higher than other morphologies, including nanowires with a lower abundance of twin defects.^[107] This finding was reinforced by molecular dynamics simulations of twinned metal nanowires^[135] and twinned SiC nanowires.^[107] Because of this direct correlation between twins and strengthening, this paper will focus most of its attention on planar defects, and they will be identified by direct TEM imaging, TEM electron diffraction, and x-ray diffraction profile analysis.

All SiC nanowires possess large quantities of planar defects, among which twins and stacking faults appear to be most abundant. Both planar defects were identified in TEM images, Raman spectra and x-ray diffraction images.^[137, 138] However, distinguishing stacking faults from twins in TEM images is not a simple task. Besides, such analyses would not allow for quantitative evaluation of the defects. Fortunately simultaneous analyses of multiple lines in x-ray diffraction allow filling of that gap. As discussed in the section on x-ray profile analysis, this methodology allows the determination of crystallite sizes and the population of dislocations and twins. Once quantitative knowledge of crystal defects is obtained, it is possible to estimate the effect these defects have on the elastic properties. The logical next step is to gain control of these defects, and thus tune the physical properties to a particular need.

6.2 TEM Analysis

A twin defect is a special form of grain boundary which is isolated to a single plane, and we may describe a twin defect as a crystal structure reflection across a mirror plane. This arrangement allows the atomic layers to satisfy all their bonds, but the symmetry of the cubic crystal is disrupted. For example, the regular stacking sequence “ABCABCABC” may form a twin to become “ABCA/CBAC.” The formation of this defect occurs usually during crystal growth, thermal annealing, application of mechanical shear forces, or other deformations of the material. However, they may also form spontaneously under very well-controlled conditions, because the energy of twin formation is so low. Twins are commonly found in spherical nanoparticles and in nanowires, and the fcc metallic nanocrystals usually have (111) twins.^[139] Recent studies have shown that this form of defect is very common in nanowires of material having the zinc-blend form, such as SiC, when they are grown by the VLS method.^[140-145]

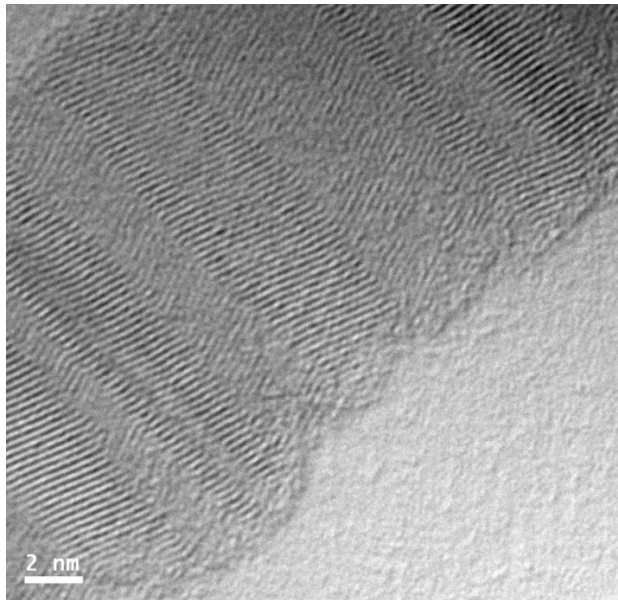


Figure 6.1 Direct-space image of twins in a SiC nanowire obtained by TEM. The angle formed at the twin boundary is 141° . Image presented courtesy of M. Wieligor.

The TEM image shown in Figure 6.1 very clearly shows repeated twins in the structure of one particular SiC nanowire. The visible lattice lines are separated by 2.52 Å, which corresponds to the interatomic spacing of the (111) planes and indicates that the growth direction is along the (111) axis. The angle formed by the intersecting (111) planes along the twin axis is 141°, which is characteristic for an fcc structure.^[146] In this atomic arrangement, the 141° angle is energetically favorable and twins with angles below 40° become unstable. As a result the 141° twins are the most common and are known as first-order twins or lowest-order twins. Understandably, only first order twins were observed in SiC nanowires produced by the method described in this paper.

While Figure 6.1 shows twins clearly, most of the SiC nanowires do not have such large regions between twin boundaries, making them much more difficult to spot. In most cases, twins are identified by electron diffraction, and, in Figure 6.2, nanobeam diffraction with the 15 nm incident beam was employed to obtain the diffraction pattern within two distinct twin segments, denoted as a) and b) in the figure. We see that, if the image in a) is rotated by 141°, the diffraction image would match that in b). Nanobeam diffraction is more difficult and time consuming than selected-area diffraction, so usually diffraction images are produced from multiple segments at the same time, which is seen in c). This is simply the overlap of images a) and b), and by the extra set of diffraction spots, one may identify a twin defect.

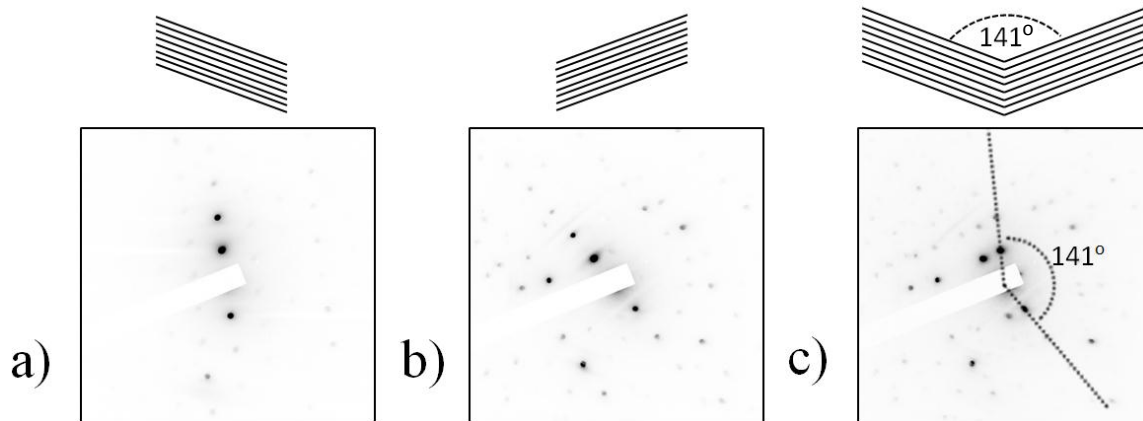


Figure 6.2 Construction of the electron diffraction pattern produced by twin defects. Here the beam size was 15 nm and the inverse of the diffraction images are shown for clarity. a) and b) are the diffraction patterns collected from two distinct regions of a SiC nanowire. c) depicts the diffraction image collected from the boundary where the electron beam is incident upon both regions. Above each diffraction image is a schematic of the atomic planes from which the diffraction originated.

The other defect brought to attention in this section is the stacking fault. A stacking fault is a disturbance or discontinuity in the normal stacking sequence. For example, the “ABCABCABC” sequence may change to “ABCA/CABC”. Because the range of a stacking fault can only be one plane in an fcc structure, they are even more difficult to observe by direct TEM imaging than twins. They are most often spotted when 1) they are concentrated to a particular area of a nanowire, or 2) the electron beam is incident on the nanowire at an angle other than perpendicular to the nanowire growth axis. If the latter case is true, a disc of higher contrast is seen along the growth axis of the nanowire. Otherwise, only a very thin line, 2.52 Å wide is seen in the nanowire. In either case, very short order twins can easily be misidentified as stacking faults, and only

electron diffraction can definitively differentiate the two. Stacking faults are identified in diffraction images as streaks running tangentially to the Ewald sphere. The direct TEM image of a nanowire with stacking faults is shown in Figure 6.3 with its Fourier transform beside it showing streaks due to stacking faults. The Fourier transform produces an image of reciprocal space just as diffraction does.

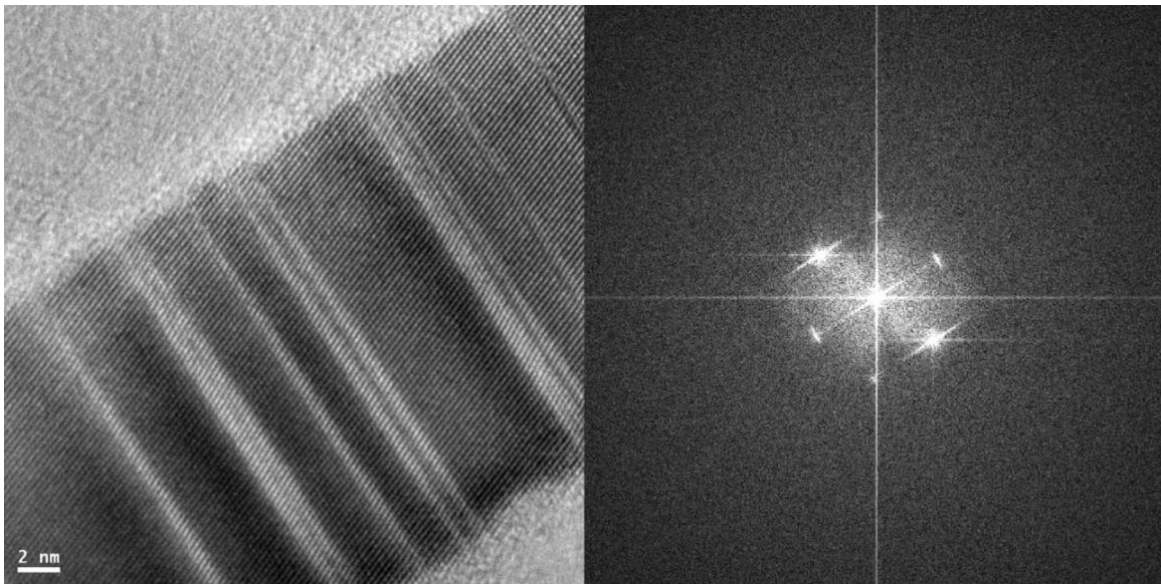


Figure 6.3 Left: a TEM image of stacking faults in a SiC nanowire. Right: A Fast Fourier transform of the image on the left. Notice the streaking that results from stacking faults.

Stacking fault formation energy is higher than that of twins. For example, in the case of III-V semiconductors, the energy to form a stacking fault is approximately twice the twin formation energy.^[140] Consequently, their populations appear to be smaller than those of twins. This formation energy is still very small and corresponds to the kinetic energy at room temperature, so it is not surprising that nanowires manufactured at about

1200°C have abundant stacking faults and twins. These defects are always present in SiC nanowires, regardless of the manufacturing technique and precursors used.

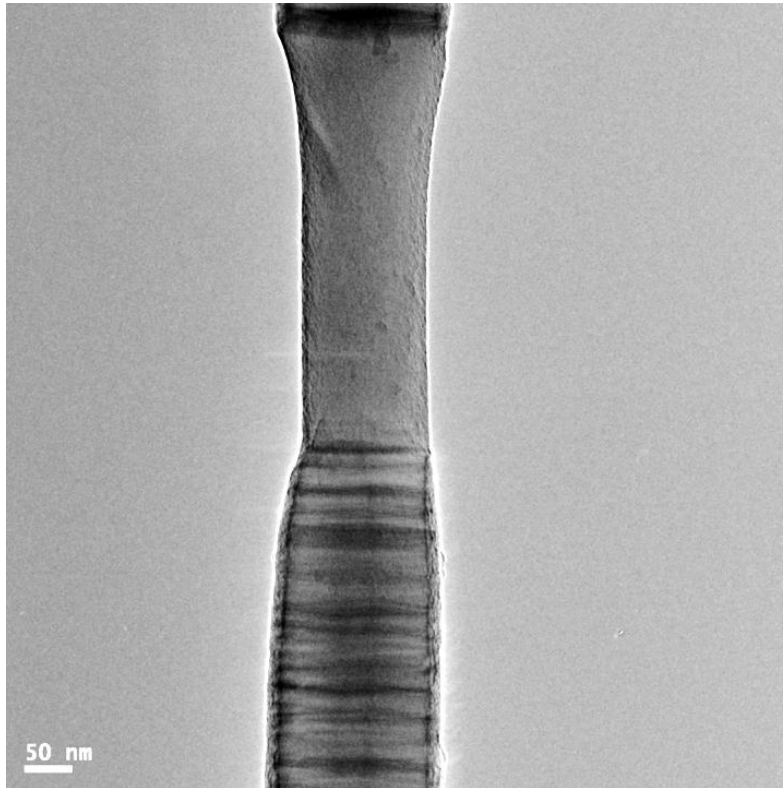


Figure 6.4 A SiC nanowire exhibiting a section with numerous planar faults and a defect-free section.

Numerous sections of wires were free of planar defects, as in Figure 6.4. The causes for the presence of planar defects in some wires and its absence in the others or the formation of defect free zones within a nanowire are still unknown. Wang et al.^[148] interpreted the formation of stacking faults in nanowires in terms of surface energy. This approach is typical for theories attempting to explain the existence of stacking faults and twin boundaries as low energy structures that readily form to relieve strain.^[148-149] In the

cubic structure, the (111) direction is energetically privileged, and the (111) planes of SiC are known to have lower surface energy than other (*hkl*) planes.^[150] Cubic SiC has an interesting feature: it possesses two interpenetrating face-centered sublattices. One lattice is formed by silicon atoms; the second one belongs entirely to carbon atoms. These lattices are separated by the displacement vector ($a/4, a/4, a/4$). Thus, each lattice is occupied by different atoms, and opposite side surfaces (111) have different polarities. This creates the different surface energies, which means that the side with entirely silicon atoms has different energy than the side containing only carbon atoms. These differences at the nanosize scale often become a source of bending and strain in the nanowires, due to the surface tension. In order to reduce the strain created during the nanowire growth, the polarity must be reversed, which is accomplished by the creation of twin structures.^[148]

TEM analysis indicates that densities of stacking faults and twins are dependent on the diameter of the wires and decrease with decreasing diameter. This conclusion is similar to that reached by Zhang et al.,^[153] Niu et al.,^[154] Roy et al.,^[155] Yu et al.,^[156] and Kraft.^[157] Unfortunately, analysis of TEM images does not allow for quantitative analysis of concentrations of either planar defect.^[152]

6.3 XRD Investigation of Microstructure

6.3.1 The Williamson-Hall Plot

Figure 6.5 depicts the Williamson-Hall plot of silicon carbide nanowires and, for comparison purposes, the corresponding data for SiC compacts heated to 1800°C at two different pressures. The SiC phase in compacts has nanosize structure, and the

population of stacking faults and dislocations depends on the applied pressure.^[158, 159] At high pressure, 5.5 GPa, the population of dislocations is orders of magnitude higher than in the compacts sintered at a relatively low pressure of 2 GPa. Nauyoks et al.^[159] also showed that the population of stacking faults at 2.0 GPa is much higher than in the sample obtained at 5.5 GPa. The Williamson-Hall plot for the nanowires follows the same trend as the 2.0 GPa sample, just with proportionally reduced FWHM due to different average crystallite size. It is an indication that the stacking faults play an important role in SiC nanowires, and the effect of dislocations on the line width of the nanowires is small.

Although further developments in the Williamson-Hall technique were made,^[160] they will not be discussed here and instead we will focus on a recently developed method of simultaneous analysis of diffraction peaks.

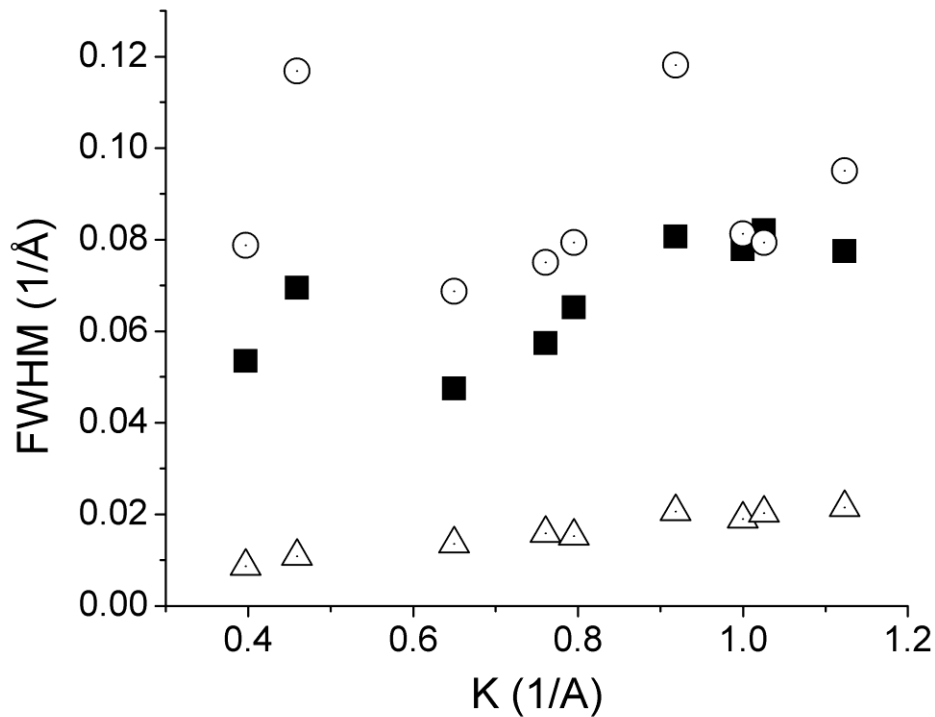


Figure 6.5 The Williamson-Hall plots for SiC nanowires of average diameter 30 nm, (solid squares) and SiC compacts (open symbols). Circles represent data for compacts obtained at 2 GPa and triangles for compacts sintered at 5.5 GPa. Data on SiC compacts originated from S. Nauyoks dissertation.^[158]

6.3.2 Application of the eCMWP Method

A typical diffraction pattern of SiC nanowires is shown in Figure 6.6. A shoulder is observed near the (111) peak at 33.6° , with x-ray wavelength 1.54 \AA , as seen in the insert in Figure 6.6. This shoulder has been attributed to planar faults. Therefore the eCMWP method was applied to obtain meaningful information regarding microstructure.

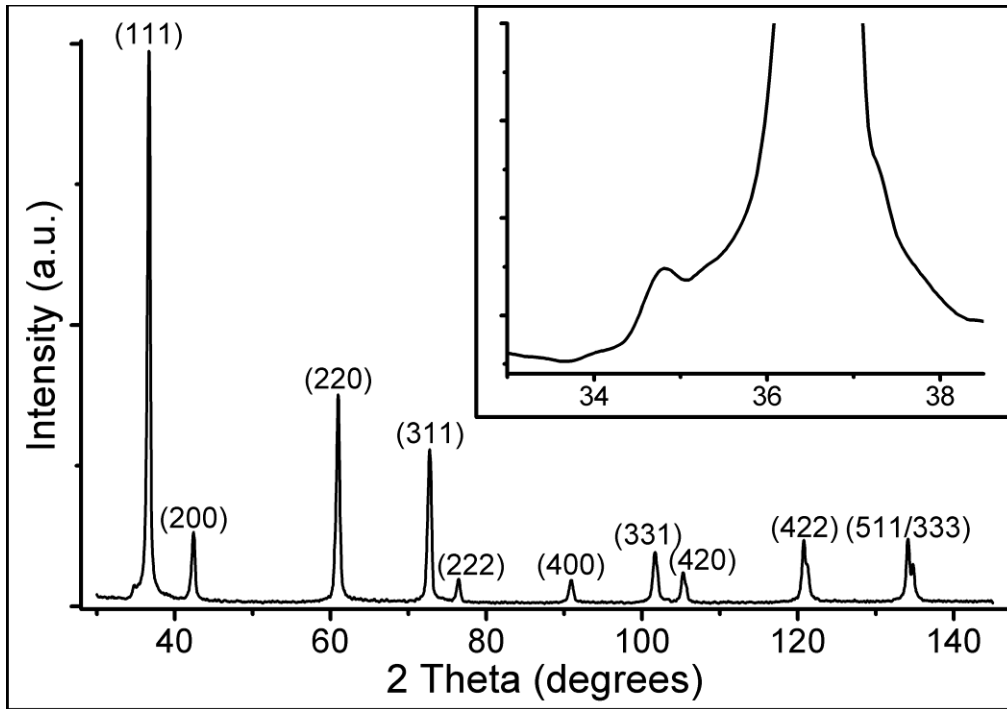


Figure 6.6 The X-Ray diffraction pattern for SiC nanowires of average diameter 30 nm. Reflections are assigned to different crystallographic planes. The insert shows details of the (111) peak with the shoulder due to stacking faults.

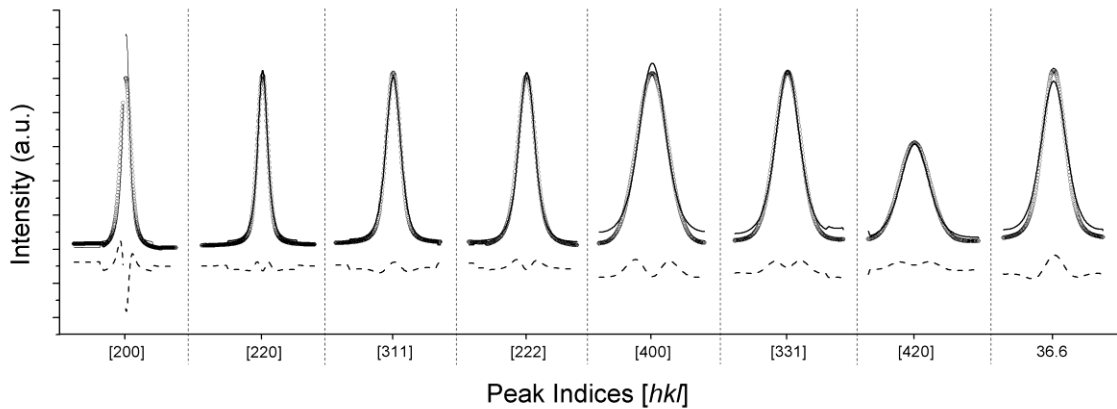


Figure 6.7 Example of the fitting procedure. Measured data (open circles) and fitted diffraction profile (solid line) for the 30 nm diameter SiC nanowires. The difference between the two sets of data is shown at the bottom part of the figure.

As explained previously, TEM imaging leads one to believe that twins are the most prevalent form of planar faults present in the SiC nanowires. Thus the eCMWP procedure was performed with this assumption in place, and the quality of the fitting procedure is shown in Figure 6.7. When either extrinsic or intrinsic stacking faults were initially assumed in the eCMWP fitting process, the sum of the residuals was orders of magnitude larger, thus confirming the assumption regarding twins. The results of the x-ray profile analysis are summarized in Table 6.1. The probability of twin defects was determined to be 2.2%, or in other words, there should be a twin about every 50 planes in the stacking sequence. SiC is known to grow along the $\{111\}$ direction, which is confirmed by TEM in our SiC nanowires. Assuming a one-dimensional wire, the distance between the (111) planes of SiC is 0.755 nm, thus the distance between twins should be 37.8 nm. This back of the envelope calculation did not take into account that there are actually four equivalent $\{111\}$ directions, and an average separation distance between two twins is expected to be less. TEM shows that, when twins are present, their separation is, indeed, much less than 37.8 nm.

The eCMWP analysis shows the average area weighted crystallite size is 31 nm. This value is very similar to the mean value produced by the lognormal distribution of diameters directly measured from TEM. This result indicates that the nanowires must contain subgrains of lengths comparable to the diameter of the nanowires themselves. If this were not the case, nanowires oriented perpendicularly to the incident x-rays would have provided a larger coherence length, and thus a larger grain size in the eCMWP analysis. It can be inferred that the grain boundaries take the form of twin defects, which

effectively shortened the coherence length seen by an x-ray normal to the surface of such a planar defect.

Table 6.1 The calculated parameters of the microstructure of silicon carbide in different forms: SiC nanowires, SiC phase in a diamond/silicon carbide composite sintered at 8.0 GPa and 1820°C, and a SiC compact sintered from nanosize powder at 5.5 GPa and 1800°C. $\langle x \rangle_{area}$ is the area-weighted mean crystallite size, β is the planar fault probability, and ρ is the dislocation density.

	SiC nanowire	SiC phase in diamond/SiC composite ^[158]	SiC compact ^[158]
$\langle x \rangle_{area}$	31 nm	20 nm	126 nm
β	2.20%	2.60%	0.17%
ρ	$6.8 \times 10^{15} \text{ m}^{-2}$	$4.3 \times 10^{15} \text{ m}^{-2}$	$0.4 \times 10^{15} \text{ m}^{-2}$

Typically, increased pressure and temperature cause growth of populations of planar faults and dislocations in ceramic materials, such as diamond or silicon carbide.^[159, 161-163] Often this process is accompanied by increased crystallite sizes. In Table 6.1, we compare results obtained from the CMWP analysis for nanosize silicon carbide in three different materials. Diamond-silicon carbide composites were sintered from a mixture of nanosize diamond and silicon powders at high pressures and temperatures. Details of the sintering protocol can be found in the References section.^[159, 161-163] Silicon carbide compacts were obtained from nanocrystalline SiC powder of nominal grain size, 30 nm. They were sintered in a high pressure toroid system.^[164] It is

seen that the microstructure of SiC nanowires is similar to the microstructure of SiC in diamond composites, which is a surprising result. In diamond composites, a large population of planar faults and dislocation densities is caused by strain associated with different rates of thermal expansion and the compressibility of diamond and silicon carbide phases. Comparable populations obtained for the nanowires indicate that its structural defects may be associated with stresses of a similar magnitude as those in diamond-SiC composites.

The work already mentioned by Lin and coworkers^[107] showed a link between nanoscale twinning and elastic strengthening in SiC nanowires.^[107] However, they did not report quantitative information regarding the abundance of twins. Upon initial inspection, their SiC nanowires appear to have a much larger abundance of twin defects, and the nanowires themselves are larger, 50-300 nm. Therefore, one may conclude that the contribution of planar defects to the elevated bulk modulus is, indeed, real and not a misunderstanding of the confinement affect.

CHAPTER 7: SURFACE FORMATIONS

7.1 Motivation

In addition to its superb mechanical properties discussed earlier, SiC is a wide bandgap semiconductor that possesses many electrical attributes that make it appealing for modern applications.^[165, 10] Thus recent years have seen growing effort to develop microelectronic devices from SiC for high-temperature, high-power, and high frequency applications.^[166] One-dimensional semiconductor nanomaterials deserve special attention, because they play a crucial role as building blocks of future molecular electronic applications,^[169-171] and attempts to use SiC nanowires for nanoelectronic and optoelectronic device applications have already been reported.^[170, 172-175] However, defects have prevented its widespread use in electronic applications for decades, despite the promising signs of defect-enhanced mechanical properties. If SiC, both in its bulk and its nanowire form, is to see its full potential in electronic applications, control over these defects must be maintained. This work presents a method to reduce or alter the amorphous layer surrounding SiC nanowires and its subsequent effect on defects in the microstructure.

7.2 Atomic Structure of the Amorphous Layer

4.5 Acid Treatments

All nanowires have a crystalline core and are coated with an amorphous layer. The thickness of that layer varies from 1 to 10 nm. Its composition depends on properties of the precursors and the history of post-production treatment. It is well known that

strong acids and bases may etch away silicon and silicon dioxide, so the SiC nanowires were treated in two acids in order to modify the surface. SiC nanowires were exposed to aqueous solutions of 40% hydrofluoric acid (HF) and 70% nitric acid (HNO₃). After 15 minutes, the samples were centrifuged for 15 minutes. After centrifugation, a large portion of acid was drawn off with a pipette and replaced with water. This process was repeated in order to dilute the acid to a safe level without removing small nanowires suspended in the liquid. Afterwards, the samples were dried in an oven at 80°C. Their total exposure time to the full strength acids was 30 min. It must be noted that the nanowires used for high pressure experiments were not treated with acid.

7.2.1 Energy Dispersive Spectroscopy

An important and still unresolved aspect of the structure of the nanowires is the atomic arrangement of the amorphous layer. Is it just amorphous SiC, a carbon rich silicon layer, or maybe a mixture of silicon in a predominantly carbon layer? To answer this question we employed EDS and FTIR. The resolution of the beam used for EDS was limited to about 10 nm, so only relatively large wires with correspondingly large amorphous layers were chosen for analysis. Elemental analysis of the nanowires clearly showed that besides silicon and carbon there was a significant concentration of oxygen, as indicated by the EDS results depicted in Figure 7.1. The sample rested upon a uniform carbon substrate, and it is presumed that the level of adsorbed oxygen would be the same on the substrate as on the wire. In other words, if oxygen was only adsorbed on the surface of the wires and was not part of the composition, there should be no relative increase in oxygen content between the carbon substrate and the SiC nanowire. However, we see from the line-scan in Figure 7.1 that there is indeed a significantly

larger amount of oxygen bonded into the amorphous layer, and that this concentration remains relatively constant across the diameter of the wire. We concluded that oxygen was present only in the outer layer of the amorphous structure, since the SiC lattice structure can be seen in the core of the wire. Although this conclusion is limited to the relatively large nanowires of diameters greater than 100 nm, due to limitations in resolution while using the TEM in scanning mode. We believe that it is also true for nanowires of smaller sizes, more representative of the samples.

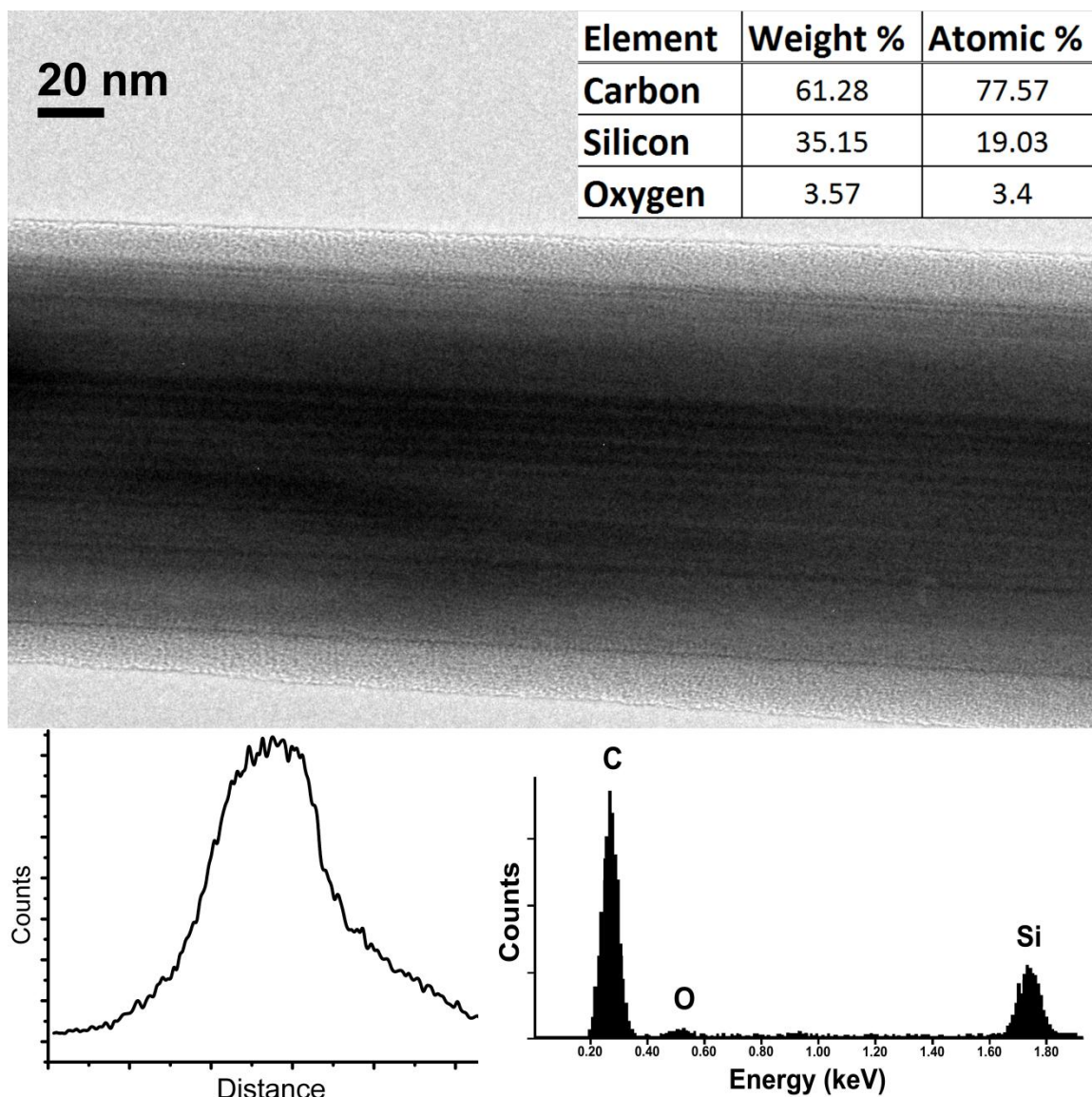


Figure 7.1 TEM image of a silicon carbide nanowire. The EDS spectrum is shown in the bottom right corner and the data are quantified in the top right corner. The data were collected from the entire region shown by the image. In the insert in the left corner, the solid line represents oxygen concentration measured across the nanowire diameter.

7.2.2 Fourier Transform Infrared Spectroscopy

FTIR is well suited for analysis of molecular composition of SiC specimens. In Figure 7.2 a typical spectrum of SiC nanowires collected using KBr pellets is shown.

This specimen was later heat treated in air at 700°C for two hours to remove carbon impurities. The most intense bands in the spectrum are due to two SiC phonons, the longitudinal optical phonon (LO) at 920 cm⁻¹ and the transverse optical phonon (TO) at 822 cm⁻¹. In the high frequency region, the spectrum is dominated by a broad and asymmetric peak due to water at 3460 cm⁻¹. To reduce the water, the samples were heated to 200°C and evacuated while being pressed into a pellet, but the complete removal of water is virtually impossible when making pellets of highly hygroscopic KBr. An identical peak was seen when a pure KBr pellet was measured.

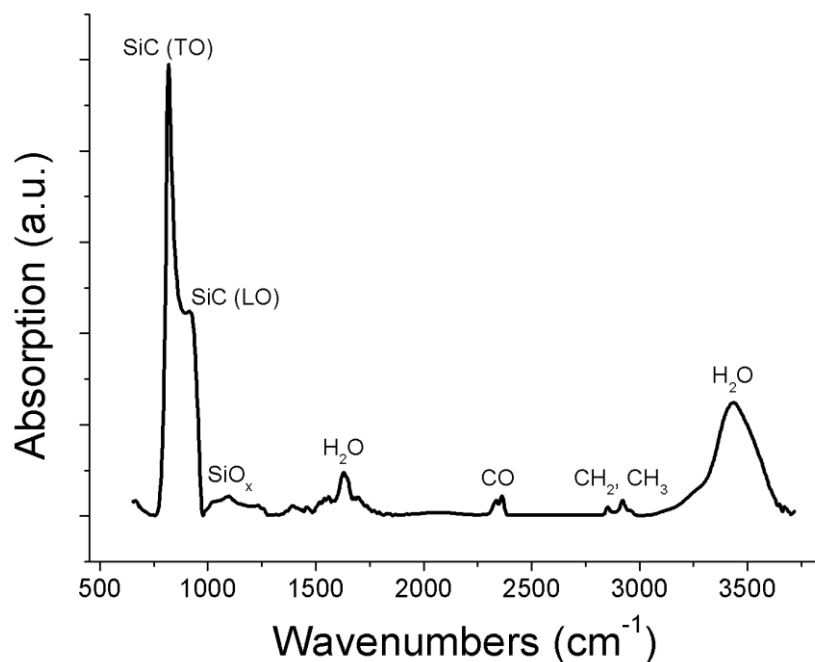


Figure 7.2 FTIR spectrum of SiC nanowires before thermal or acid treatment.

It must be noted that the peak location of the TO and LO bands of silicon carbide are shifted by about 16 cm⁻¹. This is caused by the local interaction between the electromagnetic fields of the SiC nanowires and those of the KBr matrix in which they

are embedded. When the samples are measured again using other sampling techniques, the shift disappears, see Figure 7.3.^[176]

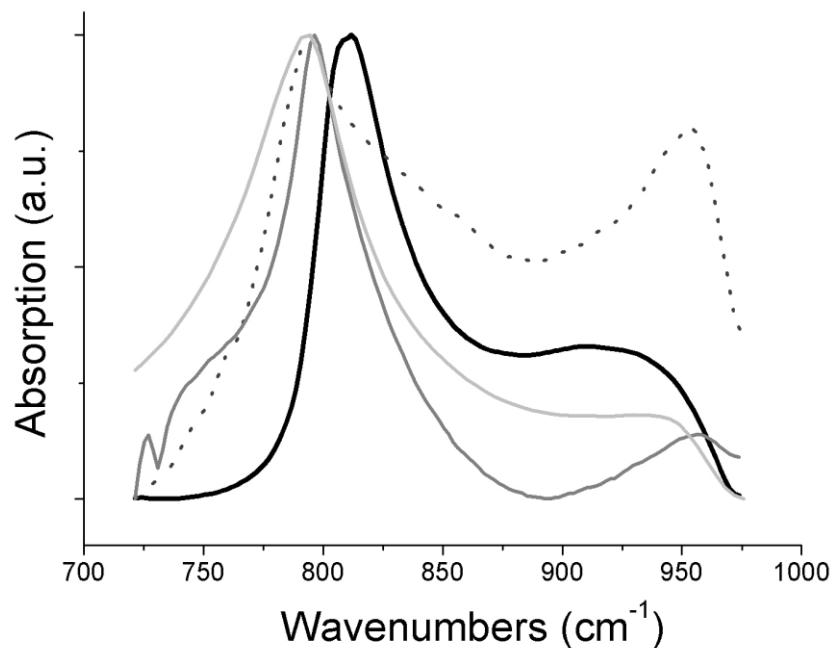


Figure 7.3 FTIR spectra of one sample of SiC nanowires collected by various techniques. The black line is the spectrum collected via conventional transmission, the dark grey is the spectrum from nanowires dispersed in mineral oil between KBr plates, the light grey line is the spectrum collected via diamond ATR, and the dotted line is a spectrum collected with the photoacoustic technique, not discussed in this paper.

The infrared spectra show that various carbon compounds are present in the specimen. The three peaks at 2962, 2922 and 2851 cm^{-1} are assigned to CH_2 and CH_3 stretching vibrations, while a number of small intensity bands in the frequency range from about 1300 cm^{-1} to 1700 cm^{-1} correspond to $-\text{COO}^-$, $-\text{COOH}$, $-\text{CH}_2$, and $\text{C}=\text{C}$ vibrations.^[177, 178] We have not found traces of Si-H bands, but Si-O bands were strong,

indicating that glass-like structures were the main form of silicon containing species present in the specimens next to SiC. These compounds were most likely assembled on the outer layers of the nanowires contributing to the amorphous structure.^[179, 180]

The bending mode O-Si-O at 810 cm⁻¹ partially overlaps with the SiC phonon and is difficult to investigate. Thus we will focus most of our attention on the asymmetric stretching Si-O vibration observed at about 1095 cm⁻¹^[179, 180]. Assuming that the broad peak at 1095 cm⁻¹ is caused by vibrations of structures similar to those present in glass, we ran a series of experiments to calculate the extinction coefficient for glass using the Beer-Lambert law.

$$\ln\left(\frac{I_0}{I}\right) = \epsilon lc \quad (7-1)$$

where I_0 is the intensity of the background, I is the intensity of the peak at 1095 cm⁻¹, ϵ is the extinction coefficient, l is the path length of the radiation through the sample (measured as the thickness of the KBr pellet) and c is the concentration of the glass within the KBr pellet. Pellets were formed with varying concentrations of ground glass in the KBr matrix. The thickness of the pellet was measured and spectra were collected. With the intensity ratio measured and plotted, the extinction coefficient was determined from the slope, see Figure 7.4.

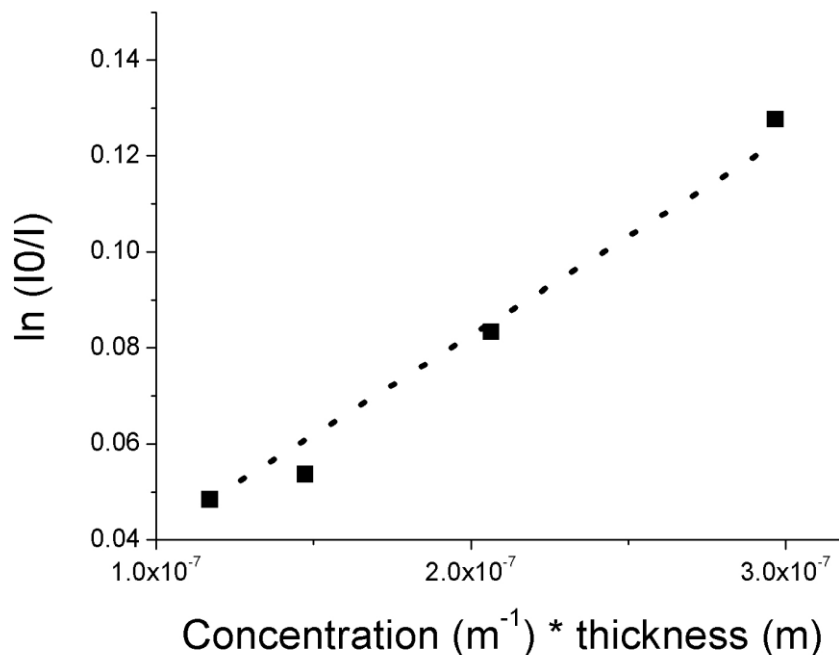


Figure 7.4 Determination of the extinction coefficient of glass. The points were collected from glass-KBr pellets and the intensity was measured from the peak around 1095 cm⁻¹. The dotted line is a linear regression fit to the data points.

With this data, it was possible to estimate the concentration of SiO₂ from that peak intensity. The calculated amount accounted for about 1% of the total mass of a 2 nm thick amorphous layer wrapping around all structures. The uncertainty in our calculations mean that the amount may be as much as 10%, but this is still low enough to conclude that the thin film on the surface of SiC nanowires and particles is mainly amorphous silicon carbide with a small amount of SiO_x and amorphous carbon. The fact that the infrared absorption peak was blue shifted further indicated that it was not pure SiO₂ but an amorphous structure of random chemical stoichiometry. From this brief description of a typical infrared adsorption spectrum, one may conclude that various oxygen containing functional groups coexist with SiC crystalline structure. Since oxygen does not readily

dilute in SiC we further conclude that these species are formed on the outer layers of SiC wire and contribute to the amorphous layer.

7.3 Surface Modification

7.3.1 Thermal Treatment

After synthesis, it was necessary to heat the raw samples at 700°C in oxygen to remove the excess MWCNTs, but this thermal treatment undoubtedly affects the SiC nanowires as well. Thus we must discuss the changes in the absorption spectra induced by thermal treatment. Two peaks centered about 1650 cm⁻¹ and 1700 cm⁻¹ correspond to the –COOH vibration, see Figure 7.5.^[177, 178] The 1650 cm⁻¹ overlaps with the peak from water at 1630 cm⁻¹ but is still observable. These peaks increase with thermal treatment. To explain this effect, we assume that large agglomerations of carbon atoms, probably in the form of graphitic nanosize crystallites, ‘burned out’ leaving carboxyl groups attached to amorphous silicon carbide. It is important to note that the CH₂ and CH₃ peaks near 2900 cm⁻¹ were not removed by the heat treatment. From the unidentified peaks at 1227 cm⁻¹, 1366 cm⁻¹, and 1387 cm⁻¹, we can say that there are most likely other functional groups attached to amorphous silicon carbide.

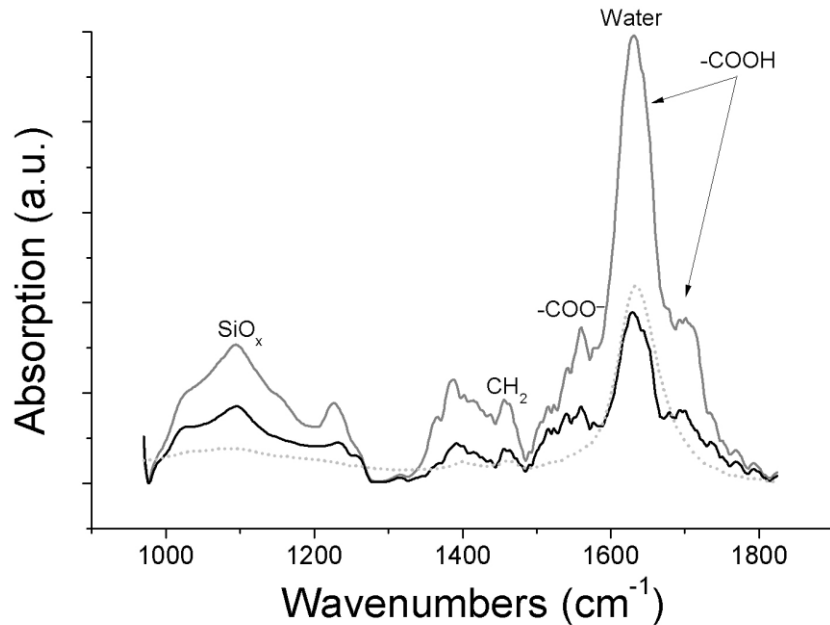


Figure 7.5 Infrared spectrum of SiC nanowires before 700°C thermal treatment (black) and after thermal treatment (grey). Also included is a spectrum collected from pure KBr (dotted line).

Temperature treatment also affected the Si-O bands. After heating the specimen at 700°C, the peak's intensity increased slightly, indicating a higher concentration of silica, see Figure 7.5. The increase in SiO_x during the thermal treatment came about through the dissociation of amorphous SiC and the recombination of Si with O.

7.3.2 Acid Treatment

Etching in an acid or a strong base is a commonly used technique for removal of undesired surface material and preparing specimens for subsequent surface functionalization procedures. EDS Spectroscopy was not useful for studying the effects of such a treatment, because the same nanowire would have to be observed before and after treatment in order to obtain useful data. Otherwise, it would be impossible to tell

whether the surface changed due to the acid, or whether a different nanowire was being observed which had a different surface from synthesis. Therefore FTIR was employed to make a statistical determination of changes due to the acid treatment. In Figure 7.6, we show absorption spectra of the same sample before and after treatment in hydrofluoric and nitric acids (HF and HNO₃, respectively). Silica bands at 1090 cm⁻¹ decreased in intensity, indicating that their concentration dropped. However, a peak centered at about 1460 cm⁻¹ grew dramatically in intensity with treatment by HNO₃. This peak corresponds to -CH₂ bonding and indicates that acid etching promotes formation of functional groups at the surface. The CH₂ and CH₃ groups around 2900 cm⁻¹ also where increased with HNO₃ treatment, see Figure 7.7. This result is in agreement with the conclusion of a study by Gogotsi et al.^[181] on hydrothermal treatment of SiC powders.

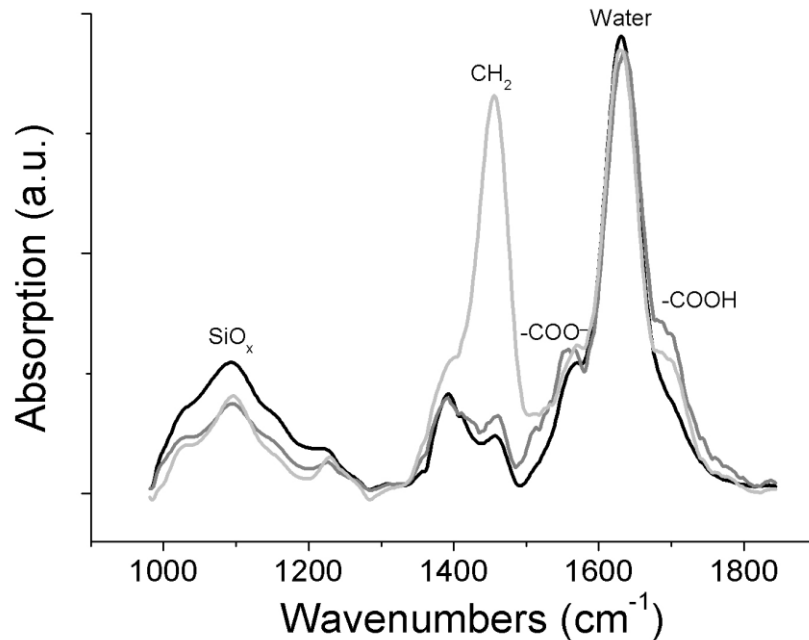


Figure 7.6 Infrared spectrum of SiC nanowires untreated (black line), treated with HF (dark grey line), and treated with HNO₃ (light grey line).

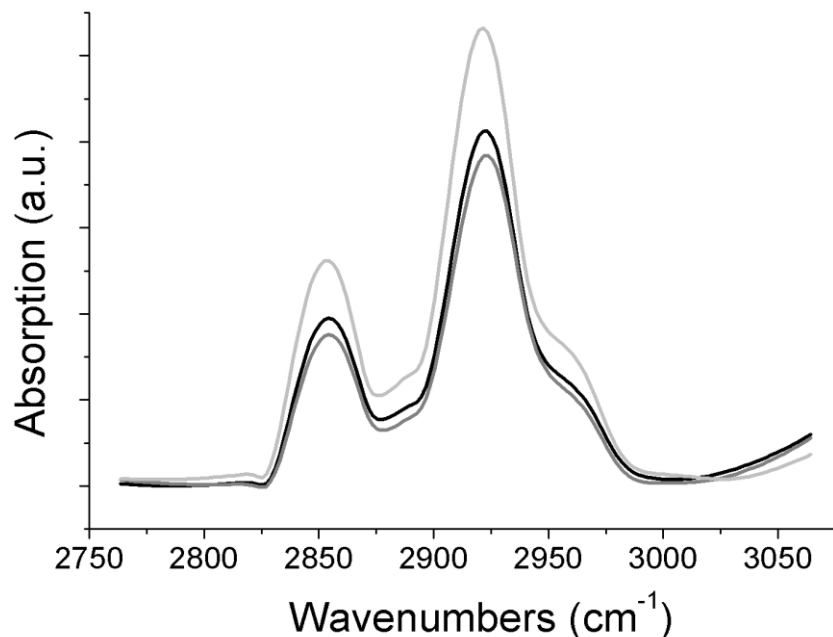


Figure 7.7 Infrared spectrum highlighting CH₂ and CH₃ bands of SiC nanowires untreated (black line), treated with HF (dark grey line), and treated with HNO₃ (light grey line).

When the XRD whole profile fitting analysis was applied to the treated wires, it was seen that the surface modification had effects that extended to the microstructure. The grain size is shown to increase by as much as 186% when treated by nitric acid. One possible explanation for this is that the acids etched away the small wires, leaving only the largest wires to contribute to the diffraction signal. However, this is shown to not be the case. TEM images show the size distribution to be nearly identical before and after acid treatment. A better conclusion is that the coherence length encountered by incident x-rays was lengthened, because the distance between defects was lengthened. In other words, the defects have either migrated, or their abundance has been reduced. TEM is not useful here, because it does not detect most dislocations and because of the

difficulties in obtaining quantitative results, as was mentioned in section 6.1. Therefore dislocations were included in the XRD profile fitting parameters, the results of which are shown in Figure 7.8. As suspected, the analysis shows that dislocations do indeed decrease by as much as 91% after acid treatment. With fewer dislocations and lesser disorientation along the nanowire axis, larger crystallites are recorded. Stacking faults also serve as a boundary to x-ray coherence, but instrumental limitations prevented their study:

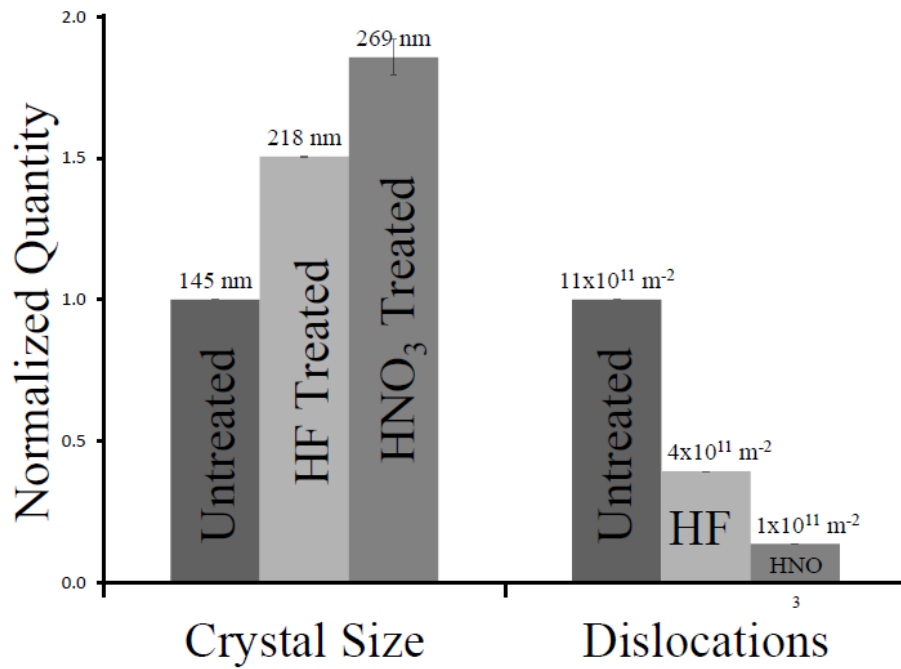


Figure 7.8 The effect of acid treatment on dislocations in SiC Nanowires. Note that, for comparison, all data are normalized to measurements performed on untreated nanowires. The actual measured values appear above each bar.

In order to examine how the acid treatment reduces dislocation, we must examine how the dislocations form in the first place. There are many mechanisms by which

dislocations may form, but here we will only address two of which that are most relevant to the current discussion: surface imperfections and impurities, such as those from the amorphous layer on SiC nanowires. Firstly, surface stresses concentrate on imperfections, which exist in all crystals. Consider the case of a one atom step on the surface of a cubic crystal. If the stress is great enough a dislocation may form at this site, and be forced into the bulk crystal as depicted in Figure 7.9. Secondly, I propose that the amorphous layer may extend into the SiC matrix creating interstitial oxygen, carbon, and silicon atoms, see Figure 7.10. These point defects force the SiC matrix to expand, thus producing tensile stresses. This combined with stress already present from surface steps leads to a large number of dislocations that would not have formed in the absence of the amorphous layer. The acid treatment removes the amorphous layer, thus reducing stress at the surface. Also, the bonding of the amorphous surface to the SiC crystal can have a similar effect to that of the step shown in Figure 7.9. Dislocations due to small surface steps will spring back to their original form once the compression from amorphous layer is removed, eliminating areas that do not scatter x-rays coherently.

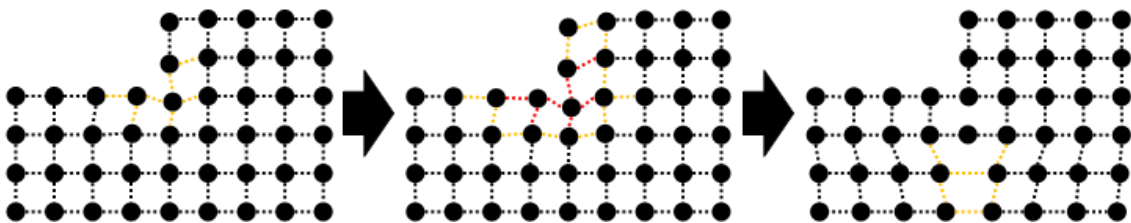


Figure 7.9 The formation of a dislocation from stresses induced by a surface defect.

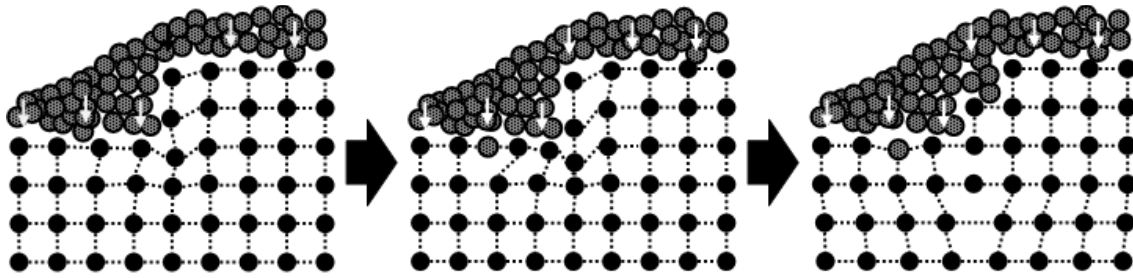


Figure 7.10 The formation of a dislocation from stresses induced by a surface defect and by a surface layer of a different composition.

CHAPTER 8: CONCLUSION

Described in this paper is a highly reproducible method of producing SiC nanowires on a large scale. Distribution of diameters was narrow and the average size of SiC nanowires was 30 nm. XRD revealed that the molar yield increased linearly with time. TEM showed a distribution of nanowire sizes that shifted towards larger diameters as sintering time increased. Also, nanowire sizes depended heavily upon the sizes of the precursors.

The mechanism of the reaction leading to SiC nanowire formation remains controversial. It is known that the VLS reactions involving Si-O ions and C-O molecules play a role, and that the metal catalyst originates in the MWCNT synthesis. We have also focused on a less frequently used vapor to solid model of the reaction involving Stone-Wales defects in carbon nanotubes. Although we have no definite proof that this mechanism is actually responsible for SiC nanowires synthesis, we believe that it provides an alternative route worthy of further exploration.

The pressure-dependent properties of SiC nanowires were investigated and compared to those of SiC grains on the nanometer scale. Synchrotron XRD data were collected from the following SiC samples under pressure applied via a DAC: 20 nm grains, 50 nm grains, 130 nm grains, and nanowires with a 30 nm average diameter. In all samples, the lattice parameter was reduced with pressure; however, the lattice parameter of the nanowires decreased at slower rate than that of 50 nm and 130 nm grains. Moreover, the lattice parameter of 20 nm grains decreased at a rate even slower than that of nanowires. This indicates a size effect in the 30 nm wires and the 20 nm crystals. The same trend was observed when the bulk moduli were extracted from

experimental data. The larger grains generated bulk moduli consistent with that of bulk material. The bulk modulus corresponding to nanowires was 8% larger, while that of 20 nm grains was 30% larger than that of bulk material. In other words, the size effect increases the resistance to compression in silicon carbide.

The increased bulk modulus of 20 nm grains is explained by the core-shell model. The individual SiC grain contains two distinct atomic arrangements: the core and the shell. In bulk material, the majority of the silicon and carbon atoms are arranged in a manner consistent with the core of nanosized grains. Therefore the core atoms exhibit all the properties associated with the bulk material, such as bulk modulus and lattice parameter. The shell atoms, on the other hand, possess unique qualities, because their interatomic distances may differ compared to bulk/core atoms. With nano-sized materials, a much larger percentage of the constituent atoms belong to the shell, and this leads to unique properties.

Previous studies show that SiC particles 20 nm or smaller have shell structures with decreased interatomic distances.^[120] In other words, the shell atoms are already compressed in relation to the core atoms. The effects of this phenomenon are seen in this paper, as the 20 nm grains and 30 nm wires exhibited a much higher bulk modulus. It is logical that these particles better resist compression, because the shell atoms are pre-compressed. Likewise, studies show that the shell atoms belonging to particles of around 80 nm in size have similar interatomic distances to the core atoms. It was seen in this study that 50 nm and 130 nm particles have bulk moduli very similar to that of bulk SiC, indicating that they are too large for the surface atoms to play a dominant role.

It is also possible that defects play a role in altering the elastic properties of SiC nanoparticles, especially in the heavily faulted nanowires. TEM imaging provides qualitative information as to the type and quantity of defects. Planar defects appear in TEM images as rings of darker contrast, and electron diffraction may be utilized to distinguish between stacking faults and twins. From analysis of SiC nanowires, planar faults were abundant, with twins being the most dominant. This is explained by the lower energy of formation for a twin defect than a stacking fault. The number of defects was dependent upon the nanowire diameter, with fewer defects seen in smaller wires. Numerous wires were also seen to have sections that were defect free.

Analysis of TEM images enables discernment between stacking faults and twins, but this is not a simple, routine task and thus not very often used. TEM images are excellent tools when only qualitative analysis is required, but when quantitative analysis is needed, a different experimental technique should be used. In this paper we demonstrated that simultaneous analysis of multiple x-ray diffraction peaks represents such alternative methodology. This analysis showed that the average crystallite size was 31 nm, nearly the same distance as the average diameter of the nanowires, meaning that defects probably serve as grain boundaries that shorten the coherence length observed by x-ray diffraction. This analysis also allowed us to conclude that twins are the most frequently occurring defect with a 2.20% probability of formation, which corresponds to a defect spacing of 38 nm.

SiC nanowires are formed with an amorphous outer layer a few nanometers deep. EDS confirmed that this structure was rich in oxygen, and FTIR confirmed the presence of Si-O bands which increased in population with thermal treatment. Quantitative

analysis of the infrared spectra revealed that the amorphous layer could not consist completely of glass-like compounds, and we concluded that the layer consisted mainly of amorphous SiC.

The surface of SiC nanowires was modified by etching in HF and HNO₃ acids. Silica bands were reduced in both cases, while a CH₂ band at 1460 cm⁻¹ increased dramatically with HNO₃ treatment. This, combined with an increased population of other CH₂ and CH₃ bands seen with both acid treatments, shows that acid etching promotes the formation of functional groups on the surface of SiC nanowires. When x-ray diffraction was applied, it was found that grain size increased by 186% and dislocations decreased by 91% with treatment by nitric acid. Hydrofluoric acid produced a similar result, though to a lesser extent. It is proposed that modification of the surface layer changes the stresses applied to the crystalline core. A reduction of these stresses leads to a reduction of dislocations within the core.

REFERENCES

- [1] P.M. Ajayan, L.S. Schadler, P.V. Braun, *Nanocomposite Science and Technology* (Wiley-VCH, New York, 2003).
- [2] W.H Qi, M.P. Wang, "Size effects on the cohesive energy of nanoparticles." *J. Mat. Sci. Lett.* **21**, 1743-1745 (2002).
- [3] Y. Gogotsi, *Nanomaterials Handbook* (CRC Press, Boca Raton, 2006).
- [4] Y. Shao, Ph.D. dissertation, Texas Christian University, 1996.
- [5] M.S. Dresselhaus, Y.L. Lin, O. Rabin, M.R. Black, J. Kong, G. Dresselhaus, in *Springer Handbook of Nanotechnology*, edited by B. Bhushan (Springer, New York, 2007), pp. 13-14.
- [6] B. Bhushan, in *Springer Handbook of Nanotechnology*, edited by B. Bhushan (Springer, New York, 2007), p. 1593.
- [7] C.H Wu, S. Stefanescu, H.I. Kuo, C.A. Zorman, M. Mehregany, in *Technical Digest – 11th Int. Conf. Solid State Sensors and Actuators – Eurosensors.* **15**, 514-517 (2001).
- [8] A.A. Yasseen, C.H. Wu, C.A. Zorman, M. Mehregany, "Fabrication and Testing of Surface Micro-machined Polycrystalline SiC Micromotors," *IEEE Electron. Dev. Lett.* **21**, 164-166 (2000).
- [9] E.O. Johnson, "Physical Limitations on Frequency and Power Parameters of Transistors," *RCA Rev* **26** 163-177 (1963).
- [10] R.F. Davis, J.W. Palmour, J.A. Edmond. "A review of the status of diamond and silicon carbide devices for high-power, -temperature, and -frequency applications." *International Electron Devices Meeting*, pp.785-788 (1990).
- [11] R.W. Keyes, "Figure of Merit for Semiconductors for High-Speed Switches," *Proc. IEEE* **60** 225-232 (1972)
- [12] B.D. Cullity, *Elements of X-Ray Diffraction* (Oxford University Press, New York, 2001).
- [13] H.P. Myers, *Introductory Solid State Physics* (Taylor and Francis Inc., Bristol, 1997).
- [14] C. Kittel, *Introduction to Solid State Physics* (Wiley, New York, 1995).
- [15] J.D. Jackson, *Classical Electrodynamics* (John Wiley and Sons, Inc., Hoboken, 1999).
- [16] G. Burns, *Solid State Physics* (Academic Press, Inc, Orlando, 1985).
- [17] B.E. Warren, *X-Ray Diffraction* (Dover, New York, 1990).
- [18] W.D. Callister, Jr. *Materials Science and Engineering An Introduction.* (John Wiley and Sons, New York, 2000).

- [19] G.K. Williamson, W.H. Hall, *Acta Metall.* **1** 22-31 (1953).
- [20] T. Ungar, G. Tichy, *Phys. Stat. Sol. A.* **171** 425-434 (1999).
- [21] G. Ribarik, J. Gubicza, T. Ungar, *Mat. Sci. Eng. A* **343** 387-389 (2004).
- [22] L. Balogh, G. Ribarik, T. Ungar *J. Appl. Phys.* **100** 1-10 (2006).
- [23] A. Guiner, *X-Ray Diffraction*, (Freeman, San Fransisco, 1963), pp 1-378.
- [24] E.F. Bertaut, *Acta Cryst.* **3** 9-14 (1950).
- [25] R. Rich, M. Wieligor, T.W. Zerda, "Microstructure of Silicon Carbide Nanowires," in *Silicon Carbide: New Materials, Production Methods, and Applications*, edited by S.H. Vanger (Nova Science Publishers, Hauppauge, 2011).
- [26] T. Ungar, J. Gubicza, G. Ribarik, C. Pantea, T.W. Zerda, *Carbon* **40** 929-937 (2002).
- [27] B.E. Warren, B.L. Averbach, *J. Appl. Phys.* **21** 595-610 (1950).
- [28] M.A. Krivoglaz, *Theory of X-ray and Thermal Neutron Scattering by Real Crystals*, (Plenum, New York, 1969), pp 95-122.
- [29] M. Wilkens, in *Fundamental Aspects of Dislocation Theory*, edited by J.A. Simmons, R. de Wit, and R. Bullough, (NBS Spec. Publ., Washington, DC, 1970) Vol. 2, p. 317.
- [30] L. Balogh, G. Ribarik, T. Ungar, *J. Appl. Phys.* **100** 023512 (2006).
- [31] M.M.J. Treacy, J.M. Newsam, M.W. Deem, *Proc. Roy. Soc. Lond. A.* **433** 499-520 (1991).
- [32] L. Balogh, S. Nauyoks, T.W. Zerda, C. Pantea, S. Stelmakh, B. Palosz, T. Ungar, *Mater. Sci. Eng. A.* **487** 180-188 (2008).
- [33] R. Miletich, D.R. Allan, W. F. Kuhs. "High-Pressure Single-Crystal Techniques." in *Reviews in Mineralogy & Geochemistry*, edited by R.M. Hazen and R.T. Downs. (Mineralogical Society of America, Washington, D.C., 2000), pp. 445-519.
- [34] P.F. McMillan, "Pressing on: The Legacy of Percy W. Bridgman," *Nature Materials* **4** 716-718 (2005).
- [35] H.E. Lorenzana, M. Bennahmias, H. Radousky, M. B. Kruger. "Producing diamond anvil cell gaskets for ultrahigh-pressure applications using an inexpensive electric discharge machine," *Rev. Sci. Instrum* **65** (11) 3540-3543 (1994).
- [36] G.J. Piermarini, S. Block, J.D. Barnett, R.A. Forman, "Calibration of the pressure dependence of the R1 ruby fluorescence line to 195 kbar," *Journal of Applied Physics* **46** (6) 2774-2780 (1975)

- [37] J.C. Jamieson, J.N. Fritz, M.H. Manghnani, in *High-Pressure Research in Geophysics Pressure*, edited by S. Akimoto and M. H. Manghnani (Center for Academic Publications, Tokyo, 1982), pp. 27–48.
- [38] O.L. Anderson, D.G. Isaak, and S. Yamamoto, “Anharmonicity and the Equation State for Gold,” *J. Appl. Phys.* **65** (4) 1534 (1989).
- [39] W.B. Holzapfel, in *High Pressure Techniques in Chemistry and Physics*, edited by W. B. Holzapfel and N. S. Isaacs Oxford University Press. Section 2.2. Oxford, 1997. Pp51-52.
- [40] W.B. Holzapfel, in *Units and fundamental constants in physics and chemistry*, edited by J. Bortfeldt and B. Kramer (Springer Verlag, Berlin, 1991), pp. 2.177-2.184.
- [41] W.B. Holzapfel, *High Press. Res.* 1991, pp. 2.177-2.184.
- [42] W.B. Holzapfel, *J. Phys. Chem. Solids* **55** 711-719 (1994).
- [43] G.J. Piermarini, S. Block, J.D. Barnett, “Hydrostatic limits in liquids and solids to 100 kbar,” *J. Appl. Phys.* **44** (12) 5377-5382 (1973).
- [44] A.P. Jephcoat, H.K. Mao, P.M. Bell. “Static compression of iron to 78 GPa with rare gas solids as pressure-transmitting media,” *J. Geophys. Res.* **91** 4677-4684 (1986).
- [45] I. Fujishiro, G.J. Piermarini, S. Block, R.G. Munro, “Viscosities and glass transition pressures in the methanol-ethanol-water system,” in *High Pressure in Research and Industry, Proc 8th AIRAPT Conf, Uppsala*, edited by C.M. Blackman, T. Johannison, and L. Tegner (1981) pp. 608-611.
- [46] J.M. Besson in *High-Pressure Techniques in Chemistry and Physics*, edited by W. B. Holzapfel and N. S. Isaacs (Oxford University Press, Oxford, 1997).
- [47] A. Jayaraman, "Diamond anvil cell and high-pressure physical investigations," *Rev. Mod. Phys.* **55** 65-108 (1983).
- [48] R.A. Foreman, G. J. Piermarini, S. Block, *Science* **176** 284-285 (1972).
- [49] J.D. Barnett, S. Block, G. J. Piermarini, *Rev. Sci. Instrum.* **44** 1 (1973).
- [50] G.J. Piermarini, and S. Block, *Rev. Sci. Instrum.* **46**, 973 (1975).
- [51] H.K. Mao, P. M. Bell, J. W. Shaner, D. J. Steinberg, *J. Appl. Phys.* **52** 4572 (1978).
- [52] V.I. Goriletsky, A.I. Mitichkin, L.E. Belenko, T.P. Rebrova, *Semiconductor Physics, Quantum Electronics, and Optoelectronics*, **4** (2) 139-141 (2001).
- [53] *X-rays, the first hundred years*, edited by A.G. Michette and S. Pfauntsch (John Wiley & Sons, New York, 1996).

- [54] D. M. Mills “Synchrotron Radiation Properties and Production” presentation at the National School on Neutron and X-ray scattering. August 12-25, 2007. Argonne National Laboratory.
- [55] Rev. Sci. Instrum. 73, 1615 (2002); doi:10.1063/1.1448127 (1 page)
- [56] S. Matsuyama, H. Mimura, H. Yumoto, K. Yamamura, Y. Sano, K. Endo, Y. Mori, M. Yabashi, K. Tamasaku, Y. Nishino, T. Ishikawa, K. Yamauchi, "Diffraction-limited two-dimensional hard-X-rays focusing in 100nm level using K-B mirror arrangement," *Review of Scientific Instrument.* **76**, 083114 (2005).
- [57] A. Hammersley, computer code Fit2D (ESRF, Grenoble, 1998).
- [58] M. Wojdyr, computer code Fityk (Unipress, Warsaw, 2004).
- [59] S. Wisnitzer, *Introduction to Electron Microscopy* (Pergamon Press, Elmsford 1970).
- [60] I.M. Watt, *The Principles and Practice of Electron Microscopy*. (Cambridge University Press, Cambridge, 1985), pp. 1-19.
- [61] J. I. Goldstein, D. E. Newbury, P. Echlin, D. C. Joy, C. Fiori, E. Lifshin, *Scanning Electron Microscopy and X-Ray Microanalysis*, (Plenum Press, New York, 1981), pp. 222-230.
- [62] B. Bhushan, “Nanotribology and Materials Characterization of MEMS/NEMS and Bio MEMS/BioNEMS Materials and Devices” in *Springer Handbook of Nanotechnology*, edited by B. Bhushan, (Springer, New York, 2007), pp. 1593.
- [63] Z. Zhang, J.Y. Ying, M.S. Dresselhaus, "Bismuth quantum-wire arrays fabricated by a vacuum melting and pressure injection process," *J. Mater. Res.* **13** 1745-1748 (1998).
- [64] C.A. Huber, T.E. Huber, M. Sadoqi, I.A. Lubin, S. Manalis, C.B. Prater, "Nanowire array composites," *Science* **263** 800-802 (1994).
- [65] Y.M. Lin, S.B. Cronin, J.Y. Ying, M.S. Dresselhaus, J.P. Heremans, "Transport properties of Bi nanowire arrays," *Appl. Phys. Lett.* **76** 3944-3946 (2000).
- [66] G. L. Hornyak, C.i. Patrissi, C. M. Martin: Fabrication, characterization and optical properties of gold nanoparticle/porous alumina composites: the non-scattering Maxwell-Garnett limit, *J. Phys. them. B* 101, 1548—1555 (1997)
- [67] L. Piraux, S. Dubois, J.L. Duvail, A. Radulescu, S. Demoustier-Champagne, E. Ferain, R. Legras, "Fabrication and properties of organic, metal nanocylinders in nanoporous membranes," *J. Mater. Res.* **14** 3042-3050 (1999).
- [68] D. Routkevitch, T. Bigioni, M. Moskovits, I.M. Xu, "Electrochemical fabrication of tdS nanowire arrays in porous anodic aluminum oxide templates," *J. Phys. Chem.* **100** 14037-14047 (1996).
- [69] D. Al-Mawlawi, N. Coombs, M. Moskovits, "Magnetic properties of Fe deposited into anodic aluminum oxide pores as a function of particle size," *J. App. Phys.* **70** 4421-4425 (1991).

- [70] L. Sun, P.C. Searson, L. Chien, "Electrochemical deposition of nickel nanowire arrays in single-crystal mica films," *Appl. Phys. Lett.* **74** 2803-2805 (1999).
- [71] C. R. Martin: Nanomaterials: A membrane-based synthetic approach, *Science* 266, 1961-1966 (1994)
- [72] K. Liu, C. L. Chien, P.C. Searson, Y.Z. Kui, "Structural and magneto-transport properties of electrode-positied bismuth nanowires," *Appl. Phys. Lett.* **73** 1436-1438 (1988).
- [73] R. Ferre, K. Ounadjela, J.M. George, L. Piraux, S. Dubbois, "Magnetization processes in nickel and cobalt electrodeposited nanowires", *Phys. Rev. B* **56** 14066-14075 (1977).
- [74] H. Zeng, M. Zheng, R. Skomski, D. J. Sellmyer, Y. Liu, L. Menon, S. Bandyopadhyay, "Magnetic properties of self-assembled Co nanowires of varying length and diameter" *J. Appl. Phys.* **87** 4718-1720 (2000).
- [75] Y. Peng, H.L. Zhang, S.L. Pan, H.L. Li, "Magnetic properties and magnetization reversal of alpha-Fe nanowires deposited in alumina film," *J. Appl. Phys.* **87** 7405-7408 (2000).
- [76] L. Pirauz, J. M. George, J. F. Despres, C. Leroy, E. Ferain, R. Legras, K. Ounadjela, A. Fert, "Giant magnetoresistance in magnetic multilayered nanowires," *Appl. Phys. Lett.* **65** 2484-2486 (1994).
- [77] S. Bhattacharrya, S.K. Saha, D. Chakravorty, "Nanowire formation in a polymeric film," *Appl. Phys. Lett.* **76** 3896-3898 (2000).
- [78] G. Yi, W. Schwarzacher, "Single crystal superconductor nanowires by electrodeposition," *Appl. Phys. Lett.* **74** 1746-1748 (1999).
- [79] J. Heremans, C.M. Thrush, Y.M. Tin, S. Cronin, Z. Zhang, M.S. Dresselhaus, J.F. Mansfield, "Bismuth nanowire arrays: synthesis, galvanomagnetic properties," *Phys. Rev. B* **61** 2921-2930 (2000).
- [80] G.S. Cheng, L.D. Zhang, V. Zhu, G.T. Fei, L. Li, C.M. Mo, V.Q. Mao, "Large-scale synthesis of single crystalline gallium nitride nanowires," *Appl. Phys. Lett.* **75** 2455-2457 (1999).
- [81] G.S. Cheng, L.D. Zhang, S.H. Chen, Y. Li, L. Li, X.G. Zhu, Y. Zhu, G.T. Fei, V.Q. Mao, "Ordered nanostructure of single-crystalline GaN nanowires in a honeycomb structure of anodic alumina," *J. Mater.Res.* **15** 347-350 (2000).
- [82] K. Wallis, "Production and Characterization of Nanostructured Silicon Carbide," Ph.D. dissertation, Texas Christian University, 2008.
- [83] A. N. Nesmeyanov, *Vapour Pressure of the Elements* (Infosearch Ltd., New York, 1963).
- [84] C. Pantea, "Kinetics of Diamond – Silicon Reaction under High Pressure-High Temperature Conditions," Ph.D. dissertation, Texas Christian University, 2004.

- [85] V. Cimalla, C. Foerster, D. Cengher, K. Tonisch, O. Ambacher, *Phys. Stat. Sol.* **243** (7) 1476-1480 (2006).
- [86] R.S. Wagner, W.C. Ellis, "Vapor-liquid-solid mechanism of single crystal growth," *Appl. Phys. Lett.* **4** 89-90 (1964).
- [87] Y. Wu, R. Fan, P. Yang, "Direct observation of vapor-liquid-solid nanowire growth," *J. Am. Chem. Soc.* **123** 3165-3166 (2001).
- [88] P. Madras, E. Dailey, J. Drucker, "Kinetically Induced Kinking of Vapor-Liquid-Solid Grown Epitaxial Si Nanowires," *Nano Lett.* **9** (11) 3826-3830 (2009).
- [89] NanoAmor certificate of analysis
http://www.nanoamor.com/coa/coa_MWNT_1234NMG.pdf
- [90] M. Wieligor, R. Rich, T.W. Zerda, *J. Mater. Sci.* **45** (7) 1725-1733 (2010).
- [91] W. Han, P. Redlich, F. Ernst, M. Rühle, Synthesizing boron nitride nanotubes filled with SiC nanowires by using carbon nanotubes as templates," *Appl. Phys. Lett.* **75** (13) 1875-1877 (1999).
- [92] G. Shen, Y. Bando, C. Ye, B. Liu, D. Golberg. "Synthesis, characterization and field-emission properties of bamboo-like β -SiC nanowires," *Nanotechnology* **17** 3468-3472 (2006).
- [93] X. Sun, C. Li, W. Wong, N. Wong, C. Lee, S. Lee, B. Teo, "Formation of Silicon Carbide Nanotubes and Nanowires via Reaction of Silicon (from Disproportionation of Silicon Monoxide) with Carbon Nanotubes," *J. Am. Chem. Soc.* **124** 12264-14471 (2002).
- [94] D. Mawhinney, V. Naumenko, A. Kuznetsova, J.T. Yates, J. Liu, R.E. Smalley, *Chem. Phys. Lett.* **324** 213-216 (2000).
- [95] Y. Wang, T.W. Zerda, *J. Phys. Condens. Mater.* **18** 2995-3003 (2006).
- [96] Y. Miyamoto, A. Rubio, S. Berber, M. Yoon, D. Tomanek, *Phys. Rev. B* **69** 121413-121417 (2004).
- [97] J. Ma, D. Alfe, A. Michaelides, E. Wang, *Phys. Rev. B* **80** 033407-033411 (2009).
- [98] N. Chakrapani, Y.M. Zhang, S.K. Nayak, J.A. Moore, D.L. Carroll, Y.Y. Choi, P.M. Ajayan, *J. Phys. Chem. B* **107** 659308 (2003).
- [99] S. Picozzi, S. Santucci, L. Lozzi, L. Valentini, B. Delley, *J. Chem. Phys.* **120** 7147 (2004).
- [100] V. Cimalla, T. Wohner, J. Pezoldt, *Mater. Sci. Forum.* **321** 338-342 (2000).
- [101] R.N. Ghoshtagore, R.L. Coble, *Phys. Rev.* **143** 623-626 (1966).
- [102] M.N. Hon, R.F. Davis, *J. Mater. Sci.* **14** 2411-2421 (1979).
- [103] M.N. Hon, R.F. Davis, *J. Mater. Sci.* **15** 2073-2080 (1980).

- [104] D.P Birnie, *J. Am. Ceram. Soc.* **69** C33-C35 (1986).
- [105] C. Pantea, G.A. Voronin, T.W. Zerda, J. Zhang, L. Wang, Y. Wang, T. Uchida, Y. Zhao, *Diamond Relat. Mater.* **14** 1611-1615 (2005) .
- [106] “NIST Property Data Summaries for Sintered Silicon Carbide (SiC).” NIST Structural Ceramics Database, SRD Database Number 30. National Institute of Standards and Technology.
<<http://www.ceramics.nist.gov/srd/summary/scdscs.htm>>
- [107] Z. J. Lin, L. Wang, J. Zhang, X. Guo, W. Yang, H. Mao, Y. Zhao, *Scripta Materiala* **63** 981-984 (2010).
- [108] H.Y. Zhu, Y.Z. Ma, H.B. Yang, E. Selvi, D.B. Hou, C. Ji, *J. Appl. Phys.* **104** 123516 (2008).
- [109] H.Z. Liu, J.Z. Hu, J.F. Shu, D. Hausermann, H.K. Mao, *Appl. Phys. Lett.* **85** 1973 (2004).
- [110] K.J. Chang, M.L. Cohen, "Ab initio pseudopotential study of structural and high-pressure properties of SiC," *Phys. Rev. B* **35** (15) 8196-8201.
- [111] F. Shimojo, I. Ebbsjö, R.K. Kalia, A. Nakano, J.P. Rino, P. Vashishta, "Molecular Dynamics Simulation of Structural Transformation in Silicon Carbide under Pressure," *Phys. Rev. Lett.* **84** (15) 3338-3341 (2000).
- [112] M. Duranduru, "Pressure-induced phase transition of SiC," *J. Phys.: Condens. Matter* **16** 4411-4417 (2004).
- [113] M. Yoshida, A. Onodera, M. Ueno, K. Takemura, and O. Shimomura, "Pressure-induced phase transition in SiC," *Physical Review B.* **48** (14) 587-589 (1993).
- [114] X. Wu, Z. Wu, L. Guo, C. Liu, J. Liu, X. Li, H. Xu. *Solid State Comm.* **135** 780-784 (2005).
- [115] Y. Wang, J. Zhang, J. Wu, J. Coffer, Z. Lin, V. Sinogeikin, W. Yang, Y. Zhao, *Nano Lett.* **8** (9) 28911-2895 (2008).
- [116] F. Birch, "Finite Elastic Strain of Cubic Crystals," *Phys.Rev.* **71** (11) 809-824 (1947).
- [117] M. Podesta, *Understanding the Properties of Matter* (Taylor and Francis, New York, 2002).
- [118] B. Palosz, S. Stelmakh, E. Grzanka, S. Gierlotka, W. Palosz, Z. *Kristallographie***222** 580-594 (2007).
- [119] S. Stelmakh, E. Grzanka, M. Wojdyr, T. Proffen, S.C. Vogel, T.W. Zerda, W. Palosz, B.Z. Palosz, *Kristallographie* **222** 174-187 (2007).
- [120] B. Palosz, S. Stelmakh, E. Grzanka, S. Gierlotka, S. Nauyoks, T.W. Zerda, W.J. Palosz, *Appl. Phys.* **102** 074303 (2007).

- [121] S. Stelmakh, E. Grzanka, Y. Zhao, W. Palosz, B.Z. Palosz, *Kristallographie (Supplement)* **23** 331-336 (2006) .
- [122] B. Palosz, E. Grzanka, S. Gierlotka, S. Stel'makh, R. Pielaszek, W. Lojkowski, U. Bismayer, J. Neuefeind, H.P. Weber, W. Palosz, *Phase Transitions* **76** 171-185 (2003).
- [124] B. Palosz, E. Grzanka, S. Gierlotka, M. Wojdar, W. Palosz, T. Proffen, S. Stel'makh, in *Proceedings IUTAM Symposium on Modeling Nanomaterials and Nanosystems*, edited by R. Pyrz and J.C. Rauche (Springer, Aalborg, 2009), pp. 75-88.
- [125] Y. Zhang, X. Han, K. Zheng, Z. Zhang, J. Fu, Y. Ji, Y. Hao, X. Guo, Z. Wang, *Adv. Funct. Mater* **17** 3435-3440 (2007).
- [126] Y. Wang, T.W. Zerda, *J. Phys. Condens. Mater.* **18** 2995 (2006).
- [127] T. Seeger, P.K. Redlich, M. Ruhle, *Adv. Mater.* **12** 279-282 (2000).
- [128] S. Veprék, in *Handbook of Ceramic Hard Materials* edited by R. Riedel (Wiley-VCH, Weinheim, 2000), pp. 104-139.
- [129] J. Liu, Z. Liu, P. Ren, P. Xu, X. Chen, X. Xu, *Acta Phys. Chim. Sinica* **24** 571-575 (2008).
- [130] A. Fissel, B. Schroter, U. Kaiser, W. Richter, *Appl. Phys. Lett.* **77** 2418-2420 (2000).
- [131] A. Fissel, U. Kaiser, B. Schroter, W. Richter, F. Bechstedt, *Appl. Surf. Sci.* **184** 37-42 (2001).
- [132] F. Bechstedt, A. Fissel, J. Furthmüller, U. Kaiser, H. Weissker, W. Wesc, *Appl. Surf. Sci.* **212** 820-825 (2003).
- [133] D. H. Wang, D. Xu, Q. Wang, Y.J. Hao, G. Q. Jin, X. Guo, K. N. Tu, *Nanotechnology* **19** 215602 (2008).
- [134] A. Fissel, U. Kaiser, B. Schroter, W. Richter, F. Bechstedt, *Appl. Surf. Sci.* **184** 37-42 (2001).
- [135] A.J. Cao, Y.G. Wei, S.X. Mao, *JOM* **60** 85 (2008).
- [136] Z.G. Wang, D. Xu, Q. Wang, Y.J. Hao, G.Q. Jin, X.Y. Guo, K.N. Tu, *Nanotechnology* **19** 215602 (2008).
- [137] M. Wieligor, Y. Wang, T.W. Zerda, *J. Phys. Condens. Matter.* **17** 2387-2395 (2005).
- [138] K.L. Wallis, "Production and Characterization of Nanostructured Silicon Carbide." Ph.D. dissertation, Texas Christian University, 2008.
- [139] *Handbook of Nanophase and Nanostructured Materials* edited by Z.L. Wang, Y. Liu, and Z. Zhang (Kluwer Academic/Plenum Publishers, New York, 2003) Vol. 2. pp 37-41.

- [140] F.M. Davidson, D.C. Lee, D.D. Fanfair, B.A. Korgel, *J. Phys. Chem. C* **111** 2929-2935 (2007).
- [141] F.M. Davidson, A.D. Schricker, R. Wiacek, B. A. Korgel, *Adv. Mater* **16** 646-649 (2004).
- [142] F.M. Davidson, R. Wiacek, B.A. Korgel, *Chem. Mater* **17** 230-233 (2005).
- [143] J. Johansson, L.S. Karlsson, C.P.T. Svensson, T. Martensson, B.A. Wacaser, K. Deppert, L Samuelson, W. Seifert, *Nat. Mater* **5** 574-580 (2006).
- [144] Q. Li, X.G. Gong, C.R. Wang, J. Wang, K. Ip, S. Hark, *Adv. Mater* **16** 1436-1440 (2004).
- [145] Y. Hao, G. Meng, Z.L. Wang, C. Ye, L. Zhang, *Nano lett.* **6** 1650-1655 (2006).
- [146] D. Shechtman, A. Feldman, M.D. Vaudin, J.L. Hutchison, *Appl. Phys. Lett.* **62** 487-489 (1993).
- [147] T.L. Daulton, T.J. Bernatowicz, R.S. Lewis, S. Messenger, F.J. Stadermann, S. Amari, *Geochimica et Cosmochimica Acta* **67** 4743-4767 (2003).
- [148] D.H. Wang, D. Xu, Q. Wang, Y. J. Hao, G.Q. Jin, X.Y. Guo, K.N. Tu, *Nanotechnology* **19** 215602 (2008).
- [149] B. Hyde, H.D. Espinosa, D. Farkas, *JOM* **57** 62-66 (2005).
- [150] L. Wang, H. Wada, L.F. Allard, *J. Mater. Res.* **7** 148-163 (1992).
- [151] Y. Zhang, H.W. Shim, H. Huang, *Appl. Phys. Lett.* **92** 261908 (2008).
- [152] D.-H. Wang, *Nanotechnology* **19** 215602-215609 (2008).
- [153] Y. Zhang, N. Wang, S. Gao, R. He, S. Miao, J. Liu, J. Zhu, X. Zhang, *Chem. Mater.* **14** 3564-3568 (2002).
- [154] J.J. Niu, J.N. Wang, *J. Phys. Chem. B* **111** 4368-4373 (2007).
- [155] S. Roy, M. Portail, T. Chassagne, J. M. Chauveau, P. Vennegues, M. Zielinski, *Appl. Phys. Lett.* **95** 081903 (2009).
- [156] Q. Yu, Z.W. Shan, J. Li, H. Huang, L. Xiao, J. Sun, E. Ma, *Nature* **463** 335-338 (2010).
- [157] O. Kraft, *Nat. Mater.* **9** 295-296 (2010).
- [158] S. E. Nauyoks, "Microstructure of Nano and Micron Size Diamond-SiC Composites Sintered Under High Pressure High Temperature Conditions," Ph.D. dissertation, Texas Christian University, 2009.
- [159] S.E. Nauyoks, M. Wieligor, T. W. Zerda, L. Balogh, T. Ungar, P. Stephens, *Compos. Part A.-Appl. S.* **40** 566-572 (2009).
- [160] J. I. Langford, D. Louer, *Rep. Prog. Phys.* **59** 131-234 (1996).
- [161] G.A. Voronin, T.W. Zerda, J. Qian, Y. Zhao, D. He, S. N. Dub, *Diamond Relat. Mater.* **12** 1477-1481 (2003).

- [162] J. Gubicza, T. Ungar, Y. Wang, G.A. Voronin, C. Pantea, T.W. Zerda, *Diamond Relat. Mater.* **15** 1452-1456 (2006).
- [163] C. Pantea, J. Gubicza, T. Ungar, G.A. Voronin, T.W. Zerda, *Phys. Rev. B* **66** 094106 (2002).
- [164] J. Gubicza, S.E. Nauyoks, L. Balogh, J. Labar, T.W. Zerda, T. Ungar, *J. Mater. Res.* **22** 1314-1321 (2007).
- [165] E.O. Johnson, "Physical Limitations on Frequency and Power Parameters of Transistors," *RCA Rev.* **26** 163-177 (1963).
- [166] R.F. Davis, J.W. Palmour, J.A. Edmond. "A review of the status of diamond and silicon carbide devices for high-power, -temperature, and -frequency applications." *Electron Devices Meeting, 1990. Technical Digest., International*, (1990) pp. 785-788.
- [167] Choyke, W. J.; Matsunami, H.; Pensl, G. *Silicon Carbide: Recent Major Advances; Advanced Texts in Physics; Springer-Verlag: Berlin Heidelberg, 2004; Vol. 79, pp 1-4.*
- [168] Harris, G. L. in *Properties of Silicon Carbide; Harris, G. L. Ed.; Datareviews Series; The Institution of Electrical Engineers: London, UK, 1995; Vol. 13, pp.12-133.*
- [169] Y. Cui, C.M. Lieber, *Science* **291** 851-853 (2001).
- [170] R. Rurali, *Phys. Rev. B* **71** 205405 (2005).
- [171] C. M. Lieber, *Nano Lett.* **2** 81-82 (2002).
- [172] H. Dai, E.W. Wong, Y.Z. Lu, S. Fan, C.M. Lieber, *Nature* **375** 769-772 (1995).
- [173] H.K. Seong, H.J. Choi, S.K. Lee, J.I. Lee, D.J. Choi, *Appl. Phys. Lett.* **85** 1256-1259 (2004).
- [174] B. Yan, G. Zhou, W. Duan, J. Wu, B. Gu, *Appl. Phys. Lett.* **89** 023104 (2006).
- [175] E.W. Wong, P.E. Sheehan, C.M. Lieber, *Science* **277** 1971-1975 (1997).
- [176] C.F. Bohren, D.R. Huffman, *Absorption and scattering of light by small particles* (Wiley, New York, 1983).
- [177] G. Socrates, *Infrared and Raman Characteristic Group Frequencies: Tables and Charts, 3rd Edition* (John Wiley & Sons, West Sussex, 2001).
- [178] B.C. Smith, *Infrared Spectral Interpretation: A Systematic Approach* (CRC Press, Boca Raton, 1996).
- [179] T.M. Mejean, E. Abdelmounim, P.S. Quintard, *J. Mol. Struct.* **349** 105 (1995).
- [180] G. Jin, P. Liang, X. Guo, *J. Mater. Sci. Lett.* **22** (10) 767-770 (2006).
- [181] Y.G. Gogotsi, K.G. Nickel, D. Bahloul-Hourlier, T. Merle-Mejean, G.E. Khomenko, K.P. Skjerlie. *J. Mater. Chem.* **6** 595-604 (1996)

ABSTRACT

SILICON CARBIDE NANOWIRES: ELASTIC PROPERTIES AND THE INFLUENCE FROM DEFECTS AND SURFACE FORMATIONS

by Ryan Michael Rich, Ph.D., 2011
Department of Physics
Texas Christian University

Dissertation Advisor:
T.W. Zerda, Professor of Physics, Chair of the Department

A highly reproducible method of producing SiC nanowires on a large scale is presented, and the average size of SiC nanowires was 30 nm. XRD revealed that the molar yield increased linearly with time. TEM showed a distribution of nanowire sizes that shifted towards larger diameters as sintering time increased. It is known that vapor-liquid-solid reactions involving a metal catalyst play a role in their formation, and there is further evidence that a vapor-solid mechanism contributes as well.

The elastic properties of the following SiC morphologies were explored with pressure applied via a diamond anvil cell: 20 nm grains, 50 nm grains, 130 nm grains, and 30 nm nanowires. The bulk modulus of nanowires increased by 8%, while that of 20 nm grains increased 30% in comparison to bulk material. The increased bulk modulus is explained by the core-shell model, where nanoparticles possess one or more distinct regions near the surface with identical crystal symmetry but different interatomic distances.

Defects may also affect the bulk modulus, especially in the heavily faulted nanowires. As seen by TEM, planar faults were abundant, and their quantity decreased with decreasing diameter. The extended Convolutional Multiple Whole Profile (eCMWP) analysis was employed to quantitate the defects by XRD. This analysis concluded that twins are the most frequently occurring planar fault with a 2.20% probability of formation, which corresponds to a defect spacing of 38 nm.

SiC nanowires are formed with an amorphous outer layer a few nanometers deep. It was concluded that the layer consisted mainly of amorphous SiC, but EDS confirmed that this structure was rich in oxygen. FTIR confirmed the presence of Si-O bands which increased in population with thermal treatment. The surface of SiC nanowires was modified by etching in HF and HNO₃ acids. Silica bands were reduced and functional groups appeared after treatment. XRD found that grain size increased by 186% and dislocations decreased by 91% with treatment by nitric acid. It is proposed that modification of the surface leads to a reduction of surface stresses, thereby increasing the apparent grain size and reducing dislocations.

VITA

- Personal** Ryan Michael Rich
Born August 1, 1984 in Danville, Kentucky
Son of Michael Allen and Sharon Elizabeth Rich
To marry Shannon Kay Good, July 9, 2011
- Education** Diploma, Marshall County High School,
Benton, Kentucky, 2002
Bachelor of Science, Physics, Centre College,
Danville, Kentucky, 2006
Doctor of Philosophy, Physics, Texas Christian University
Fort Worth, Texas, 2011
- Working Experience** Research Experience for Undergraduates, Texas Christian
University, Fort Worth, Texas, 2005.
Research/Teaching Assistant, Texas Christian University, Fort
Worth, 2006-2011.
National School on X-ray and Neutron Diffraction, Argonne
National Laboratory, Argonne, IL, 2007.
- Professional Memberships** American Physical Society, Materials Research Society
- Research** Diamond Anvil Cell, Transmission/Scanning Electron Microscopy,
Electron Diffraction, Energy Dispersive Spectroscopy, X-ray
Diffraction, Fourier Transform Infrared Spectroscopy,
Photoluminescence Spectroscopy
- Publications**
- 1) "Microstructure of Silicon Carbide Nanowires" in *Silicon Carbide: New Materials, Production Methods, and Applications*. (Nova Science Publishing, 2011)
 - 2) "Bulk Modulus of Silicon Carbide Nanowires and Nanosize Grains." *Journal of Material Science*. Volume 44, Number 11. Pages 3010-3013. June 2009.
 - 3) "Study on silicon carbide nanowires produced from carbon blacks and structure of carbon blacks." *Journal of Material Science*. Volume 45, Number 7. Pages 1725-1733. April 2010.
 - 4) "Silicon Carbide Nanowires Synthesis and Preliminary Investigations." *Acta Physica Polonica A*. Vol. 118. Pages 480-482. 2010.
 - 5) "Looking Beyond Limitations of Diffraction Methods of Structural Analysis of Nanocrystalline Materials." IUTAM Symposium on Modeling Nanomaterials and Nanosystems. Pages 75-88. 2009.